# Harnessing disorder for photonic device applications

Hui Cao[a] and Yaniv Eliezer

**AFFILIATIONS**

Department of Applied Physics, Yale University, New Haven, Connecticut 06520, USA

[a]Author to whom correspondence should be addressed: hui.cao@yale.edu

**ABSTRACT**

For photonic devices, structural disorder and light scattering have long been considered annoying and detrimental features that were best avoided or minimized. This review shows that disorder and complexity can be harnessed for photonic device applications. Compared to ordered systems, disordered systems provide much more possibilities and diverse optical responses. They have been used to create physical unclonable functions for secret key generation, and more recently for random projection, high-dimensional matrix multiplication, and reservoir computing. Incorporating structural disorder enables novel devices with unique functionalities as well as multi-functionality. A random system can function as an optical lens, a spectrometer, a polarimeter, and a radio frequency receiver. It is also employed for optical pulse measurement and full-field recovery. Multi-functional disordered photonic devices have been developed for hyperspectral imaging, spatial, and spectral polarimetry. In addition to passive devices, structural disorder has been incorporated to active devices. One prominent example is the random laser, which enables speckle-free imaging, super-resolution spectroscopy, broad tunability of high-power fiber laser, and suppression of lasing instabilities. Disordered devices have low fabrication costs, and their combination with advanced computational techniques may lead to a paradigm shift in photonics and optical engineering.

## TABLE OF CONTENTS

**FIG. 1.** Order vs disorder. A periodic array of particles with identical size and shape in (a) has a only a few well-defined spatial frequencies (b). A disordered array of particles with irregular size and shape and varying refraction index in (c) contains many spatial frequencies (d).

## I. INTRODUCTION

While most photonic devices are designed to have regular, ordered structures, disordered structures provide much more possibilities. Compared to a periodic array of particles with identical size and shape [Fig. 1(a)], disorder may be introduced to spatial position, size, and shape of an individual particle [Fig. 1(b)]. An ordered structure has only a few spatial frequencies [Fig. 1(c)], but a disordered structure contains many more spatial frequencies [Fig. 1(d)], providing a huge parameter space for device design. Consequently, an inverse design of photonic devices, namely, optimizing device configurations for desired functionalities, often ends up with "seemingly" disordered structures instead of ordered ones.[1]

Over the years, there have been growing interest and efforts in harnessing disorder for photonic device applications. More and more examples show that incorporating disorder not only improves the performance of existing devices, but also enables novel schemes and additional functionalities. Disordered structures are easy to fabricate and have low costs, while providing diverse responses to external signals. As photonic devices, their functionalities often rely on post-processing of their responses using computational algorithms, including compressive sensing and machine learning. Such algorithms have advanced rapidly in recent years; meanwhile, physical size and cost of processors have fallen sharply. Therefore, the emergence of disordered photonic devices enables a paradigm shift of device design from hardware to software, which will dramatically lower the cost.

### A. Motivation

In this subsection, we will present a few examples to illustrate some of the advantages for incorporating disorder to photonic devices. More details and relevant references can be found in Secs. I A 1–I A 4.
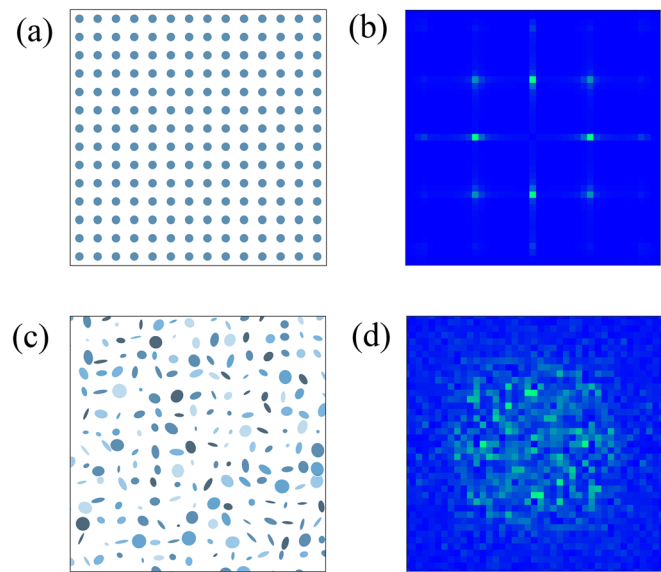
### 1. Optical physical unclonable functions (PUFs) for secret key generation

A disordered system packed with billions of micro- or nanoparticles possesses an enormous amount of entropy, and features diverse optical responses to external interrogations.[2] As illustrated in Fig. 2, directing a laser beam to a bulk random sample will generate a seemingly random grainy pattern (speckle) in transmission or reflection (response), which depends on the illumination condition (challenge). The huge number of challenge–response pairs makes a complete characterization impossible, and machine learning attacks ineffective. Moreover, it is extremely difficult, if not impossible, to clone the random dense packing of numerous particles with irregular size and shape to reproduce the response (speckle pattern). The extraordinary complexity, uniqueness, high sensitivity, and low fabrication costs make the random scattering media an ideal candidate of strong PUFs for authentication and information security.

### 2. Random spectrometers

Most spectrometers use periodic gratings to diffract light of different wavelengths to different directions, so that they are spatially separated and measured by different sensors. Figure 3(a) shows one-to-one spectral-to-spatial mapping; that is, each wavelength is mapped to a single spatial location. If the location falls outside a sensor array, the corresponding wavelength will not be detected at all. To cover different spectral range, the grating must be rotated. Such rotation is extremely challenging, if not impossible, to implement with a monolithic grating in an on-chip spectrometer.

If the periodic grating is replaced by a disordered structure, random diffraction will project a signal to all sensors, regardless of its wavelength. Every wavelength generates a distinct spatial distribution

**FIG. 2.** Physical unclonable function (PUF) for secure key generation. A coherent laser beam impinges on a 3D linear scattering medium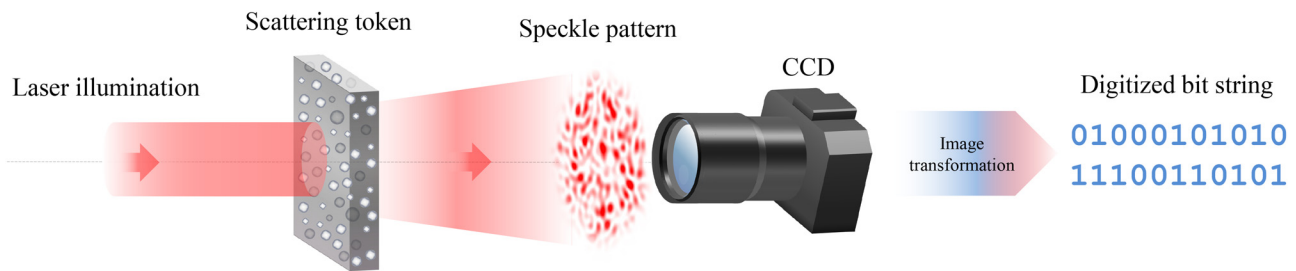 (token) and generates a random speckle pattern as response. The pattern is recorded by a 2D camera and digitally processed to extract a bit string as the key. An enormous number of keys can be generated by varying the spatial position and incident angle of the illumination beam to create different speckle patterns.

of light intensity across the sensor array and can be used as "fingerprint" for spectral reconstruction.[3] As shown in Fig. 3(b), the one-to-many spectral-to-spatial mapping allows a small number of sensors to cover a broad wavelength range, even with a fixed disordered structure. The spectrum cannot be directly readout from the sensor array; instead, it will be reconstructed by computational algorithms. Compressive sensing techniques have been developed to increase the number of spectral channels that can be recovered from a single acquisition.

For grating/prism or resonant-cavity-based spectrometers, the free spectral range (FSR) sets an upper bound of wavelength range in one measurement. In sharp contrast, the random spectrometer does not have the FSR limit, because a disordered structure lifts all degeneracies. The probability of having identical output patterns at well-separated wavelengths is negligible. Furthermore, multiple scattering



**FIG. 3.** Conventional spectrometer vs random spectrometer. (a) A grating spectrometer maps individual wavelengths to different spatial positions. The wavelengths that miss the sensor array will not be detected at all. (b) A disordered structure generates a random scattering pattern unique for each wavelength, and no wavelength will miss the sensor array.

of light provides non-resonant broadband enhancement of wavelength resolution, enabling a chip-scale spectrometer with small footprint and fine resolution.

### 3. Multi-functional photonic devices

Complex optical systems, for example, disordered photonic nanostructures, multimode fibers with random refractive index fluctuations, have numerous degrees of freedom (DoFs) in space, time, spectrum, and polarization. Since these DoFs are coupled, it is possible to use the DoFs in one domain at input to control the output in another domain. For example, the transmission spectrum,[4,5] polarization state,[6–8] and temporal pulse shape[9–16] can be varied by shaping the spatial wavefront of incident light.[17] Hence, a complex system, in combination with a spatial light modulator (SLM), can function simultaneously as a temporal pulse shaper, a reconfigurable waveplate, a tunable spectral filter, and a programmable beam splitter.[18]

Inversely, a complex optical system allows recovery of information of an input signal in one domain by measuring the output light in a different domain. As an example, the spatial intensity distribution (speckle pattern) of transmitted light through a disordered medium or a multimode fiber encodes the information of spatial wavefront, spectrum, and polarization state of the incident wave. Such information of input may be retrieved from the output speckle measurement, meaning a single system can serve as a lens, a spectrometer, and a polarimeter. It is also possible to simultaneously recover information in multiple domains, for example, reconstructing both spatial and spectral distributions of a signal from one speckle pattern, enabling snapshot hyperspectral imaging.

### 4. Suppression of coherent imaging artifacts

Spatial coherence of laser emission introduces coherent artifacts like speckle noise, limiting the use of lasers as illumination sources in full-field imaging applications including wide-field microscopy, parallel projection, optical holography, and photolithography. A common method of reducing the spatial coherence of a laser is integrating many different speckle patterns generated by a time-varying scattering system like a rotating or vibrating diffuser [Fig. 4(a)]. Such scheme is slow and inefficient, as it starts with a coherent laser and then reduces the coherence with a diffuser outside the laser. A more direct and efficient approach is to design a laser with low spatial coherence by inserting a diffuser into the cavity, or more generally, by incorporating
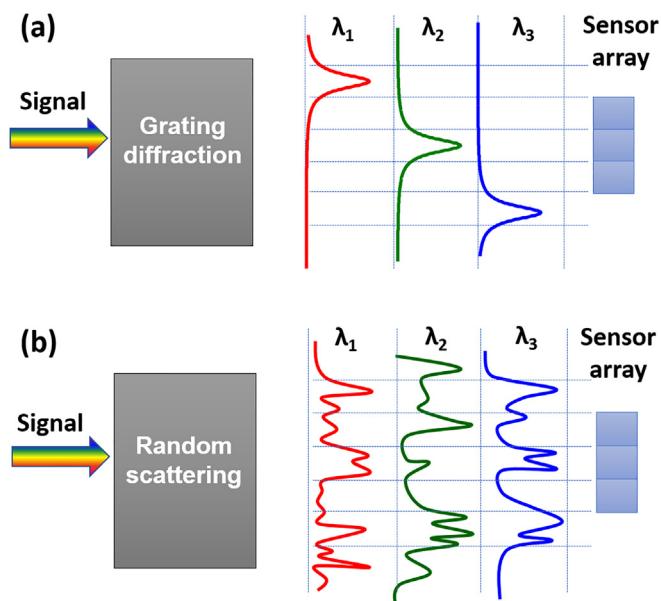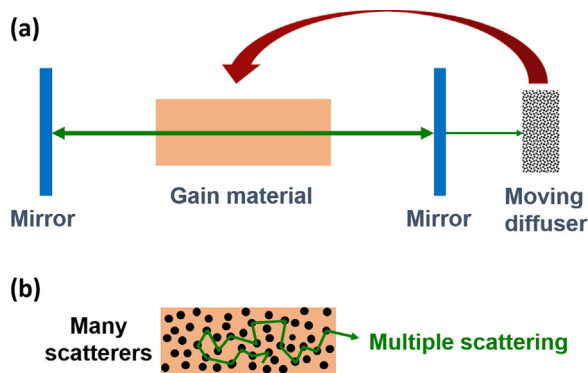
**FIG. 4.** Conventional laser vs random laser. A standard laser consisting of a gain material in between two mirrors produces spatially coherent emission. To avoid coherent imaging artifacts with laser illumination, the spatial coherence of laser emission is lowered by placing a moving diffuser outside the cavity. A more direct way of reducing the laser coherence is to inset the diffuser into the cavity (a) or incorporate many scatterers inside the gain material (b). Light amplification is enhanced by multiple scattering that increases optical path length inside the gain material.

scatterers to a gain material [Fig. 4(b)]. Such a laser is called a random laser, and it can produce emission with varying degrees of spatial coherence. Its brightness as a laser enables high-speed full-field imaging, and its relatively low spatial coherence rejects speckle and coherent crosstalk.

## B. Background

In this subsection, we will define relevant parameters and functions, and introduce physical phenomena and mechanisms that underlie the photonic devices in Secs. I B 1–I B 6.

### 1. Photonic systems with disorder

In this review, we consider mostly disordered photonic structures of varying parameters and dimensions. Examples are one-dimensional (1D) dielectric layers with fluctuating thickness/refractive index, two-dimensional (2D) arrays of cylindrical holes randomly distributed in a membrane, and three-dimensional (3D) packing of nanoparticles with irregular size and shape. In addition, we will include optical cavities featuring chaotic ray dynamics such as integrating spheres with rough inner walls, and optical fibers with structural inhomogeneities and refractive index variations.

### 2. Characteristic lengths of optical scattering

Light is scattered by a disordered structure with refractive index variation on the length scale of the optical wavelength. The scattering strength is characterized by the scattering mean free path $l_s$ and the transport mean free path $l_t$. The scattering mean free path $l_s$ is defined as the average distance that light travels between two consecutive scattering events. The transport mean free path $l_t$ is defined as the minimum distance a wave travels before its direction of propagation is completely randomized. These two length scales are related by

$$l_t = \frac{l_s}{1 - \langle \cos \theta_s \rangle}, \qquad (1)$$

where $\langle \cos \theta_s \rangle$ is the average cosine of the scattering angle $\theta_s$, which can be found from the differential scattering cross section. If the scattering particle size is smaller than the wavelength $\lambda$, Rayleigh scattering of light gives $\langle \cos \theta_s \rangle = 0$, and $l_t = l_s$. For larger scatterers, Mie scattering results in $\langle \cos \theta_s \rangle \approx 0.5$, and $l_t \approx 2l_s$.

### 3. Light diffusion and localization

In a scattering system of thickness $L_s$ that is less than $l_s$, light is scattered only once. When $L_s$ exceeds $l_s$, light is scattered multiple times. Once $L_s \gg l_t$, light transport can be described by diffusion. The total transmission (transmittance) is on the order of $l_t/L_s \ll 1$. Random walk of photons increases their path-lengths inside the scattering system. The average path length for transmitted light is $\langle \mathscr{L} \rangle \sim L_s^2/l_t$. Multiple scattering and light diffusion leads to a broad distribution of optical path-lengths $\mathscr{L}$, and its width $\Delta \mathscr{L}$ is comparable to the mean path length.

In 1D and 2D disordered systems, light will be localized, as long as the system size is sufficiently large (exceeding the localization length). It is hard to localize light in 3D disordered systems, even in the presence of strong scattering. Unlike the linear decay in the diffusive regime, the average transmission of light in the localization regime decays exponentially with the system thickness $L_s$. Almost all light will be reflected back, when absorption is negligible.

### 4. Multimode optical fiber

In a multimode fiber (MMF), intrinsic imperfections like refractive index variation along the fiber and external perturbations that cause fiber bending or twisting result in optical coupling between guided modes. Such coupling can be considered as optical scattering in the fiber modal space. The effective scattering mean free length $l_s$ is given by the average distance light travels in the fiber before hopping from one spatial mode to another. The effective transport mean free path $l_t$ is the minimum propagation distance beyond which light is spread over all fiber modes, no matter which mode is initially launched into. If the fiber length $L_{MMF}$ is shorter than $l_t$, then the mode coupling is weak. Once $L_{MMF} \gg l_t$, the mode coupling is strong enough to initiate a random walk of photons in the modal space. Since backscattering is negligible, light diffusion occurs in the modal space, namely, light always propagates forward in the fiber, but in different spatial modes.

The modal dispersion (group velocity dispersion) in a MMF broadens the path length distribution of transmitted light. If the mode coupling is weak, the width of optical path length distribution scales linearly with the fiber length, $\Delta \mathscr{L} \propto L_{MMF}$. In the strong coupling regime, light is scattered back and forth among the fiber modes, and the optical path length distribution is narrowed. Its width scales as $\Delta \mathscr{L} \propto \sqrt{L_{MMF}}$, as a result of diffusion.

### 5. Spectral correlation function

The speckle field pattern $E_p(r, \lambda)$, generated by coherent light transmitted through a random scattering medium, varies with wavelength $\lambda$. The spectral field correlation function is defined as

$$C_E(\Delta\lambda) \equiv \frac{\langle E_p^*(r,\lambda)\, E_p(r;\lambda+\Delta\lambda)\rangle_{r,\lambda}}{\langle |E_p(r;\lambda)|^2\rangle_{r,\lambda}} - 1, \qquad (2)$$

where $\langle\cdots\rangle_{r,\lambda}$ represents averaging over spatial position $r$ and wavelength $\lambda$. The spectral correlation function for speckle intensity, $C_I(\Delta\lambda)$, is equal to $|C_E(\Delta\lambda)|^2$, if non-local correlation is negligible. The full-width-at-half-maximum (FWHM) of $C_I(\Delta\lambda)$ is inversely proportional to the width of optical path length distribution $\Delta\mathscr{L}$. In a diffusive system without absorption, the spectral correlation width scales as $l_t/L_s^2$.

Similarly, $\Delta\mathscr{L}$ in a MMF determines how fast the transmitted speckle pattern decorrelates with wavelength. In a fiber with weak mode coupling, the spectral correlation width scales as $1/L_{\mathrm{MMF}}$. With strong mode coupling, the scaling is changed to $1/\sqrt{L_{\mathrm{MMF}}}$.

If the input light has a bandwidth narrower than the spectral correlation width, it can be considered as "monochromatic" in terms of transport through a scattering medium or a MMF. The transmitted speckle, if fully developed, has an intensity contrast $C_t \equiv \sigma_I/\bar{I}_s = 1$, where $\sigma_I$ is the standard deviation of intensity, $\bar{I}_s$ is the mean intensity. For a broadband input whose bandwidth is $N_\lambda$ times of the spectral correlation width, the transmitted intensity pattern is an incoherent sum of $N_\lambda$ distinct speckle patterns, and the speckle intensity contrast $C_t$ is reduced to $1/\sqrt{N_\lambda}$.

### 6. Optical memory effect

The angular memory effect in random scattering systems, also referred to as intrinsic isoplanatism, is a key physical phenomenon that has been widely used for optical imaging, metrology, and communication through turbid media. When the spatial wavefront of a coherent beam incident on a disordered slab is tilted by a small angle, the transmitted wavefront is tilted by the same angle, leading to a lateral translation of the far-field speckle pattern. The angular memory effect exists in both single-scattering and multiple-scattering systems. The angular range of memory effect is inversely proportional to the system thickness, and thus, a thin diffuser has a large memory effect range.

Consider a diffusive slab of width much larger than its thickness $L_s$, a point excitation at the front surface of the slab emerges as a diffusive halo of radius $\sim L_s$ at the back surface. This lateral spread determines the angular range of memory effect, $\Delta\theta_m = \lambda/(2\pi L_s)$. The angular memory effect also exists for light reflected from the slab. Since the penetration depth is on the order of transport mean free path $l_t$, the angular range of memory effect in reflection is approximately $\lambda/(2\pi l_t)$.

### C. Scope

This review aims to illustrate why structural disorder is useful for photonic device applications, and how it has been incorporated to both passive and active devices. Here, we focus on the methods and mechanisms of utilizing "randomness" (natural disorder) to enhance device performance and add new functionality, without relying on "controlled" disorder. Even when structural disorder is intentionally introduced to a device, the exact configuration is not necessarily known. The disorder is neither correlated nor engineered.

In this review, we start with passive devices (Secs. II–VII) and then move to active ones (Sec. VIII). One category of disordered photonic device applications is information security and optical computing. Section II describes the construction of optical physical unclonable functions with random complex systems for secure key generation. The emerging applications of disorder for optical computing and artificial neural network are discussed in the last section (Sec. IX).

Another category of disordered device applications is imaging and sensing. In Secs. III–VII, random systems are employed to retrieve spatial, spectral, temporal, and polarization information of light fields, so that they function as optical lens (Sec. III), spectrometer or wavemeter (Sec. IV), polarimeter (Sec. VI), and RF receiver (Sec. VII A), and are also used for optical pulse measurement and full-field recovery (Sec. VII B). Multi-functional devices are developed for hyperspectral imaging (Sec. V), and spatial and spectral polarimetry (Sec. VI). These applications require the random systems to have static structures and constant environments. If the illuminating light is fixed, the optical response of a random system can be used to monitor environmental change, and disorder-induced light scattering will enhance the sensitivity, as shown in Sec. IX A.

Shifting from passive devices to active devices, we will introduce random lasers and their applications for speckle-free imaging and super-resolution spectroscopy in Sec. VIII. This section also presents remarkable performance that random fiber lasers have achieved in terms of high-power generation and ultra-broad frequency tunability, as well as the unexpected suppression of lasing instabilities by disorder.

Figure 5 presents a roadmap of this review. In Table I, the disordered photonic devices covered in this review are summarized.

The scope of this review is restricted to *intentional* use of disorder for photonic *device* applications. To provide a tutorial for newcomers, our review of existing works does not follow the chronological order. For related topics that are not covered here, there are excellent reviews and books regarding fundamental physics of light scattering and wave transport in disordered systems,[19–25] control of light transport by wavefront shaping,[17,26,27] mitigating the effects of naturally occurring disorder and optical scattering for imaging and sensing applications,[28–31] disordered photonics and optics[32,33] in general, and correlated and engineered disorder[34–36] in specific.

## II. PHOTONIC PHYSICAL UNCLONABLE FUNCTIONS

In this section, we introduce different types of optical physical unclonable functions (PUFs) that have been developed with random, chaotic systems for physical key generation. After a brief introduction of PUFs in Sec. II A, we describe the strong optical PUFs based on linear light scattering (Sec. II B) and show how the PUFs can be made reconfigurable (Sec. II C). To enhance security, nonlinear PUFs (Sec. II D) and quantum readouts (Sec. II E) are developed. Finally, we discuss strong photonic PUFs (Sec. II F) and weak ones (Sec. II G).

### A. Introduction of PUFs

The physical unclonable function (PUF), originally named physical one-way function, is the modern realization of a physical key. It represents an unpredictable yet deterministic physical system that creates a reproducible output for a given input. The input-to-output mapping is unique for every token and is characterized by implementing a challenge-response protocol. The PUF is interrogated with a list of input signals called challenges, and the output signals, called responses, are recorded and processed. An applied challenge and the measured
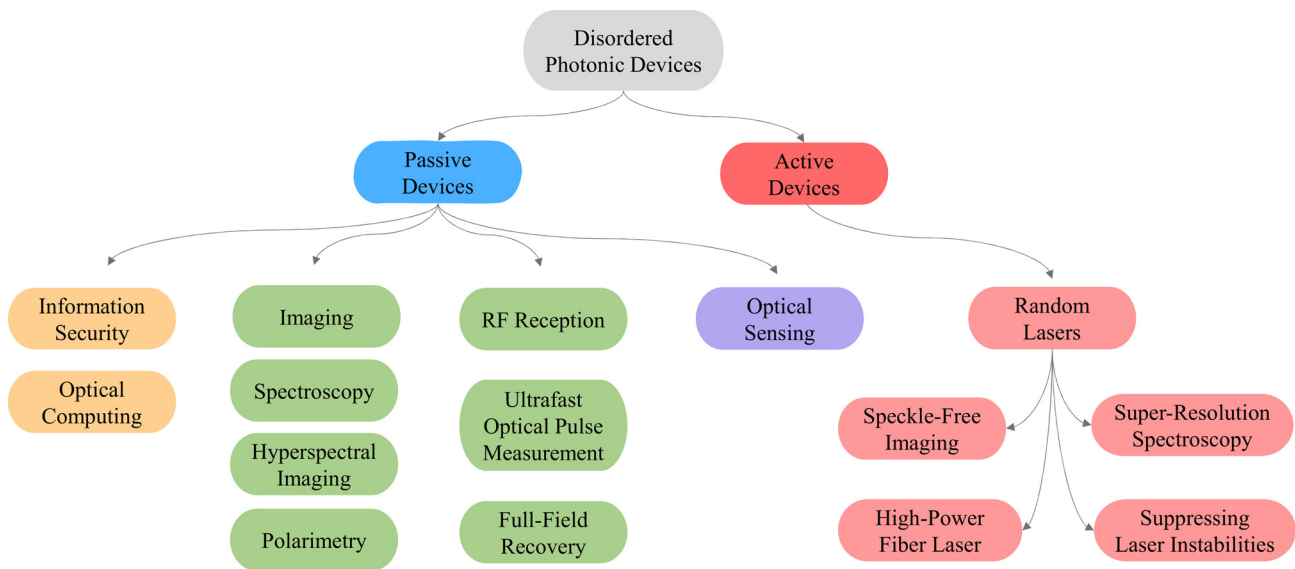
**FIG. 5.** Roadmap of this review. The review covers both passive and active disordered devices for various photonic applications. The passive devices are grouped according to information security and computing, imaging and metrology and sensing applications. The active devices are a group of disordered lasing applications.

response are referred to as a challenge–response pair (CRP). During the enrollment phase, a challenge-response library is created. Based on the maximum size of the library, PUFs are classified as weak PUFs or strong PUFs. Strong PUFs differ from their weak counterparts by an extremely large CRP space, which is fully accessible to any user or attacker and impossible to entirely readout in feasible time. The challenge–response mapping is so complex that the response to a fresh challenge is hard to predict.

In general, PUFs exploit the unique and inherent randomness of physical micro-structures originating from fabrication and environmental conditions for authentication and information security.[37,38] Optical PUFs, in particular, utilize various optical processes in disordered structures for interrogation and readout.[39] This section reviews the developments of photonic PUFs, with a focus on strong PUFs.

### B. Linear scattering PUFs

The first optical PUF is realized with a three-dimensional (3D) bulk of randomly packed glass spheres[2] serving as a token (Fig. 2). When a laser beam is incident to the token, light experiences multiple scattering. The interference of scattered waves generates a random grainy intensity profile—a speckle pattern.[40] With static scatterers, the optical scattering is a deterministic linear process. The resulting speckle pattern is reproducible for a fixed scatterer's configuration and a given illumination condition. The PUF challenge is set by the illumination conditions such as wavelength, spatial location, and incident angle of the laser beam. The PUF response is a digitized bit string extracted from the speckle pattern of transmitted/reflected light.

Such an optical PUF has a very large number of possible challenges.[2,41] Consider a scattering slab with a cross section area of $1 \, \text{cm}^2$ and thickness of 2.5 mm. A monochromatic light at the wavelength of 500 nm can be coupled into any one of the $10^9$ spatial modes at the input facet to produce a distinct output speckle pattern. This enormous

space renders the complete readout of all challenge–response pairs (CRPs) an extremely challenging task, even if an adversary holds physical possession of the PUF for a considerable time.

While it is easy to fabricate a 3D scattering PUF, it is impossible to clone one with the state-of-the-art technology. A $0.25\text{-cm}^3$ token consists of $10^{11}$ scattering particles of average diameter $\sim 1 \, \mu\text{m}$. These particles are randomly packed in a 3D volume and have polydisperse size and irregular shape. It is extremely difficult to accurately determine their position, size, and shape, let alone duplicate them with high precision. Even with the exact knowledge of the entire 3D structure, it is impossible to numerically calculate the response to a given challenge in a reasonable time. Since the speckle pattern is very sensitive to any modification of the scattering structure, the PUF is intrinsically tamper-resistant.[2,41,42]

To this day, the optical scattering PUF has withstood any machine learning-based modeling attacks,[41] while most existing electronic PUF architectures have failed.[39] In such attacks, machine learning (ML) algorithms are trained with a subset of the CRP space to extrapolate and predict the entire space. The resistance of optical scattering PUFs to ML attack attempts is achieved by interrogating different spatial regions of a random bulk material. The interrogation of different spatial regions where the scattering structure is entirely different yields new speckle patterns, uncorrelated to the previous patterns that the algorithm has already learned.

Therefore, the extraordinary complexity of random-scattering optical PUF provides an unprecedented security level; however, it comes at the cost of a large device size and lack of electronic integration. Moreover, the response repeatability or reliability requires a submicrometer precision in positioning the token with respect to the interrogating beam and the camera, which is difficult to implement in a cost-effective way.

To overcome these issues, miniaturization and integration of optical scattering PUFs to electronic circuits have been explored.[41,43,44]

TABLE I. Detailed summary of the disordered photonic devices covered in this review.

| Device | Functions | Disorder-enabled features | Type | Sections |
|---|---|---|---|---|
| Physical unclonable function (PUF) | Secret key generation | Extraordinary complexity, reconfigurability, high security, robustness against attacks | Passive | II |
| Optical computing | Random projection, reservoir computing | High dimensionality, scalability, reconfigurability | Passive | IX B |
| Random lens | Spatial imaging, light focusing | Enhanced spatial resolution, enlarged field-of-view | Passive | III |
| Speckle spectrometer, wavemeter | Spectrum reconstruction, wavelength identification | Overcoming the trade-off between device size and spectral resolution, elimination of free-spectral range | Passive | IV |
| Hyperspectral imager | Spectrally resolved imaging | Single acquisition, flexible adjustment of spatial–spectral trade-off, insensitivity to optical (mis)alignment | Passive | V |
| Scattering polarimeter | Spatially and/or spectrally resolved polarimetry | Retrieval of spatial, spectral and polarization information with a single speckle pattern | Passive | VI |
| Compressive RF receiver | Radio-frequency reception | Breaking Nyquist sampling limit with compressive sensing technique | Passive | VII A |
| Optical pulse measurement | Pulse shape recovery, full-field measurement | Time-integrated measurement, reference-free, removal of ambiguity in the direction of time | Passive | VII B |
| Optical sensor | Monitoring of temperature, pressure, mechanical motion, refractive index variations | High sensitivity, multi-functional sensor, simple implementation | Passive, active | IX A |
| Random laser illumination source | Speckle-free full-field imaging | High spectral radiance, low spatial coherence, fast decoherence, short integration time | Active | VIII B and VIII C |
| Super-resolution spectroscopy | Sparse spectral sampling with random lasing peaks | Breaking the spectrometer resolution limits | Active | VIII D |
| Fiber random laser | High power generation | High efficiency, clean output beam, nearly octave wavelength tuning | Active | VIII E |
| Disordered semiconductor laser | Stable lasing dynamics | Suppression of temporal instability over a wide range of pump power | Active | VIII F |

In one proposal, the PUF challenge space is comprised of illumination patterns generated by an integrated spatial light modulator or an array of phase-locked laser diodes. However, integrable optical PUFs are vulnerable to modeling and ML attacks, because of the reuse of a compact scattering volume and the linear nature of the optical scattering process.[41] Once the linear relation between the input field and the output field is characterized or learned, the response to any challenge can be predicted.

### C. Reconfigurable optical PUFs

One way to avoid the reuse of a scattering structure is to reconfigure the scattering structure and increase the structural diversity. This is done by heating a polymer containing randomly distributed scattering particles with an intense laser beam.[45] Once the polymer melts locally, the scattering particles change their position and subsequently freeze after cooling down. Alternatively, a polymer-dispersed liquid crystal film is reconfigured with the application of an electrical voltage

in a short amount of time.[46] The reconfigured scattering potential is uncorrelated with respect to its prior, effectively erasing the old PUF and creating a new one. This property of total erasability allows a complete destruction of the old PUF and prevents the abuse of a security device that falls into adversarial hands. While both reconfiguration schemes generate new unpredictable structures, they cannot return to the old ones. Such irreversible reconfigurability allows a single PUF-carrying hardware to be refreshed and employed by different customers sequentially. However, in between the reconfiguration operations, the input–output mapping remains linear, making the PUF vulnerable to ML attacks.

### D. Nonlinear optical PUFs

Given the vulnerabilities of linear optical PUFs, optical nonlinearities in a silicon chip are harnessed for the construction of an integrated PUF.[47,48] The nonlinear optical PUF exploits ultrafast nonlinear light–matter interactions in a two-dimensional (2D)

microcavity.[47] The cavity shape is designed to induce chaotic ray dynamics, and air holes are arbitrary positioned within the silicon cavity to cause light scattering (Fig. 6). Despite the state-of-the-art fabrication techniques, the microcavities possess inevitable structural and compositional idiosyncrasies that cannot be duplicated. The PUF challenges are encoded in the spectrum modulations of femtosecond laser pulses. Once the pulses are injected into a silicon microcavity, their high intensities trigger nonlinear optical processes including Kerr effects and free-carrier absorption. The output pulses are spectrally filtered and digitized to provide the PUF responses. The nonlinear input–output relation makes the PUF robust against ML attacks.[48]

### E. Quantum readout

The aforementioned PUFs use classical light for readout, and thus, they are vulnerable to emulation attacks.[37] Despite an enormous number of possible CRPs, only a small portion can be characterized and stored in a database. Once an adversary gains access to the challenge–response database, it is possible to intercept the challenges and produce the correct responses, if the interrogation is conducted with classical light. To defend against the digital emulation, quantum readout of PUFs is introduced.[49] The challenges are high-spatial-dimension states of light with only a few photons. When the number of spatial modes exceeds the number of photons, it is impossible for an adversary to fully determine the challenge and therefore to construct the expected response.[50] This scheme no longer depends on the secrecy of any stored data.

### F. Strong PUFs

Strong PUFs have been realized in various optical systems, with no means of cloning. In addition to disordered photonic nanostructures, random coupling of spatial modes in an optical fiber/waveguide is explored for PUF construction[51,52] and classical[53] or quantum[54] key establishment. Beyond the spatial domain, spectral features created by

disorder in an optical waveguide are exploited for an integrated photonic PUF.[55] More recently, a disordered metasurface embedded with perovskite quantum dots provides fluorescent speckle patterns with enormous encoding capability.[56] While it has been mostly used to attack PUFs, deep learning is employed in optical PUF generation to improve reliability and unpredictibility.[57]

Since the photonic PUFs are unique, unpredictable, reproducible (only by themselves), unclonable (even by manufacturers), one-way (non-invertible), and tamper evident, they offer a broad and versatile application spectrum. Optical strong PUFs enable remote authentication of both objects and data.[48,58] Protocols and systems have been proposed and demonstrated for their applications in encryption and secure communication.[59–62]

### G. Weak PUFs and unique objects

Optical weak PUFs are another form of storing secret keys in a vulnerable optical system. In contrast to strong PUFs, weak PUFs have small fixed CRP libraries with a challenge–response interface that is kept access-restricted from attackers.[63] In addition, there are optical unique objects (UNOs),[64,65] which are open-access fingerprints that have been developed for product authentication, tracking, and anti-counterfeiting. Almost all paper documents, plastic cards and product packaging contain a unique physical identity code formed from microscopic imperfections in the surface, which can be read from a reflected image.[66–68] Beyond the intrinsic "fingerprint," various disordered structures are engraved or attached to objects and function as optically readable, unforgettable tags/labels. Examples include randomly deposited plasmonic nanoparticles[69] and femtosecond laser filament-induced scattering surfaces.[70] The readout is not limited to optical scattering patterns, fluorescence patterns, or laser emission patterns provide unique responses as well. Examples are excitation-selected lanthanide luminescence from zeolites dispersed in polymer films,[71] random nanowire arrays with size-dependent dual lasing emission.[72]
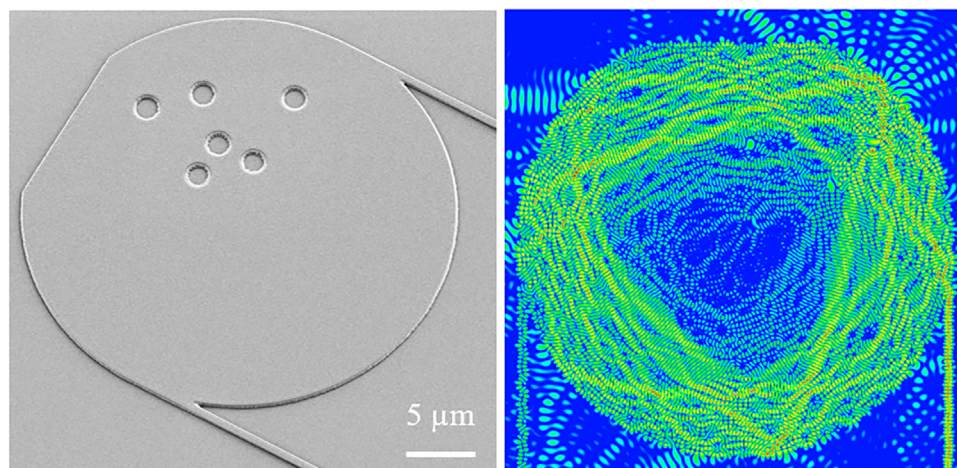


**FIG. 6.** Nonlinear optical PUF for enhanced security. Reprinted with permission from Grubel *et al.*, Opt. Express **26**, 4710 (2018). Copyright 2018 The Optical Society. (Left) Scanning electron microscope (SEM) image of a two-dimensional optical cavity with input and output waveguides fabricated in a silicon wafer. The cavity boundary shape introduces chaotic ray dynamics and the randomly positioned air holes inside the cavity cause light scattering. (Right) Simulated intensity distribution in the cavity, created by an input pulse, revealing chaotic ray dynamics. The short pulse induces optical nonlinearity inside the cavity, increasing the complexity of the response. While the challenge is encoded in the input spectrum modulation, the response lies in the output spectrum.

Edible photonic UNOs made of fluorescent biomaterials, which can be directly attached to the surface of medicines, are proposed for pharmaceutical anti-counterfeiting.[73]

## III. RANDOM LENS

In this section, disorder is intentionally introduced for optical imaging and light focusing to enhance the spatial resolution and the field of view. After a brief introduction of random lens imaging (Sec. III A), we describe its transfer function for coherent and incoherent illumination (Sec. III B). The random lens often combines with compressive sensing or machine learning for image recovery, as detailed in Sec. III C. Without calibration of its transfer function, random lens has been used for imaging based on cross-correlation or auto-correlation (Sec. III D). In addition, reference-free holographic imaging and wavefront sensing are realized with pseudo-random masks or thin diffusive layers (Sec. III E). Furthermore, light focusing by a random lens in combination with a spatial light modulator can enhance the spatial resolution of fluorescence microscopy (Sec. III F). The imaging techniques developed with random lens are adopted to multimode optical fibers with uncontrolled mode/polarization mixing and disordered fibers for endoscopic imaging (Sec. III G).

### A. Lens imaging

A conventional lens, designed for two-dimensional (2D) imaging, focuses light from one point on the object plane to a point on the image plane [Fig. 7(a)]. The spatial resolution is determined by the angular range $\theta_{max}$ of light that is captured by the lens, which corresponds to the numerical aperture (NA) of the lens. The field of view (FOV) depends on the lateral dimension of the sensor area of the
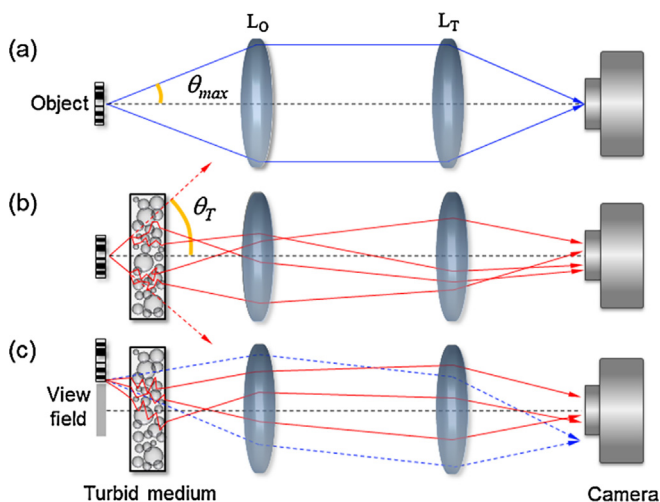


**FIG. 7.** Conventional lens vs random lens. Reprinted with permission from Choi *et al.*, Phys. Rev. Lett. **107**, 023902 (2011). Copyright 2011 The American Physical Society. (a) Conventional imaging with an objective ($L_O$) and a tube ($L_T$) lenses. $\theta_{max}$ is the maximum angle of light captured by the objective lens, which determines the spatial resolution. (b) After inserting a disordered medium, the waves of original angle $\theta_T$ exceeding $\theta_{max}$ can be captured after being scattered and redirected, so spatial resolution is enhanced. (c) The field of view (FOV) is also increased by scattering, as some of the scattered waves from an object outside the conventional FOV will reach the camera.

camera as well as the image magnification. Such a lens faces a trade-off between the spatial resolution and the field of view. As the diffraction-limited resolution increases with the NA of the lens, the field of view shrinks.

A random lens,[74] also called opaque lens,[75] turbid lens,[76] scattering lens,[77] or diffuserCam,[78] is an unconventional imager comprised of a disordered structure. As schematically illustrated in Fig. 7, incorporating a random scattering medium to an imaging system brings several advantages.[76] First, the spatial resolution is enhanced by an effective increase in the NA, since light emitted from the object at large angles that would miss the camera can be redirected by the random lens back to the camera [Fig. 7(b)]. Second, the field of view is enlarged, because light from any point on the object is scattered into many directions, and some of which will reach the camera [Fig. 7(c)]. Third, volumetric (3D) imaging is possible with a planar (2D) sensor array, as objects at different axial planes will generate distinct scattering patterns at the sensor plane.[79]

The typical image projected by a random lens onto a camera is a seemingly random pattern with little resemblance to the object. Computational models and algorithms, based on compressive sensing and machine learning, must be employed for random lens calibration and image reconstruction. The quality of reconstructed images relies heavily on algorithms that shift the burden from the hardware to software and make the imaging system much cheaper. The lenses comprised of disordered structures not only reduce the hardware cost, but also expand the space of imaging system designs and add novel imaging functionalities.

A closely related topic is imaging through random scattering media, which has attracted much attention and investigation in recent years.[17,27–31] These studies aim to mitigate the effects of unwanted scattering that scrambles the image. In contrast, random lenses exploit disorder and scattering for focusing and imaging applications. Their implementations benefit from techniques and algorithms developed for imaging through random media.

### B. Transfer function

Depending on the coherence of illuminating light and the response of an object, optical imaging is either coherent or incoherent. With the many-to-one mapping of a random lens, light from different positions of an object can reach the same pixel of the camera. If the fields are mutually incoherent, their intensities will be added, and the transfer function relates the intensity distribution over the camera to every point across the object. However, if the fields from the object are coherent, they will interfere on the camera, and the transfer function maps the field from the object to the camera.

#### 1. Coherent imaging

The transfer function of a random lens $\mathbf{M}_F$ maps the field distribution across an object $\mathbf{E}_{in}(\mathbf{r})$ to that over a camera $\mathbf{E}_{out}(\mathbf{r})$,

$$\mathbf{E}_{out}(\mathbf{r}) = \mathbf{M}_F \cdot \mathbf{E}_{in}(\mathbf{r}). \quad (3)$$

$\mathbf{M}_F$ is a complex matrix of dimension $N_o \times N_i$, where $N_i$ and $N_o$ denote the number of input and output channels. For a conventional lens, $\mathbf{M}_F$ is a diagonal matrix; but for a random lens, its off-diagonal elements do not vanish. After $\mathbf{M}$ is calibrated, the field distribution across an object can be reconstructed from the measured field pattern

on the camera:[76] $\mathbf{E}_{\text{in}} = \mathbf{M}_{\text{F}}^{-1} \cdot \mathbf{E}_{\text{out}}$. However, the matrix inversion $\mathbf{M}_{\text{F}}^{-1}$ is unstable in the presence of noise. Tikhonov regularization is applied to obtain an approximate solution.[80] The image reconstruction can be further improved by illuminating the object with different wavefronts[81] or increasing the number of detected channels.[80]

To reach a sub-wavelength resolution, a random lens made of closely packed nanoparticles is placed in close proximity of an object.[82] The evanescent waves from the object, which carry high spatial frequency components, are converted to propagating waves via scattering with nanoparticles in the random lens, and sub-wavelength resolution is achieved with far-field detection. The near-field to far-field transfer function is calibrated using the near-field scanning optical microscope (NSOM).

### 2. Incoherent imaging

If an object is illuminated by spatially incoherent light or it produces an incoherent signal such as fluorescence upon coherent excitation, the transfer function that maps *intensity* distribution from the object to the camera is a real, positive matrix. The first implementation of a random lens is a disordered array of small mirrors,[74] and the transfer function is modeled by geometric ray optics. The random lens is also combined with a pinhole camera for sparkle vision.[83,84] While a diffusive layer can provide a larger angle of light collection via multiple scattering, the low transmission leads to a poor signal to noise ratio (SNR). Thin diffusers or random phase masks have much higher transmission and better SNR. Moreover, they possess a larger range of the memory effect.

Because of the angular memory[85,86] (intrinsic isoplanatism), a lateral displacement of a point source will not change the scattering pattern but only translate it laterally at the sensor plane [Fig. 8(a)]. The point spread function (PSF) $P(\rho', z'; \rho, z)$ describes the intensity distribution on the sensor array $(\rho', z')$ generated by a point source at $(\rho, z)$. $z$ denotes the distance from the source to the random lens, and $z'$ from the lens to the sensor. With the origins of transverse coordinates $\rho$ and $\rho'$ on the $z$-axis, the angular memory effect is expressed as



**(a)** Lateral dependence of the PSF

**(b)** Depth dependence of the PSF

**FIG. 8.** Point spread function (PSF) of scattering lens. Reprinted with permission from Antipa *et al.*, Optica **5**, 1 (2018). Copyright 2018 The Optical Society. The PSF is given by the far-field intensity pattern created by light from a point source propagating through a thin scattering layer. (a) The PSF translates laterally as the point source shifts in the lateral direction. (b) The PSF rescales as the point source moves in the axial direction. Such effects greatly simplify the PSF calibration process of a thin scattering lens.

$$P\left[\rho' - (z'/z)\,\Delta\rho, z'; \rho + \Delta\rho, z\right] = P(\rho', z'; \rho, z). \qquad (4)$$

Furthermore, an axial shift of the point source rescales the PSF in the case of single scattering (light is only scattered once by the random lens), as shown in Fig. 8(b). Such memory effects greatly simplify the PSF calibration process.[78]

Since any object can be considered as a sum of point sources $O(\rho, z)$, the detected intensity distribution is a convolution of the object with the PSF,

$$I_{\text{det}}(\rho', z') = \int O(\rho, z)\, P(\rho', z'; \rho, z)\, d\rho\, dz \equiv O * P, \qquad (5)$$

where $*$ denotes the convolution operation. The deconvolution with known PSF reconstructs a 3D object from a 2D image. Although the raw data are collected on a fixed sensor grid, one can choose a nonuniform 3D reconstruction grid arbitrary. This choice is crucial for efficient reconstruction without resolution loss.[78] In contrast to the traditional imaging system whose resolution is independent of the scene, the image reconstruction using nonlinear algorithms may degrade the effective resolution as the scene complexity increases. As a result, the two-point resolution is often better than the multi-point resolution.

While the above expressions are given for incoherent imaging, a similar expression can be obtained for coherent imaging by replacing the intensity with a complex field.

### C. Compressive sensing and machine learning

The random lens may be regarded as a parallel implementation of the single-pixel camera developed for compressive sensing, as illustrated in Fig. 9. In the field of compressive imaging, pseudo-random masks have been extensively used to sample objects, because they are uncorrelated with any mathematical basis in which the object images have sparse representations. In contrast to the single-pixel camera which projects the signal from an object onto different pseudo-random masks sequentially, the random lens enables simultaneous projections onto multiple camera pixels in a single acquisition.

Compressive sensing algorithms allow image reconstruction of sparse objects, when the number of sensors is significantly smaller than the number of sampling points on the object.[78,79,81] The compression ratio depends on the relative sparsity of the object.[81] Such compression is essential to achieve volumetric imaging of a 3D object with a 2D detector array.[78]

Machine learning has recently been applied to imaging through scattering media and light control.[87–94] The main goal is to "learn" the transfer functions of unknown structures in the presence of noise.[95,96] Such learning can make the random lens robust against external perturbations that modify the transfer function, avoiding frequent re-calibration.

### D. Correlation-based imaging

To skip the transfer function characterization, correlations among scattered waves have been employed for imaging with a random lens of unknown structure. Starting with the initial proposal of a "wall lens,"[97,98] several schemes have been proposed and realized over the years.
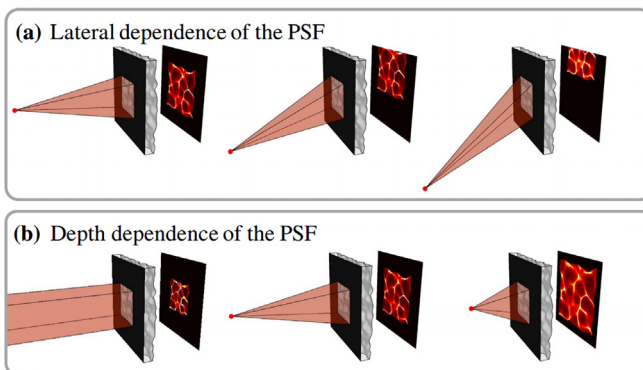
**FIG. 9.** Compressive imaging with random lens. Reproduced with permission from Liutkus *et al.*, Sci. Rep. **4**, 5552 (2014). Copyright 2014 Author(s); licensed under a Creative Commons Attribution (CC BY) license. (a) Classical Nyquist–Shannon sampling: waves originating from an object of size *N* are captured by an array of *M* = *N* sensors. (b) Single-pixel camera: an object is sampled by M successive random projections onto a single sensor using a digital multiplexer. (c) Imaging with a random lens: *M* sensors simultaneously capture different random projections of the original object. In (b) and (c), sparse objects can be reconstructed with *M* < *N*.

### 1. Cross-correlation

The first method utilizes the correlation between the random lens output from a reference wave and that from the signal to recover the object. The reference wave is not necessarily coherent with the

signal from the object.[97,98] As illustrated in Fig. 10(a), a point source at $(\rho, z)$ serves as the reference, its spherical wavefront impinges on the random lens (a scattering layer), and the transmitted or reflected intensity distribution provides the PSF, $P(\rho, z; \rho', z')$. It is then correlated with the intensity distribution $I_{\text{det}}(\rho', z')$ created by an object
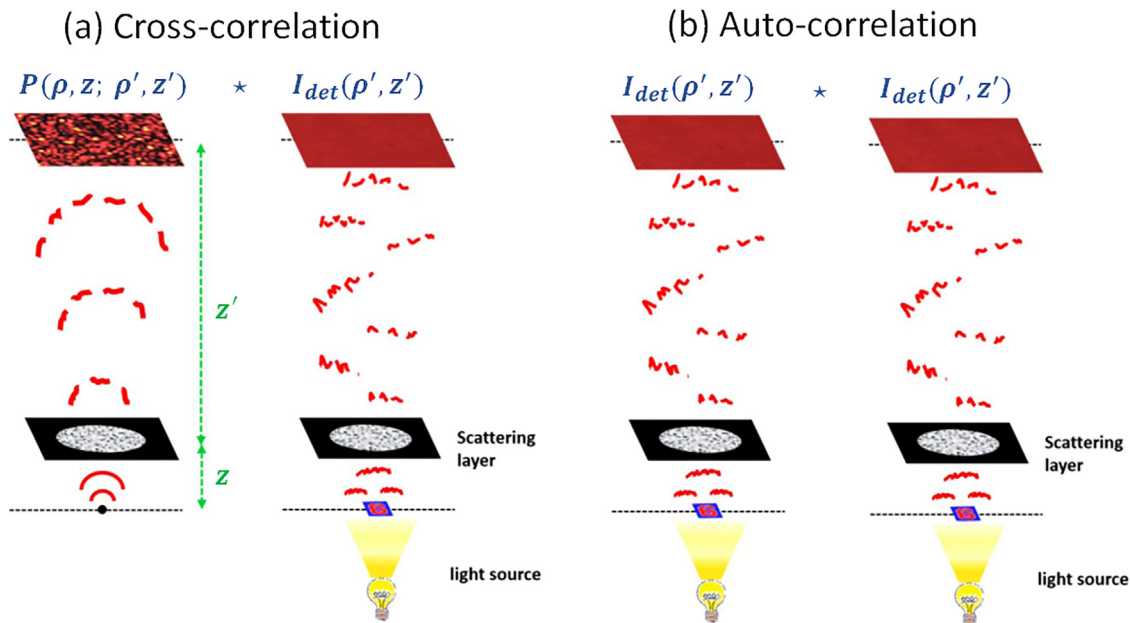


**FIG. 10.** Correlation-based imaging with random lens. Reproduced with permission from Singh *et al.*, Sci. Rep. **7**, 10687 (2017). Copyright 2017 Author(s); licensed under a Creative Commons Attribution (CC BY) license. (a) Cross-correlation between the point spread function (PSF) created by a point source, $P(\rho, z; \rho', z')$ and the image of an object through a thin scattering layer, $I_{\text{det}}(\rho', z') = O * P$, recovers the object $O(\rho, z)$ [see Eq. (6)]. (b) Auto-correlation of $I_{\text{det}}(\rho', z')$, $I \star I$, is equal to $O \star O$, from which $O$ is retrieved [see Eq. (7)].

$O(\rho, z)$. Although the reference wave and the object wave do not interact directly, they interact indirectly via the random lens. Since $I_{det}$ is the convolution of the object $O$ and the PSF $P$, the cross-correlation between $I_{det}$ and the reference $P$ gives

$$I_{det} \star P = (O * P) \star P = O * (P \star P) = O, \tag{6}$$

where $\star$ denotes the correlation operation, and the auto-correlation of the PSF $(P \star P)$ can be approximated by a Dirac delta function $\delta$ whose convolution with $O$ gives $O$.

In principle, the volumetric image of a 3D object can be constructed from the cross-correlation of 3D intensity distributions generated by the random lens with the reference source and the object separately. In reality, a 2D sensor array is often used to record the intensity distribution on a single plane. From it, a sharp image of a 2D object or cross section of a 3D object with distance to the random lens $z_{obj}$ equal to that of the reference source to the lens $z_{ref}$ is retrieved.[99] The random lens satisfies the same imaging condition as a conventional lens: $1/z + 1/z' = 1/f$, where $z = z_{obj} = z_{ref}$ is the working distance from the object to the random lens, $z' = z_{det}$ is the distance between the detector plane and the random lens, and $f$ is the effective focal length.[97,98] While a conventional lens has a fixed focal length, the random lens has an adaptive focal length that adjusts itself for arbitrary chosen $z$ and $z'$. The lateral magnification $m = -z'/z$ is independent of wavelength $\lambda$, even though the transmitted/reflected intensity pattern changes with $\lambda$. Hence, the magnification can be increased by moving the random lens away from the detector toward the object. The lateral resolution is given by RES $\simeq 1.22 \lambda z / D_a$, where $D_a$ is the diameter of the input aperture on the random lens. By bringing an object closer to the random lens or by increasing the aperture diameter, RES decreases and the resolution is enhanced.

The field of view (FOV) is limited by the range of angular memory effect.[97,98] If light transport in the random lens is diffusive, FOV $\simeq \lambda z / \pi L_s$, where $L_s$ is equal to the thickness of the lens when operating in the transmission mode or the transport mean free path in the reflection mode. The FOV depends on the working distance $z$ from the object to the random lens. The depth of field DOF is proportional to $\lambda (z'/D_a)^2$ and is independent of the working distance $z$.[99] Similar to a conventional lens, the random lens has a trade-off between the lateral resolution RES and the field of view FOV: FOV/RES $\sim D_a/L_s$. However, this trade-off is achromatic with no dependence on wavelength.

### 2. Auto-correlation

While it does not require the calibration of a random lens, cross-correlation-based imaging does require a known reference, which may not be possible in some cases. An auto-correlation method, originally invented for noninvasive single-shot imaging through scattering medium,[100,101] is adopted for random lens imaging without a reference. Let us consider incoherent imaging with a random lens, $I_{det} = O * P$, in Fig. 10(b). The auto-correlation of $I_{det}$ is equal to the auto-correlation of the object $O$,

$$I_{det} \star I_{det} = (O * P) \star (O * P) = (O \star O) * (P \star P) = O \star O. \tag{7}$$

The Fourier transform $\mathscr{F}\{I_{det} \star I_{det}\} = \mathscr{F}\{O \star O\} = |\mathscr{F}\{O\}|^2$ gives the amplitude of Fourier transform of $O$, $|\mathscr{F}\{O\}|$. The phase of

$\mathscr{F}\{O\}$ can be retrieved numerically, under the object constraints. The reconstructed $\mathscr{F}\{O\}$ gives $O$ via an inverse Fourier transform.

Typically, the phase retrieval algorithms work efficiently for sparse objects. However, for objects with large size, low sparsity, and high complexity, the image contrast is low, as $I_{det}$ is an incoherent sum of many shifted PSF. The low contrast restricts the size and complexity of the object that can be reconstructed using a phase-retrieval algorithm. To circumvent this difficulty, a reference point source is added to the scene:[102,103] $O(\rho) + \delta(\rho - \rho_0)$. Unlike the cross-correlation method described above, there is no need to measure the random lens output when illuminated only by the point source (without the object). The autocorrelation of random lens output $I_{det}$, taken with both the object and the reference present, gives two spatially offset copies of the object, $O(\rho - \rho_0)$ and $O(\rho + \rho_0)$. This method permits direct reconstruction of the object without phase retrieval.

### E. Holographic imagers and wavefront sensors

In parallel to random lens developments, pseudo-random masks are adopted in reference-free holographic imaging, also called phase imaging.[104–110] Unlike most random lens, the amplitude or phase pattern of a mask is usually known by design and its transfer function can be predicted. To probe the phase front from the intensity measurement, light from an object is diffracted by the mask, and the interference of waves from different positions on the phase front produces intensity modulations. This step encodes phase information into intensity variation. The transmitted/reflected intensity patterns are recorded at one or several planes, from which the incident field to the mask is reconstructed. While recording multiple intensity patterns at different planes guarantee a unique, accurate, and fast-convergent reconstruction, single-plane recovery is possible for sparse objects. The "randomness" in the mask (aperture) eliminates any possible symmetry or degeneracy in the interference pattern, thus avoiding stagnation or ambiguity in the phase recovery.

Since the phase-retrieval is an iterative process, it takes time to converge, posing a challenge for real-time imaging and tracking. To address this issue, the intensity pattern without any object is recorded first, and then, the change of pattern caused by insertion of an object is used for full-field (amplitude and phase) reconstruction in a single (non-iterative) processing step.[107]

In addition to pseudo-random masks, a thin diffusive layer with an unknown internal structure has been used for holographic imaging.[111,112] Its scattering matrix is first calibrated and then correlated with the speckle intensity pattern of an unknown signal passing through the diffusive layer. Finally, the full field of the signal is recovered from the correlation. This technique enables high-resolution holographic imaging with a long working distance beyond what a conventional objective lens can achieve.[113]

An alternative way of wavefront sensing using a thin diffuser is to place it in the close vicinity of a camera.[114] The diffuser produces a speckle pattern that is recorded by the camera. Due to the angular memory effect, the speckle grains in the camera are translated with the incident wavefront tilt. The local wavefront gradient can be determined from the local translation of the speckle pattern. The translation vector map is computed with a fast diffeomorphic image registration algorithm and then integrated to reconstruct the entire wavefront. While a change of the wavefront is efficiently converted to a change in the speckle pattern, the exact intensity distribution depends on the

unknown structure of the scattering layer. Nevertheless, the correlation between two incident wavefronts is directly related to the correlation between their speckle patterns produced by the scattering layer, independent of the scattering structure of the layer.[115] This universal relation facilitates wavefront sensing with arbitrary diffusers.

## F. Light focusing and fluorescence microscopy

Another imaging modality is focusing the probe beam by a lens to an object and collecting the response signal while scanning the focal spot across the object. This can also be done with a random lens, but requires a spatial light modulator (SLM) to pre-compensate the wavefront distortion of the probe beam by scattering.[116,117] As shown in Fig. 11, a smaller focal spot is obtained when inserting a multiple-scattering slab between a conventional lens and a camera, as the large-angle scattering effectively increases the numerical aperture.[75] To further reduce the focal spot size, an annular mask is placed after the random lens to filter low spatial frequency components in the transmitted field.[118] Also, a random lens is constructed with high refractive-index material to focus down to sub-100 nm.[119] In addition to focusing in the far-field, near-field focusing is possible with a lens made of disordered nanoparticles.[120]

Thanks to the angular memory effect, once the incident wavefront for focusing to a particular position is found, the focal spot can be scanned laterally by tilting the wavefront. Similar to correlation-based imaging, there is a trade-off between the scanning range (field of scan) and the spatial resolution (size of focus). It is possible to overcome this trade-off, that is, to reach beyond the memory effect range, by calibrating the field transfer function of the random lens, which provides the incident wavefront for focusing to any point or even multiple points.[121] Even if only a subset of the matrix is measured, a
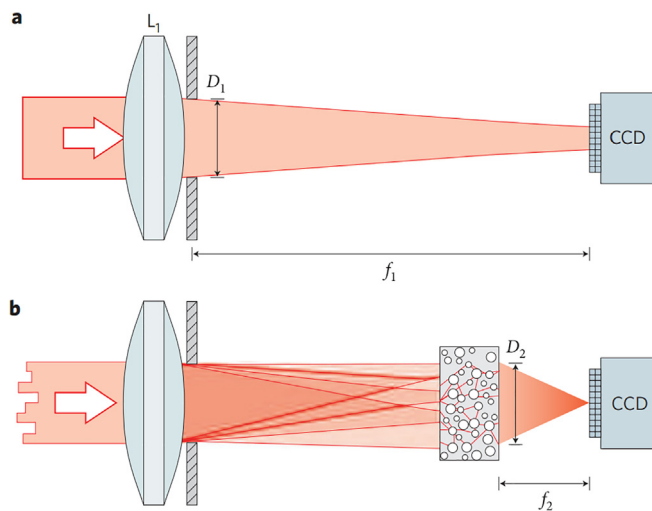


**FIG. 11.** Disorder improves light focusing. Reprinted with permission from Vellekoop *et al.*, Nat. Photonics **4**, 320 (2010). Copyright 2010 Nature Publishing Group. (a) A conventional lens $L_1$ with focal distance $f_1$ focuses light onto a camera. An iris controls the aperture $D_1$ of the lens. The focus is as sharp as the diffraction limit of the lens. (b) A disordered sample at distance $f_2$ from the camera randomly scatters the light. After shaping the incident wavefront with a spatial light modulator (not shown), the light focuses through the scattering sample to a spot that is smaller than that in (a). $D_2$ is the diameter of the diffuse spot at the back of the sample.

technique called sparse field focusing allows arbitrary scanning of the focus, but with lower contrast.[122]

Typically, a bulk random lens has a statistically isotropic structure. Recently, the random lens with anisotropic scattering structure is fabricated and used in combination with a SLM to focus light to submicrometer-thin sheets.[123] Furthermore, a disorder-engineered metasurface is designed and fabricated. Thanks to its extremely broad scattering range, light can be focused to $10^8$ points.[124]

In addition to the structural design of random lens, the point spread function (PSF) can be engineered by numerical processing of the transfer function. For example, by numerically applying a Fourier filter to the transmission matrix of a random lens, the 3D profile of its focus is shaped at will.[125] Bessel, donut, and helical beams are generated, as well as foci smaller than the diffraction-limited speckle size.

Disordered metallic nanostructures have been utilized to construct plasmonic lens for near-field focusing with far-field control.[126] By coupling the wavefront-shaped far-field optical waves ($\lambda = 637$ nm) to a 2D random array of holes in a thin gold film, surface plasmon polaritons can be focused to arbitrary positions with a spot size of 170 nm. Hence, the plasmonic random lens may be applied to near-field focusing and scanning microscopy with sub-wavelength resolution.[127]

One issue of focusing waves with a random lens is the non-zero background outside the focus. Although the intensity at the focus can be much higher than the average intensity of the background, the energy inside the focus is still much lower than the total energy outside. Another issue of using the random lens is that a SLM is needed to shape the incident wavefront of a coherent beam for focusing. To overcome these issues, a technique has been invented for fluorescence imaging through a scattering medium without a SLM.[100] An unknown speckle pattern generated by a laser beam propagating through a random medium illuminates a thin sample, and the fluorescence signal produced by the speckled illumination is measured by a bucket detector. Then, the illuminating speckle pattern is raster-scanned across the sample by tilting the incident laser beam onto the random medium. From the fluorescence signals recorded for a range of angles within the memory effect range, a 2D image of the sample is reconstructed. This technique is adopted for fluorescence imaging with a high-index random lens to enhance the spatial resolution to 116 nm.[128] To image beyond the range of angular memory effect, additional low-resolution fluorescence images are taken for reconstruction of a wide field of view.

## G. Multimode fiber endoscopy

Although a bundle of single-mode optical fibers has been widely employed for endoscopic imaging, it is advantageous to use a multimode fiber (MMF),[129–132] because its larger NA gives better resolution and its smaller cross section means less invasive. The higher areal density of optical guided modes in a MMF enhances the information capacity. However, the fiber modes have different propagation constants and acquire varying phase delays, and thus, spatial images transmitted through a MMF will be distorted. Moreover, random coupling of guided modes, caused by fiber imperfections and external perturbations, further scramble the information, similar to the process of light scattering in a disordered material. Hence, a MMF with uncontrolled mode coupling resembles a random lens. Its transfer function maps the input fields in all fiber modes to the output field distribution in an

object plane.[133–135] After calibration of the transfer function, the field patterns at the fiber distal end can be recovered from the signals transmitted back to the proximal end.[136–139] Machine learning and compressive sensing techniques have been used for image classification and reconstruction through MMFs, which are robust against environmental changes and wavelength drift.[140–157]

Similar to random scattering medium, it is possible to focus light or create arbitrary spatial pattern at the fiber output by shaping the input wavefront of a laser beam.[133,158–166] In short fibers with weak mode coupling, rotational and quasi-radial memory effects allow transverse scanning of a focal spot.[167–169] If light propagates through a MMF with a specific propagation constant, a quadratic radial phase modulation of the input wavefront will cause an axial shift of the output pattern.[136] More recently, the translational memory effect is observed in MMFs with a square cross section.[170] However, none of these memory effects will survive in long MMFs with strong mode coupling. To increase the spatial resolution of 3D imaging and optical manipulation, photonic crystal fibers with numerical aperture significantly higher than that of conventional fibers are used.[171,172] Alternatively, a highly scattering material is added to the distal end of a MMF to enable the formation of smaller foci at longer distances from the fiber tip.[173] Instead of shaping the input wavefront, the transfer function of a MMF can be modulated by applying computer-controlled mechanical perturbations to the fiber to obtain desired output patterns.[174]

Using a minimally invasive MMF, subcellular spatial resolution has been achieved for deep-brain *in vivo* imaging.[175,176] Optical sectioning and enhanced resolution are demonstrated with saturated excitation and temporal modulation.[177] Compared to one-photon excitation, two-photon excitation through a MMF improves depth sectioning for 3D fluorescence imaging.[178] To enhance the image contrast, digital confocal microscopy through a MMF is realized by digitally engineering the excitation wavefront and then applying a virtual digital pinhole on the collected signal.[179] To acquire chemical contrast for diagnosis, nonlinear microscopy based on coherent anti-Stokes Raman scattering (CARS) is developed with a MMF endoscope.[180] Hybrid photoacoustic-fluorescence microendoscopy through a MMF is shown to provide both anatomical and functional contrasts.[181] Beyond the imaging applications, 3D printing at the distal end of a MMF is demonstrated by wavefront shaping of input laser pulses.[182]

While conventional optical fibers are mostly used for convenience, disordered fibers are fabricated and exploited for endoscopic imaging[183–187] and information transmission.[188] The refractive index fluctuates randomly over the fiber cross section, but remains uniform along the fiber.[189] Transverse scattering and interference results in transverse localization of light, similar to Anderson localization in a 2D disordered structure. Such fibers can transport transversely localized beams with low crosstalk.[190] It has been shown that the transported images have less pixelation and higher contrast than those through the multicore fibers.[183,184]

## IV. SPECKLE-BASED SPECTROMETERS

In this section, optical speckles, generated by random scattering structures or multimode fibers, are utilized to build compact spectrometers with record-breaking resolution. After introducing relevant parameters for spectrometers (Sec. IV A), we describe three

mechanisms underlying speckle spectrometers and wavemeters: random optical diffraction (Sec. IV B), multiple light scattering (Sec. IV C), and multimode waveguide/fiber dispersion (Sec. IV D). Finally, we will discuss the pros and cons of computational spectrometers based on speckle and disorder (Sec. IV E).

### A. Spectrometer parameters

Optical spectrometers are widely used in scientific and industrial research. The performance of a spectrometer is characterized by multiple parameters. The spectral resolution $\delta\lambda$ denotes the smallest difference in wavelength $\lambda$ that can be distinguished. The resolving power is the ratio of wavelength $\lambda$ and resolution $\delta\lambda$. The finesse is given by the number of spectral channels $N_\lambda$ that can be covered in one measurement. Each spectral channel has a width of $\delta\lambda$. If these channels are contiguous in wavelength, the wavelength range covered in one acquisition equals to $N_\lambda \Delta\lambda$. The free spectral range (FSR) denotes the minimal spacing of (well-separated) wavelengths at which a spectrometer produces identical response, and limits the spectral bandwidth of a spectrometer.

The sensitivity of a spectrometer depends on the photon throughput, that is, the percentage of photons entering the spectrometer eventually reaching the sensors. How weak a signal that a spectrometer can measure depends not only on the signal strength but also on the amount of detection noise, ultimately the signal-to-noise ratio (SNR). The signal strength increases with collection efficiency, which is related to the number of spatial modes a spectrometer can harvest while maintaining the spectral resolution. For many applications, the operation speed matters, and it determines the number of spectra that can be measured or reconstructed in a second. Finally, size, weight, power, and cost (SWaP-C) are also relevant parameters for practical applications.

Most spectrometers face tradeoffs between some of aforementioned parameters. For example, a grating spectrometer diffracts light of different wavelengths to different directions. Two closeby wavelengths, which have slightly different diffraction angles, can only be spatially separated and measured by different detectors after propagating over a long distance $L$ from the grating to the detector. The spectral resolution $\delta\lambda$ scales as $1/L$, so a smaller spectrometer has lower resolution. The trade-off between resolution and size limits the performance of chip-scale spectrometers—a key element for low-cost, portable sensing and lab-on-a-chip applications, hence prompting exploration of alternative mechanisms for spectrometer operation. As will be shown below, incorporating disorder into spectrometers not only overcomes the trade-off between size and resolution, but also removes other limitation like the free spectral range.

### B. Random optical diffraction

With randomized width or depth of groves, a disordered grating, also called a random polychromat,[191] diffracts light of one wavelength to many directions [Fig. 12]. The one-to-many spectral-to-spatial mapping is characterized by a point spread function, $P(x;\lambda)$, which describes the spatial intensity distribution of diffracted light at wavelength $\lambda$. Because waves of different $\lambda$ do not interfere in the time-integrated measurement, their intensities add at each sensor. The intensity distribution over a sensor array $I_{\text{dif}}(x)$ is related to the spectral density of an input signal $I_{\text{sig}}(\lambda)$ by $P(x;\lambda)$,
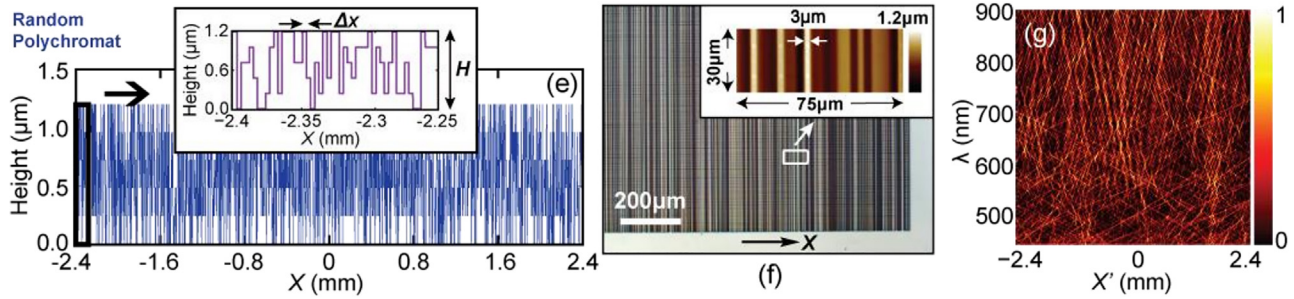
**FIG. 12.** Random polychromat (disordered grating) for spectrum reconstruction. Reprinted with permission from Wang *et al.*, Opt. Express **22**, 14575 (2014). Copyright 2014 The Optical Society. Left panel: Depth profile showing random fluctuation of groove depth of a grating. Inset is magnified view of a segment enclosed by the black box. Middle panel: Optical micrograph of a corner of the fabricated random polychromat. Inset shows atomic-force microscope measurement of a small region delimited by the white box. Right panel: Spatial-spectral PSF $P(x; \lambda)$ measured at a distance of 450 mm from the random polychromat. The spectral resolution is 1 nm.

$$I_{\mathrm{dif}}(x) = \int P(x; \lambda) \, I_{\mathrm{sig}}(\lambda) \, d\lambda. \qquad (8)$$

Once $P(x; \lambda)$ is calibrated by recording the diffraction patterns at individual wavelengths using a tunable source, any unknown spectrum $I_{\mathrm{sig}}(\lambda)$ can be recovered from the measured diffraction pattern $I_{\mathrm{dif}}(x)$.[191,192] However, the spatial profile and polarization state of a signal incident onto the random polychromat must be identical to those adopted in the PSF calibration. Also, the distance $L$ from the random polychromat to the sensor array is fixed.

The spectral resolution is determined by how small a wavelength shift will cause a notable change in the diffraction pattern. Such a change is quantified by spectral correlation of the PSF:

$$C_S(\Delta\lambda) \equiv \frac{\langle P(x, \lambda) \, P(x; \lambda + \Delta\lambda) \rangle_{x,\lambda}}{\langle P(x; \lambda) \rangle_{x,\lambda} \, \langle P(x; \lambda + \Delta\lambda) \rangle_{x,\lambda}} - 1, \qquad (9)$$

where $\langle \cdots \rangle_{x,\lambda}$ denotes an average over spatial position $x$ and wavelength $\lambda$. As $\Delta\lambda$ increases, $C_S(\Delta\lambda)$ gradually decays to zero. The half-width-at-half-maximum (HWHM) provides an order-of-magnitude estimate of wavelength resolution $\delta\lambda$. Similar to a grating spectrometer, the resolution is inversely proportional to the distance $L$: $\delta\lambda \propto 1/L$, and a larger polychromat with finer grooves provides a better resolution.[191,192]

The number of spectral channels $N_\lambda$ that can be recovered in a single measurement is determined by the number of independent spatial channels $N_x$ over a sensor array. Without prior information of the signal spectrum, $N_\lambda \simeq N_x$, but if there is prior information or the spectrum is sparse, $N_\lambda \gg N_x$ is possible using compressive sensing algorithms. One advantage of the random polychromat is that the spectral channels in one measurement do not need to be contiguous in wavelength. If it is known *a priori* that the signals are located in certain wavelength regions that are disconnected, the finite number of spectral channels will be allocated only to those regions. In this way, a small number of spectral channels can effectively cover a broad wavelength range.

Switching from one-dimensional (1D) to two-dimensional (2D) diffraction further increases $N_\lambda$. For example, the PSF $P(x; y; \lambda)$ is generated by a 2D array of air holes with varying diameter[193,194] or a frosted glass with rough surface.[195] The mapping from 1D spectrum to 2D space greatly enhances the number of spatial channels $N_{x,y}$, which is given by the number of speckle grains within the 2D sensor array. A tiny wavelength shift has been detected from the speckle displacement, and a resolving power of one million for a single wavelength is demonstrated.[196]

The multiplex spatial-to-spectral mapping offered by a random polychromat is ideally suited for compressive spectroscopy. This scheme is equivalent to parallel projection of an input spectrum to multiple sensors. The one-to-many spectral-to-spatial mapping allows a small sensor array to capture light of all wavelengths without rotating the random polychromat. However, such mapping raises concerns about the SNR, because even monochromatic light spreads over many sensors, while a grating diffracts the light to a single sensor. If the signal is weak or the sensor noise is large (e.g., at the infrared wavelength), dividing the signal over many sensors is detrimental to spectrum reconstruction.[197] However, if the signal shot noise dominates over the sensor dark noise, the spectrum reconstructed from a random diffraction pattern has comparable quality to that measured by grating diffraction. Quantitatively, how the noise propagates through the nonlinear optimization process to manifest as an error of spectrum reconstruction is difficult to analyze.[197] In addition, various denoising algorithms have been developed over the years, and recent adoption of machine learning techniques significantly improves the robustness of spectrum reconstruction against measurement noise and system drift.[198]

## C. Multiple light scattering

Compared to optical diffraction from a random polychromat or single scattering by a weakly disordered material, multiple scattering in a highly disordered slab accelerates speckle decorrelation and enhances spectral resolution.[3] For any dispersive medium, the spectral resolution is inversely proportional to the temporal spread of light, which is given by the optical path length difference at a single wavelength. For light diffusion in a 2D system, the optical path length distribution has a width $\Delta\mathscr{L}$ proportional to the average path length, which scales as $L^2/l_t$, where $L$ is the linear dimension of the system, and $l_t$ is the transport mean free path. The spectral resolution[199] is inversely proportional to the path length difference $\Delta\mathscr{L}$, which leads to the scaling $\delta\lambda \propto l_t/L^2$. Compared to the $1/L$ scaling of $\delta\lambda$ for optical diffraction and single scattering, the $1/L^2$ scaling for multiple scattering and light diffusion enables a much faster increase in resolution

with $L$. For the same value of $L$, the spectral resolution is enhanced by a factor of $L/l_t$, which can be much larger than 1.

However, optical diffusion reduces the transmission, as most light is reflected after multiple scattering. In the absence of dissipation, the total transmission scales as $l_t/L$. While the spectral resolution is enhanced by $L/l_t$, the photon throughput is reduced by the same factor. The trade-off between resolution and sensitivity has been addressed in the design of an on-chip spectrometer.[199] As shown in Fig. 13, a random array of air holes (150 nm in diameter) etched to a silicon layer is confined in a semicircle and surrounded by a highly reflecting photonic crystal boundary (periodic lattice of air holes), so that the diffusive photons are effectively channeled from an input waveguide at the base of the semicircle to the output waveguides at the circumference. While the spectral resolution is enhanced via multiple scattering of light by air holes, the throughput remains high due to suppression of reflection with the closed boundary. Although the semicircle radius is merely 25 $\mu$m, it is much larger than the transport mean free path, resulting in sub-nanometer resolution at 1500 nm wavelength.[199] To avoid material absorption, silicon is replaced by silicon nitride for broadband operation at visible and near-infrared wavelengths.[200,201] Single-photon detectors and an efficient broadband fiber-to-chip coupler are integrated with the disordered structure in a single chip.[202] The power sensitivity of –111.5 dBm is reached in the telecom band.

In addition to small footprint, another appealing feature for on-chip implementation is that the random spectrometer can operate over a broad wavelength range without structural modification. Regardless of input light wavelength, scattered waves always reach the sensors. The photonic–crystal boundary cannot be highly reflective at any wavelength, but it may be replaced by a random array of densely packed air holes. By adjusting the hole size and density as well as the boundary layer thickness, it is possible to reach 2D light localization, resulting in broadband reflection. In contrast to grating spectrometers, the random spectrometers do not suffer the redundancy that sets the free spectral range (FSR), because a disordered structure is free of any symmetry or degeneracy. The speckle pattern is formed by interference of numerous scattered waves going through different paths and having uncorrelated phases. The probability of having identical speckle patterns at far apart wavelengths is negligibly small, especially when the number of speckle grains is large.

One issue of the planar disordered structure is that a small amount of light is scattered out of the plane. Such loss decreases photon throughput and spectral resolution. The out-of-plane leakage is stronger for longer scattering paths, thereby preferentially attenuating
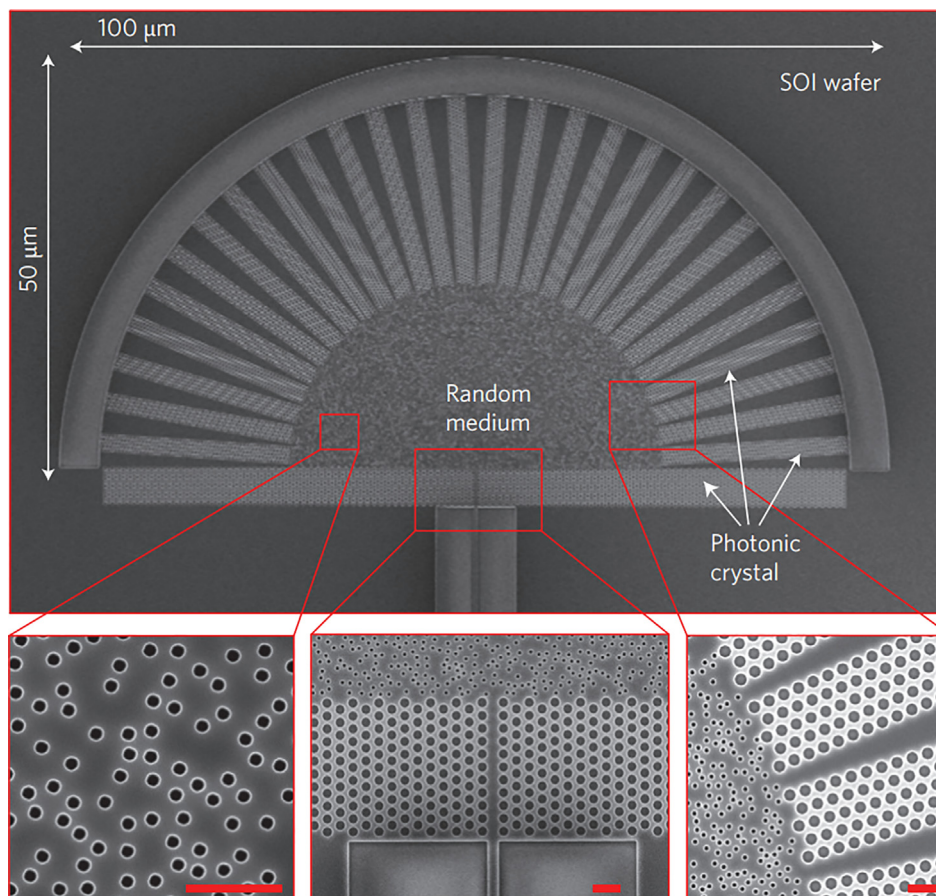


**FIG. 13.** Chip-scale diffusive spectrometer. Reprinted with permission from Redding *et al.,* Nat. Photonics **7**, 746 (2013). Copyright 2013 Nature Publishing Group. Scanning electron microscope image of a semicircular array of randomly positioned air holes in a silicon-on-insulator (SOI) wafer, surrounded by highly reflective photonic-crystal layer. The signal is launched into the random structure via a defect waveguide at the bottom of the semicircle. The light then diffuses through the random array via multiple scattering and eventually reaches the 25 defect waveguides around the circumference of the semicircle. These tapered waveguides couple the signals to photodetectors at their ends (not integrated). The distribution of intensities over the detectors is used to identify the input spectrum. The insets in the bottom row are magnified images, and the scale bars indicate 1 $\mu$m.

the light going through longer paths. The path length distribution is narrower, and the spectral resolution is lower. One way of reducing the out-of-plane scattering is engineering the spatial Fourier spectrum of a 2D scattering structure.[199] By introducing either short-range order or long-range order, it is possible to attenuate the spatial frequencies of the structure that facilitate out-of-plane scattering of light. Inverse design of the scattering structure can maximize the amount of light reaching the output waveguides at desired wavelengths.[203] In another scheme, a thin layer of random alumina particles is inserted in between two mirrors to reduce light leakage.[204] Principal component analysis (PCA) is applied to determine the wavelength corresponding to a speckle pattern with picometer resolution.

Integrating spheres with rough inner walls have been used for high-resolution wavelength meters (wavemeters). Light is bounced many times inside an integrating sphere, and the escaping waves interfere to form a speckle pattern at the output port. From the speckle pattern, the corresponding wavelength is identified.[205] The wavemeter operates in the visible and near-infrared spectrum with sub-femtometer wavelength resolution. It has been exploited for laser frequency locking to an arbitrary wavelength.[205] The maximum lock update rate of 200 Hz is limited by the time it takes to identify the wavelength using PCA. By resorting to a Poincaré descriptor of the speckle pattern, the computation time is shortened by two orders of magnitude, enabling kHz-rate measurements of femtometer-level wavelength changes.[206] More recently, deep learning is employed to reject instrumental and environmental noise, providing attometer-scale wavelength precision over a range of 488 nm to 976 nm.[207] In addition to recording speckle intensity, single-shot speckle phase detection is exploited for wavelength identification with high precision.[208]

## D. Multimode waveguide dispersion

A speckle pattern is also generated by a multimode fiber (MMF) through interference of light in guided modes. The transmitted field distribution at the exit face of a MMF is

$$E_{\text{MMF}}(\rho, \phi; \lambda) = \sum_{m=1}^{M_w} a_m \Psi(\rho, \phi; \lambda) e^{-i\beta_m(\lambda) L_w}, \qquad (10)$$

where $\rho$ and $\phi$ are polar coordinates, $L_w$ is the fiber length, $M_w$ is the total number of guided modes, $a_m$ is the complex amplitude of the $m$-th mode whose spatial field profile $\Psi$ and propagation constant $\beta_m$ change with wavelength $\lambda$. Once the spatial wavefront and polarization state of incident light are fixed, the transmitted speckle intensity pattern, $I_{\text{MMF}}(\rho, \phi; \lambda) = |E_{\text{MMF}}(\rho, \phi; \lambda)|^2$, is unique for each wavelength
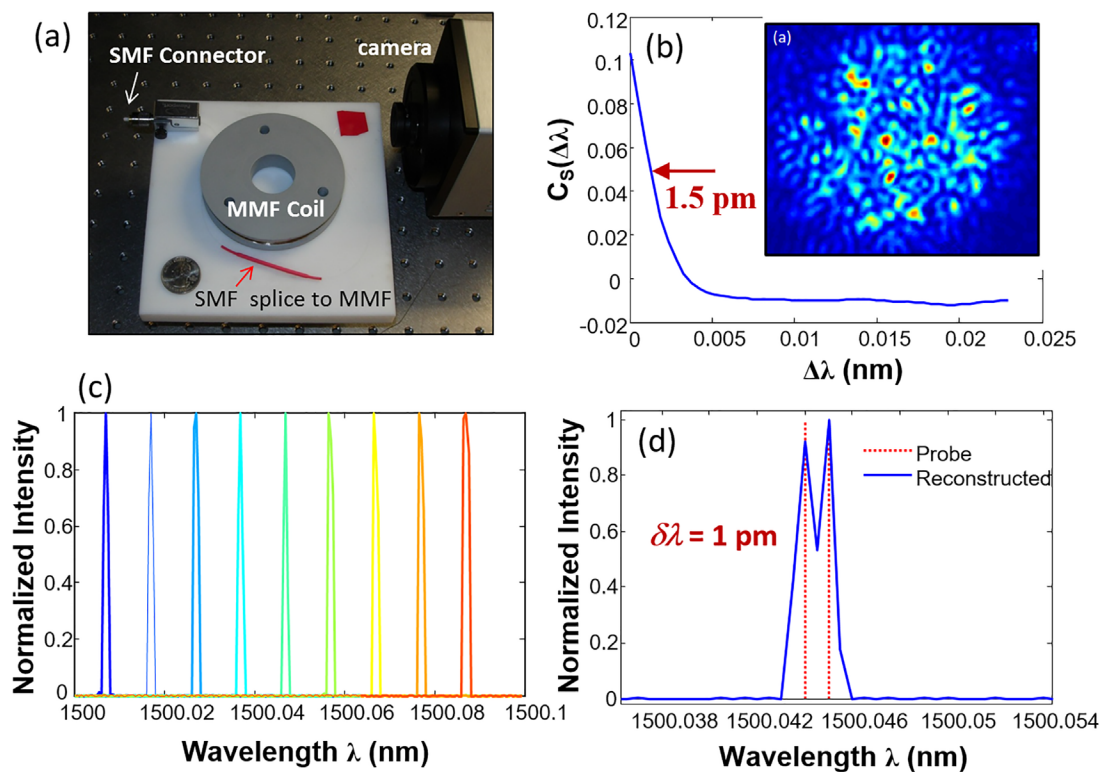


FIG. 14. Multimode fiber spectrometer with ultrahigh resolution. Reprinted with permission from Redding *et al.*, Optica **1**, 3 (2014). Copyright 2014 The Optical Society. (a) Photograph of a multimode fiber (MMF) spectrometer. Light is coupled via a polarization-maintaining single-mode fiber (SMF) to the 100-m-long MMF (coiled to a 3 in. spool), and the transmitted speckle pattern is recorded by a monochrome camera. (b) Spectral correlation function of the speckle pattern $C_S(\Delta\lambda)$ features a half-width-at-half-maximum (HWHM) of 1.5 pm. Inset: Speckle intensity pattern measured at $\lambda = 1500$ nm. (c) Spectral lines reconstructed from speckle patterns. (d) Reconstructed spectrum (blue line) of two narrow lines separated by 1 pm. The red dotted vertical lines mark the probe wavelengths.

and serves as a fingerprint. The spectral contrast decreases as the number of spectral components increases, because their speckle patterns add incoherently. Previously, the laser linewidth has been retrieved from the speckle contrast.[209] Recently, it is shown that the entire spectrum $I_{\mathrm{sig}}(\lambda)$ can be reconstructed from a speckle pattern

$$I_{\mathrm{MMF}}(\rho, \phi; \lambda) = \int P(\rho, \phi; \lambda) \, I_{\mathrm{sig}}(\lambda) \, d\lambda, \qquad (11)$$

once the PSF $P(\rho, \phi; \lambda)$ is calibrated.[210]

The spectral resolution is dictated by modal dispersion that temporally stretches light through a MMF. Assuming all fiber modes are excited with equal magnitude and their coupling is negligible, the resolution is inversely proportional to the path length difference

$$\delta\lambda \propto \frac{1}{(\dot{\beta}_1 - \dot{\beta}_M) L}, \qquad (12)$$

where $\dot{\beta}_1 - \dot{\beta}_M = d\beta_1/d\lambda - d\beta_M/d\lambda$ reflects the maximal difference of group delay, and it scales as $\mathrm{NA}^2$ for a step-index fiber of NA $\ll 1$.[211] If mode coupling is strong in a MMF, random hopping of photons among the fiber modes can be described by diffusion in the mode basis, and the path length difference is proportional to $\sqrt{L}$, so $\delta\lambda \propto 1/\sqrt{L}$.

Since the optical fiber has been optimized for long-distance transmission with minimal loss, a long MMF can be used to reach ultrahigh resolution without sacrificing throughput. The resolving power $\lambda/\Delta\lambda$ exceeds $10^6$ for a 100-meter-long step-index MMF (core diameter $D_w = 105\,\mu m$, NA $= 0.22$) at $\lambda = 1500$ nm.[212] Such a long fiber is coiled on a small spool, making the spectrometer (comprised of a single MMF and a monochrome camera) compact and lightweight (Fig. 14).

The MMF is also shown to function as an ultrahigh-resolution wavemeter that can precisely determine a single wavelength.[213] By modulating the input signal with an acoustic optical modulator (AOM) and applying the PCA, attometer resolution at $\lambda \simeq 780$ nm is obtained with a 18-cm-long step-index MMF ($D_w = 105\,\mu m$, NA $= 0.22$). Multiple wavelengths may be resolved simultaneously by modulating them at different acoustic frequencies.[214]

Since the MMF maps 1D spectrum to 2D space, a large number of spectral channels are measured in a single acquisition. As an example, a 4-cm-long MMF (core diameter $= 105\,\mu m$, NA $= 0.22$) covers the entire visible spectrum with 1 nm wavelength resolution in one measurement.[212] While the fiber core diameter $D_w$ has little influence on spectral resolution, it determines the total number of guided modes $M_w \propto D_w^2$, which sets the upper bound for the number of spectral channels $N_\lambda$. Although a large-core MMF provides a high $N_\lambda$, the speckle contrast $C_t \simeq 1/\sqrt{N_\lambda}$ is low for a dense spectrum of $N_\lambda \gg 1$. Once the contrast is below the noise level, an accurate spectrum recovery is impossible.[197]

To overcome the trade-off between bandwidth and resolution, a wavelength division multiplexer (WDM) is integrated with a bundle of MMFs.[215] The WDM divides a broad spectrum to multiple windows, and each window is covered by a single MMF. The output speckle patterns from all MMFs are recorded simultaneously by a large-area camera (with a large number of pixels). Then, they are separately processed in parallel, greatly reducing the complexity of post-processing and enhancing the speed of spectrum reconstruction. Using five 2-meter-long MMFs, dense spectra centered at $\lambda = 1500$ nm

with 100 nm bandwidth are recovered with 0.03 nm resolution in snapshot measurements.

Compared to other high-resolution spectroscopy tools such as the scanning Fabry–Pérot etalon or the virtually imaged phase array (VIPA), a notable advantage of the MMF is that its spectral range is not limited by the FSR. This is because fiber fabrication imperfections (random refractive index variation) and external perturbations (fiber bending, twisting) make the probability of a highly multimode fiber producing identical speckle patterns at distinct wavelengths extremely low. A MMF spectrometer, combined with an optical frequency comb source, has been adopted in broadband metrology-grade spectroscopy to resolve individual comb lines.[216] The wavelength resolution obtained with a 100-m-long MMF is an order of magnitude higher than that of existing dual-comb spectroscopy. Using the MMF spectrometer, 500 comb lines are measured simultaneously and 3500 lines sequentially for direct comb spectroscopy.

The resolving power of a MMF spectrometer can be further improved by increasing the fiber length and/or the differential group delay. However, the speckle patterns are sensitive to environmental changes including mechanical vibration and temperature drift. Recent studies show that a combination of thermal and mechanical stabilization with software correction can enable robust performance of a high-resolution MMF spectrometer.[212,216] Alternately, the spectral-to-spatial PSF $P(\rho, \phi; \lambda)$ may be calibrated as a function of temperature, and the one matched to the current temperature will be used for spectrum recovery.

Further stabilization is realized with on-chip implementation of the MMF spectrometer. As shown in Fig. 15(a), a silicon multimode waveguide (width $= 10\,\mu m$, length $= 18$ mm) is coiled in an Archimedean spiral (outer radius 250 $\mu m$).[217] By introducing evanescent coupling of light between adjacent waveguide arms (separated by small air gap), photons will leap forward or backward in time, greatly increasing the temporal spread. Consequently, the spectral resolution is dramatically enhanced [Fig. 15(b)], and such enhancement is non-resonant and broadband. The coupling of waveguide modes, which is detrimental to a MMF spectrometer, improves the resolution by enhancing the evanescent coupling of lower-order modes in adjacent waveguide arms indirectly (converting to higher-order modes with stronger evanescent coupling and then back). The resolving power exceeds $10^5$ at the $\lambda \simeq 1500$ nm. Like the MMF, the spiral waveguide effectively disperses light at any wavelength as long as the material absorption is negligible and the waveguide remains multimode. Despite the spatial domain is reduced to 1D, a small number of sensors can cover many more spectral channels, if the spectrum is sparse in some domain.[217] Compressive sensing algorithms are adopted for rapid and accurate reconstruction of various types of sparse spectra [one example given in Fig. 15(c)].

Since the output speckle pattern varies with the launch condition of input light, it is crucial to ensure the consistency between the launch used in PSF calibration and that in spectrum measurement. This is done by coupling signals via a single-mode, polarization-maintaining fiber/waveguide to the multimode fiber/waveguide. To recover a large number of spectral channels $N_\lambda$, it is important to excite as many modes as possible at the input. This is realized by using a fiber mode scrambler[218] or off-set fusion of fibers.[219]

The input launch condition may be switched among multiple choices to increase the number of spectral channels $N_\lambda$. On-chip
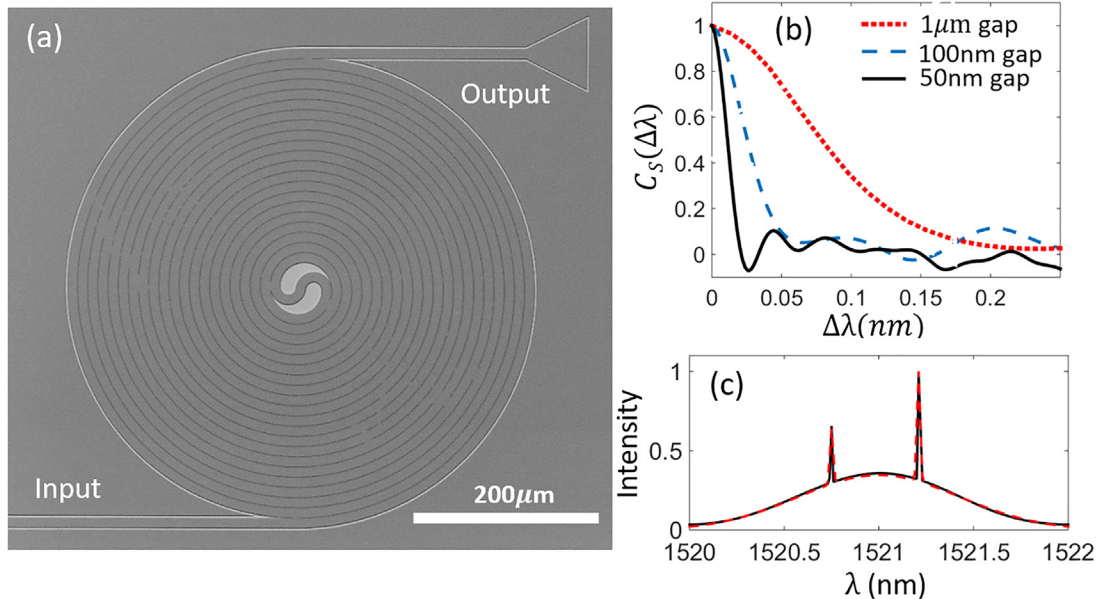
**FIG. 15.** Spiral waveguide spectrometer in a silicon chip. Reprinted with permission from Redding *et al.*, Optica **3**, 956 (2016). Copyright 2016 The Optical Society. (a) A multimode waveguide of width 10 $\mu$m and length 18 mm is coiled into an interleaved Archimedean spiral structure. (b) Spectral correlation function $C_S(\Delta\lambda)$ measured for three spiral structures with different width of air gaps in between adjacent arms. Narrower air gaps results in stronger evanescent coupling between spiral arms, thus spectral correlation width is smaller and wavelength resolution is better. (c) A reconstructed spectrum has two sharp lines of different amplitude on top of a broad smooth band.

launchers are implemented to vary relative phases and amplitudes of $M_w$ excited modes.[220] With $M_w$ distinct launch conditions, $N_\lambda$ is increased from $M_w$ to approximately $M_w^2$. The space-division multiplexing scheme is also implemented with a multicore fiber[221] or an on-chip photonic lantern.[222]

**E. Computational spectrometers**

The speckle-based spectrometers discussed in Subsections IV A–IV D belong to a general class of computational spectrometers. In addition to spatial speckles, temporal speckles generated by a single-mode fiber (SMF) via Rayleigh backscattering are exploited for a high-precision, broad-range wavemeter.[223,224] Speckles are also utilized to enhance spectral resolution and dynamic range of prism spectrometers,[225,226] tapered fiber/waveguide multimode interference spectroscopy,[227–229] and on-chip Fourier-transform spectrometers.[230]

While the speckle spectrometers have fine resolution, broad bandwidth and high throughput, their sensitivity is limited by single-mode collection of signals. Thus, they are most suitable for those applications where single-mode fibers are already used for signal collection, for example, optical wavemeters, telecommunication channel monitors, micro-photoluminescence or micro-Raman spectroscopy, and optical coherence tomography. For volumetric Raman and fluorescence spectroscopy of diffuse sources like tissue and gases, it is essential to use a spectrometer capable of measuring the spectral densities averaged over many spatial modes, in order to improve the SNR. The multimodal spectroscopy is realized with disordered photonic crystals such as 3D opal structures, which can convert spatially incoherent signals with spatially uniform spectral density into spatially non-uniform spectral densities over a detection plane.[231]

An array of spectral filters has also been used for snapshot spectrum measurement. Compared to narrow bandpass filters, broadband random spectral filters provide more efficient and accurate spectrum recovery.[232,233] The random transmission spectra are obtained from binary dielectric layers of varying thickness[234,235] or 2D photonic crystals of different lattice.[236] Since the transmittance of these interference filters is sensitive not only to the input spectrum but also to the angle of incidence, the signals must have a fixed direction of propagation in the spectrum measurement. The spectral filters based on absorption of colloidal quantum dots,[237] which are independent of incident angles, are able to characterize large etendue sources. However, the signal is divided among many filters of different spectra, and the overall throughput is low.

**V. SNAPSHOT HYPERSPECTRAL IMAGERS**

Since a speckle pattern encodes both spatial and spectral information, it can be used for single-shot hyperspectral imaging. This section describes several schemes of utilizing random spatial–spectral coupling to achieve hyperspectral imaging with single acquisition.

Traditional hyperspectral imagers rely on spatial or spectral scanning, which can be slow and generally require moving parts. Snapshot techniques have been developed to capture the full hyperspectral datacube in a single shot. A common method uses tiled superpixels, each comprised of a grid of spectral filters. While the spectral resolution and/or range increases with the number of spectral filters in one superpixel, the size of a superpixel also increases and the spatial resolution decreases. Moreover, the narrow passbands of spectral filters make the overall light transmission low. To improve the throughput and sensitivity, the absorptive color-filter array is replaced by a transparent diffractive-filter array, each filter generating a wavelength-dependent

diffraction pattern in a camera.[238,239] However, the short distance between the filter array and the camera limits the spectral resolution. High spectral accuracy can be obtained by replacing the diffractive filters by 2D photonic crystal slabs,[236] but the field of view is limited by a small number of superpixels.

The spectral filter array has also been replaced by a random scattering film, for example, a semiconductor nanowire mat.[240] A microlens array focuses light to the nanowire mat, which induces multiple scattering and creates an array of speckle patterns. From these patterns, the position-dependent spectra are recovered. The spatial resolution is given by the microlens spacing, and it is ultimately limited by the diffuse spot size of transmitted light, which scales with the film thickness. For example, a strongly scattering GaP nanowire film is thinner than 2 $\mu$m, so the spatial resolution can be potentially high, but the throughput is relatively low. Moreover, the number of speckle grains generated from each focus determines the wavelength range or the number of spectral channels that can be recovered in one measurement.

By resorting to the optical memory effect, multispectral imaging can be realized without a microlens array.[241] A prototype in Fig. 16(a) consists of a diffuser, an iris and a monochrome camera. As described in Sec. III B, the angular memory effect leads to shift-invariant PSF in the far field. When an object $O$ is illuminated by a single wavelength $\lambda$, the far-field speckle intensity pattern is a convolution of the object $O_\lambda$ and the PSF $P_\lambda$, $I_\lambda = O_\lambda * P_\lambda$. The object $O_\lambda$ can be reconstructed by deconvolution of $I_\lambda$ with $P_\lambda$. Under multi-wavelength illumination, the total intensity pattern is a sum of $I_\lambda$:

$$I = \sum_\lambda I_\lambda = \sum_\lambda (O_\lambda * P_\lambda). \tag{13}$$

Due to random scattering and wave interference, the PSF $P_\lambda$ decorrelates with wavelength [Fig. 16(b)]. Assuming the PSFs at all illuminating wavelengths are uncorrelated, the deconvolution of $I$ with $P_\lambda$ is approximately equal to the deconvolution $I_\lambda$ with $P_\lambda$, which gives $O_\lambda$ [Fig. 16(c)],

$$O_\lambda = I_\lambda \circledast P_\lambda \approx I \circledast P_\lambda, \tag{14}$$

where $\circledast$ denotes deconvolution. In essence, each spectral PSF $P_\lambda$ plays the role of a spectral filter in image reconstruction. Note that the single wavelength $\lambda$ can be extended to a spectral band. The single speckle image $I$ of an object $O$ contains both spatial and spectral information, which are multiplexed orthogonally via multispectral PSFs $P_\lambda$. The deconvolution will de-multiplex and recover the spectral image $O_\lambda$ [Fig. 16(d)].

One advantage of using random scattering medium for multispectral imaging is the flexibility in implementation to utilize the full capacity of a 2D camera.[241] Instead of being preset at manufacture, the trade-off between spatial and spectral information is up to the analyzer's choices. On one extreme, the spectral information may be limited to a single wavelength or narrow spectral band, and the maximum spatial information is recovered with a maximal number of spatial pixels and dynamic range. On the other extreme, the spatial information is reduced to a single point object, and the highest spectral resolution of the point source is retrieved. Eventually, the number of spatial points in the object and the number of decorrelated spectral bands
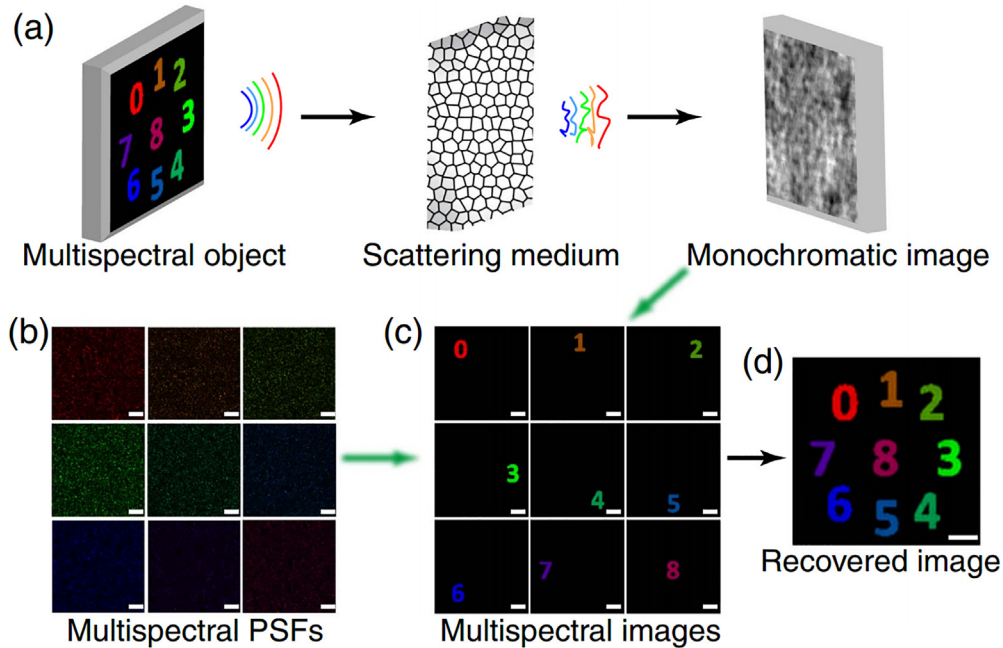


FIG. 16. Speckle-based multispectral imager. Reprinted with permission from Sahoo *et al.*, Optica **4**, 10 (2017). Copyright 2017 The Optical Society. (a) Schematic of multispectral imaging with a scattering medium and a monochrome camera. Light from a multispectral object propagates through the scattering medium and generates a speckle pattern on the camera. (b) Speckle patterns produced by a point object located at center and illuminated with different spectral bands are recorded as spectral PSFs. (c) Reconstructed spectral images from the monochromatic speckle pattern using corresponding spectral PSFs. (d) A full-spectrum image of the object is created by superimposing of individual spectral images. All scale bars denote 20 pixels in numerical simulation.

determine the intensity contrast of the speckle pattern and therefore the recovery quality of the multispectral images. If a hyperspectral object consists of sparse spectral lines spread over a broad spectral range, a large amount of spatial information can be retrieved with high spectral resolution. One potential issue is the crosstalk caused by residual correlation of PSFs at nearby wavelengths.

Another advantage of the speckle-based multispectral imager is its insensitivity to optical (mis)alignment. There are no moving parts and no focusing optics. Due to the memory effect, a small shift in the optical setup causes only a slight shift of reconstructed multispectral images, and thus, there is no need to recalibrate the multi-spectral PSFs.[241] Compressive sensing algorithms have been developed to recover spatial and spectral information from snapshot images taken with a monochrome camera.[242] The quality of recovery is improved by adding a second camera (regular red-green-blue camera) or using additional scattering medium, after splitting the signal.[243,244]

Another design of the lensless hyperspectral imager combines a diffuser and a tiled spectral filter array.[245] The spectral information at one spatial location is distributed over many superpixels, each containing an array of spectral filters. Therefore, each point in the scene is mapped to a unique pseudo-random pattern on the 2D spectral filter array, encoding multiplexed spatio-spectral information. By solving a sparsity-constrained inverse problem, the hyperspectral volume is recovered with sub-superpixel resolution. Since the multiplexing effect of the diffuser allows the recovery of a scene from a subset of sensor pixels, the full spatio-spectral cube can be recovered without the loss in resolution that would result from using a non-multiplexing optic such as a lens. The spectral filters are not necessarily contiguous in wavelength; instead, they can be chosen for specific applications. Selecting narrowband spectral filters will lead to high spectral accuracy and discrimination, but at the cost of low light-throughput. As the signal is distributed over many filters, the SNR is further reduced.

To enhance light throughput and spectral resolution, the scattering medium and spectral filters are replaced by a multicore multimode fiber.[246] As shown in Fig. 17, 3000 fiber cores provide sub-nanometer wavelength resolution over a broad spectral range. In addition to compressive sensing algorithms, deep learning has been employed for fast and reliable reconstruction of both discrete and continuous spectra from speckle patterns.[198] The artificial neural network is trained with the multispectral datasets numerically constructed from the measured spectral PSFs. Compared to analytical inversion methods and compressive sensing algorithms, the deep learning approach is robust to
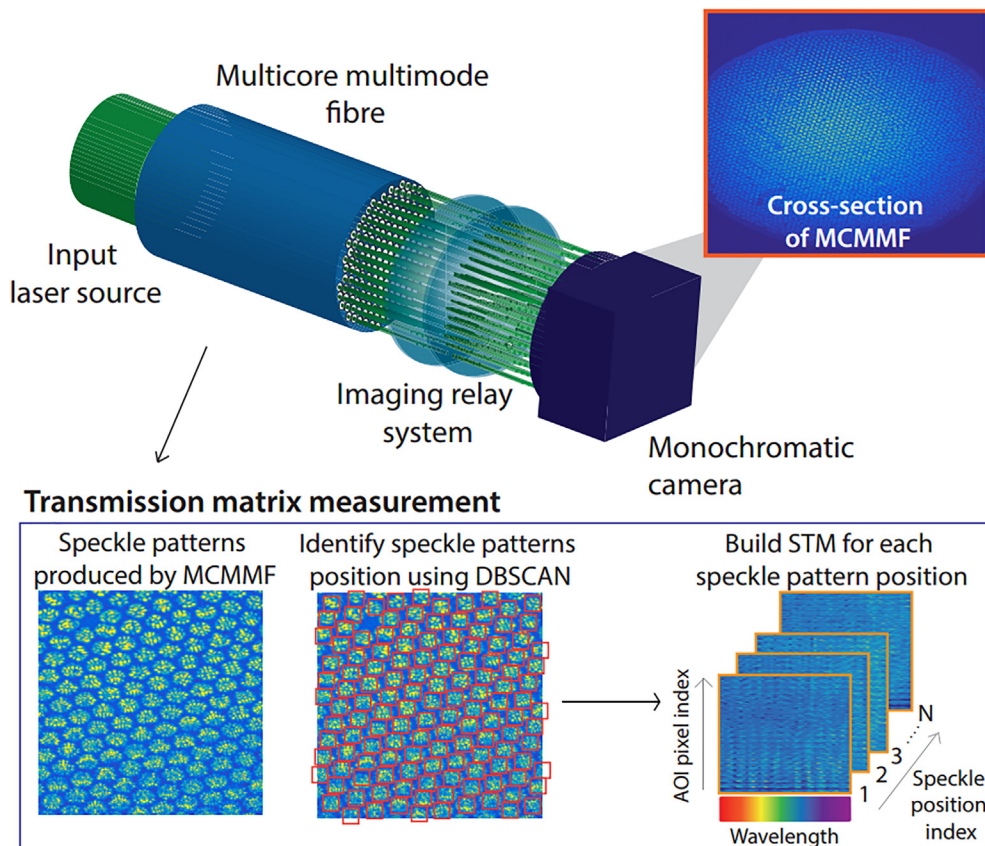


**FIG. 17.** Hyperspectral imaging with multicore multimode fiber. Reprinted with permission from French *et al.*, Opt. Express **26**, 32302 (2018). Copyright 2018 The Optical Society. Light travels through a multicore multimode fiber (MCMMF) and the cross section of the end of the fiber is imaged on to a camera. A clustering algorithm, DBSCAN, detects the coordinates of the speckle patterns produced by each fiber core on the camera. The pattern coordinates are then used to calibrate a spectral intensity transmission matrix (STM) by measuring wavelength-dependent speckle patterns at every core position and storing them in a three-dimensional data cube.

system drift and measurement noise. Although it takes time to train an artificial neural network, once it is done, the reconstruction is fast enough for real-time recovery of hyperspectral information.

# VI. SCATTERING POLARIMETERS

The vectorial nature of light plays an indispensable role in light–matter interaction, optical sensing and imaging applications. In Secs. III–V, the polarization states of signals are fixed. In this section, we describe how the vector components of light can be measured using disordered structures. Since multiple scattering of light in complex media encodes spatial, spectral, and polarization information of input signals to output speckle patterns, it is possible to reconstruct spatially resolved (Sec. VI A) and spectrally resolved (Sec. VI B) polarization states from a single image.

## A. Spatial polarimetry

When light propagates through a 3D disordered structure or a multimode fiber, it is depolarized (Fig. 18). The change of polarization state is deterministic for a specific configuration of the system and is fully captured in the polarization-resolved transfer matrix for coherent light.[247] Without loss of generality, we use the horizontal (H) and vertical (V) linear polarizations as the basis to decompose any coherent polarization state. Equation (3) is generalized to:

$$
\begin{bmatrix} \mathbf{E}_{\text{out}}^H \\ \mathbf{E}_{\text{out}}^V \end{bmatrix} = \begin{bmatrix} \mathbf{M}_{HH} & \mathbf{M}_{HV} \\ \mathbf{M}_{VH} & \mathbf{M}_{VV} \end{bmatrix} \cdot \begin{bmatrix} \mathbf{E}_{\text{in}}^H(\mathbf{r}) \\ \mathbf{E}_{\text{in}}^V(\mathbf{r}) \end{bmatrix}. \tag{15}
$$

$\mathbf{E}_{\text{in}}^H(\mathbf{r})$ and $\mathbf{E}_{\text{in}}^V(\mathbf{r})$ represent horizontal and vertical components of the input field profile, and $\mathbf{E}_{\text{out}}^H(\mathbf{r})$ and $\mathbf{E}_{\text{out}}^V(\mathbf{r})$ of the output. The polarization-resolved transfer matrix contains four submatrices $\mathbf{M}_{HH}$, $\mathbf{M}_{HV}$, $\mathbf{M}_{VH}$, and $\mathbf{M}_{VV}$. $\mathbf{M}_{HV}$ and $\mathbf{M}_{VH}$ account for polarization conversion by optical scattering. Once the full matrix is calibrated, the spatially varying polarization state of an input signal can be recovered from polarization-resolved measurement of the output field profile.[248]

Equation (15) holds for coherent polarization states. A more general description of polarization that is valid for both coherent and incoherent states is the Stokes vector $\mathbf{S}$. It contains four independent parameters $(S_1, S_2, S_3, S_4)$. If the polarization state of a signal beam is spatially invariant, the Stokes vector can be reconstructed from four measurements of spatial intensity correlations of speckle patterns generated by a disordered structure.[249,250] First, four reference speckle patterns, produced by a scattering medium for four known polarization states of the input light, are recorded. For example, the four reference polarization states are three linear polarizations and one right-handed circularly polarization (+). The first three linear polarizations are oriented to the x-axis (0°), the y-axis (90°), and 45°, respectively. The corresponding speckle patterns transmitted through or reflected from a scattering medium are $R_x$, $R_y$, $R_{xy}$, and $R_+$. Then, a signal of unknown polarization but with identical spatial waveform to the reference light generates a speckle pattern $R_s$. It is cross-correlated with four reference speckle patterns $R_i$, where $i = x, y, xy, +$. The normalized cross-correlation coefficients $C_i = \langle R_s | R_i \rangle$ give the Stokes parameters of the signal,

$$
\begin{aligned}
S_1 &= C_x + C_y, \\
S_2 &= C_x - C_y, \\
S_3 &= 2C_{xy} - (C_x + C_y), \\
S_4 &= 2C_+ - (C_x + C_y).
\end{aligned} \tag{16}
$$

Now we consider a signal with spatially varying polarization, namely, the Stokes vector $\mathbf{S}_{\text{in}}$ changes with position $\mathbf{r}$. It has been shown that the output speckle intensity pattern is linearly related to the input Stokes parameters, as long as light scattering is linear.[251] The output intensity pattern $\mathbf{I}_{\text{out}}(\mathbf{r})$ is expressed as

$$
\mathbf{I}_{\text{out}}(\mathbf{r}) = \tilde{\mathbf{M}}_S \cdot \mathbf{S}_{\text{in}}(\mathbf{r}). \tag{17}
$$

$\mathbf{S}_{\text{in}}(\mathbf{r})$ is a vector with $4\,N_{\text{in}}$ elements, describing the polarization states of input light at $N_{\text{in}}$ spatial positions. $\mathbf{I}_{\text{out}}(\mathbf{r})$ is a vector with $N_{\text{out}}$ elements, denoting the output intensities at $N_{\text{out}}$ positions. The transfer matrix $\tilde{\mathbf{M}}_S$ describes a linear mapping from $\mathbf{S}_{\text{in}}(\mathbf{r})$ to $\mathbf{I}_{\text{out}}(\mathbf{r})$. Once $\tilde{\mathbf{M}}_S$ is calibrated or learned, the Stokes parameters can be recovered from the spatial intensity pattern recorded by a camera.

Compared to conventional polarimeters, the scattering polarimeter enables a single-shot measurement of all Stokes parameters. For a signal beam with spatially invariant polarization, $\mathbf{S}_{\text{in}}$ has only four parameters, which can be recovered from the speckle intensities at
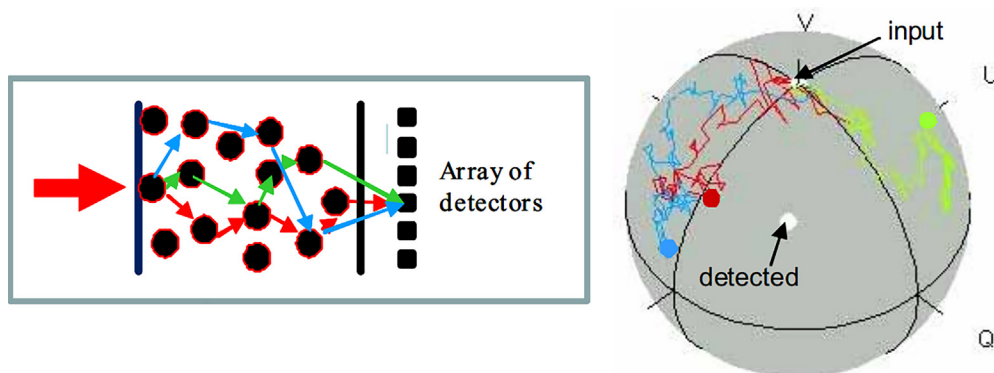


**FIG. 18.** Depolarization by multiple scattering. Reprinted with permission from Kohlgraf-Owens and Dogariu, Opt. Express **16**, 13225 (2008). Copyright 2008 The Optical Society. Light incident onto a disordered system undergoes multiple scattering, which changes its polarization state, as shown by the Poincaré sphere on the right. With a static scattering structure, the deterministic relation between the input and output vector fields allows retrieval of the input polarization state from the output intensity pattern.

four spatial positions. Once the output speckle pattern is recorded in a single shot, the intensities at additional positions may be used to enhance the accuracy of polarization recovery. If the input signals in $N_{in}$ spatial channels have distinct polarization states, a minimum of $N_{out} = 4 N_{in}$ intensities are extracted from the output speckle pattern to determine $N_{in}$ input polarization states.[248] If there is prior information about the signal polarization state or the signal is spatially sparse, the number of output intensities needed for polarization recovery is reduced by using compressive sensing algorithms. This method is also applied to simultaneous measurement of polarization states of multiple laser beams that are mutually incoherent.[251] It has been shown that the polarization rotation of a signal beam can be tracked from the temporal change of the speckle pattern.[249,252]

### B. Spectral polarimetry

Subsection VI A considers monochromatic light. If the input light contains multiple wavelengths, the output speckle pattern encodes spatial, spectral, and polarization information. More specifically, Eq. (17) can be generalized to

$$\mathbf{I}_{out}(\mathbf{r}) = \int \tilde{\mathbf{M}}_S(\lambda) \cdot \mathbf{S}_{in}(\mathbf{r}; \lambda) \, d\lambda. \qquad (18)$$

In principle, the spatially and spectrally resolved Stokes vector $\mathbf{S}_{in}(\mathbf{r}; \lambda)$ can be recovered from a single speckle pattern $\mathbf{I}_{out}(\mathbf{r})$, but the finite number of speckle grains will limit the total amount of information in space, spectrum, and polarization that can be retrieved from one measurement.

If the signal is spatially homogeneous or one spatial mode is probed, only its spectrum and polarization need to be recovered. The polarization state may vary with wavelength; namely, each wavelength has distinct polarization. To recover $\mathbf{S}_{in}(\lambda)$ from $\mathbf{I}_{out}(\mathbf{r})$, the transfer matrix $\tilde{\mathbf{M}}_S(\lambda)$ must be calibrated first. One implementation of the spectral polarimeter is covering one end of an imaging fiber bundle with a thin layer of $0.5 \, \mu m$ silica spheres.[253] Because the spheres are located randomly with respect to the fiber core centers, different cores have widely varying responses, both spectrally and polarimetrically. The other end of the fiber bundle is imaged onto a CCD camera. From the speckle patterns, signals with spectrally varying polarization states are recovered.[253] However, the spectral resolution is modest, because the scattering layer is kept thin to avoid low throughput.

The spectral resolution can be boosted by multiple scattering of light. Let us consider the 2D diffusive structure in the chip-scale spectrometer (Fig. 13). Since the transverse-electric (TE) and transverse-magnetic (TM) waves have slightly different effective indices of refraction in a thin silicon layer, the scattering cross section of a single air hole differs slightly for the two polarizations. Such difference is accumulated by scattering subsequently with multiple holes, leading to distinct intensity patterns at the sensor array. Their orthogonal polarizations result in an intensity sum at each sensor, and thus, the total intensity distribution is given by

$$I_{det}(x) = \int \left[ P_H(x; \lambda) \, I_{sig}^{(H)}(\lambda) + P_V(x; \lambda) \, I_{sig}^{(V)}(\lambda) \right] d\lambda. \qquad (19)$$

From $I_{det}(x)$, the input spectra for TE polarization $I_{sig}^{(H)}(\lambda)$ and TM polarization $I_{sig}^{(V)}(\lambda)$ can be reconstructed, because the spectral PSFs for the two polarizations $P_H(x; \lambda)$ and $P_V(x; \lambda)$ are notably different.

Equation (19) assumes the polarization mixing by in-plane scattering is negligible. If this is not the case, the input TE wave may be converted to a TM wave and interfere with the original TM wave at the same wavelength. Then, the intensity sum must be replaced by a field sum. However, if the input TE and TM waves are mutually incoherent at all wavelengths, the intensity sum will remain valid even in the presence of polarization mixing. Hence, the spectra for two polarizations can still be recovered using Eq. (19).

## VII. TEMPORAL MEASUREMENT

Now we shift to the time domain and show how time-integrated speckle patterns from multimode optical fibers/waveguides are employed to retrieve temporal information at both radio frequency and optical frequency. In Sec. VII A, radio frequency (RF) receivers based on optical speckle detection break the Nyquist sampling limit by employing compressive (compressed) sensing techniques. Section VII B presents two schemes for single-shot full-field recovery of ultrashort optical pulses, one utilizing spatiotemporal speckle fields generated by a multimode fiber for parallel ghost imaging, the other based on nonlinear speckle measurement and deep learning.

### A. Compressive radio-frequency receivers

Nyquist rate sampling of Gigahertz-band radio frequency (RF) signals rapidly generates huge amounts of data. To address this general issue, compressive sensing (CS) techniques are developed for sparse signals and images. Electronic CS systems suffer timing jitter and amplitude noise. Although microwave photonic CS systems have equivalent issues, in many cases, the distortions are static or lower in frequency and amenable to calibration. Previously, pseudo-random bit sequences have been created to modulate the optical carriers for compressive sensing. Recently, optical speckle patterns, generated by multimode fibers or waveguides, are employed for sparse RF signal recovery.[218,254,255]

Figure 19 is a schematic showing a multimode waveguide/fiber replacing a 2D SLM in generating pseudo-random bit sequences in a modulated wideband converter.[218] Femtosecond pulses from a mode-locked laser (MLL) are launched into a dispersion-compensating fiber (DCF), which stretches the pulse to the inter-pulse time. Then, the optically chirped pulses pass through a Mach–Zehnder modulator (MZM) that imprints the RF signal on the optical intensity and subsequently enter a multimode waveguide/fiber. The transmitted signals are spatially split at the output of the guide and directed to an array of photodiodes. The integration times of the photodiodes are matched to the period of mode-locked pulses, and the electrical signals from the photodiode array are digitized by an array of analog-to-digital converters (ADCs) clocked to the pulse repetition rate. An optional fiber mode scrambler is placed near the input end of the fiber to fully excite the guided modes. The time-wavelength mapping is depicted by the rainbow-colored pulse icons. The output speckle pattern from the multimode waveguide varies with wavelength, and hence with time. The optical spectrum recovered from the speckle pattern provides temporal variation of the RF signal through the time-wavelength mapping. CS algorithms are employed to recover different types of sparse signals, for example, sparse in time, in frequency, or after the Harr wavelet transform.[218]

Instead of mapping from space to wavelength and then to time, it is possible to combine them for a direct mapping from space to time
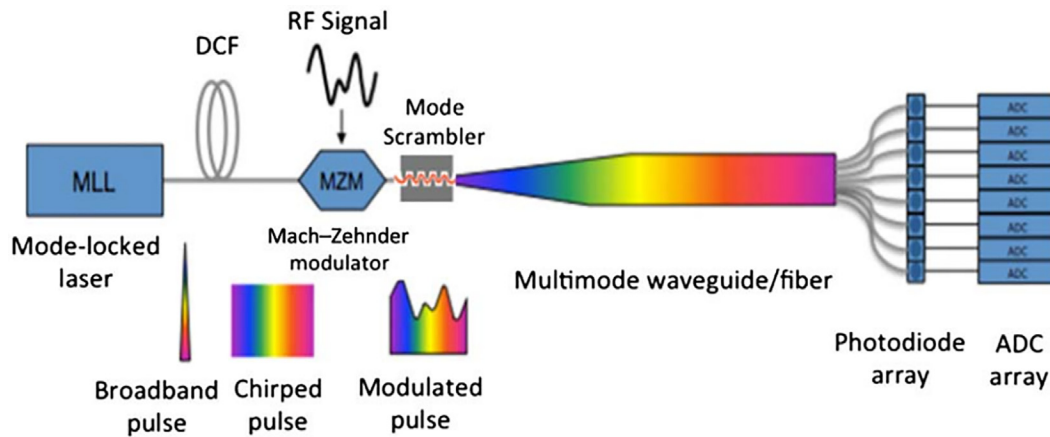
**FIG. 19.** Compressive sensing of RF signals. Reprinted with permission from Valley *et al.*, Opt. Lett. **41**, 11 (2016). Copyright 2016 The Optical Society. Schematic of RF signal recovery from optical speckle measurement. An broadband optical pulses from a mode-locked laser (MLL) are stretched by a dispersion compensating fiber (DCF), and the RF signals are applied to the chirped pulse in a Mach–Zehnder modulator (MZM), and then, the modulated pulses are sent through a multimode waveguide/fiber, and the transmitted speckle patterns are detected by a photodiode array.

or to RF. In addition to the RF signal amplitude, its relative phase (with respect to the optical pulse train from the mode-locked laser) can be recovered from the speckle measurement. The mapping matrix has two columns for each RF tone, which are referred to as in-phase and quadrature components. Three methods have been explored for calibration: the first one estimates the two columns from measurements with pairs of pulses, the second method fits the data as a function of the relative RF phase, and the third one is based on singular value decomposition (SVD) of the calibration matrix.[254] Finally, a penalized $l_1$ norm method recovers the amplitude, phase, and frequency of sparse RF signals. Using a 5-m-long MMF (0.22 NA step-index, 105-$\mu$m core), RF signals with one tone or two tones in the 2–19 GHz band are reconstructed with 100 MHz resolution in a single 4.5-ns pulse.

To reduce the device footprint, the MMF is replaced by an 11-cm-long multimode waveguide (96 $\mu$m wide and 220 nm thick), which is integrated with a multi-port splitter and a grating coupler array in a photonic circuit.[255] The planar waveguide is wrapped in a spiral geometry and produces random projections for CS via optical speckle. A precise analog signal routing is supported by two integrated structures, waveguide bus trombone flare and matched 90° bus bend, in the silicon chip. 16 RF channels, each with an effective sampling rate of 35 MSps (mega samples per second), are able to recover RF signals across a 2 GHz bandwidth from 2.5 to 4.5 GHz. Compared with direct Nyquist sampling, which requires 4 GSps, the CS requires $4000/(35 \times 16) = 7$ times fewer recorded samples and a maximum sampling rate that is $4000/35 = 114$ times smaller.[255] Sampling well below the Nyquist limit reduces the need for data storage, shortens data-payload transmission time, and reduces the overall receiver size, weight, and power.

## B. Single-shot full-field measurement of optical pulses

Full-field (both amplitude and phase) characterization of ultrashort optical pulses with femtosecond to attosecond pulse duration is crucial to ultrafast science. Existing sensors are not fast enough to

directly resolve such short pulses, and the pulses are recovered indirectly, often through algorithmic methods. Various schemes have been developed for multi-shot measurements, which require trains of identical pulses. However, in many cases the probed pulses are not reproducible, prompting the development of single-shot characterization methods.

The single-shot measurement is more challenging for several reasons. First, a trade-off between the temporal range $\Delta t$ and resolution $\delta t$ limits the time-bandwidth product $\Delta t/\delta t$, where $1/\delta t$ is proportional to the spectral bandwidth. Second, the single-shot measurement is highly sensitive to noise, as there is no averaging over multiple pulses and the power of incoming signal is always limited. Third, a full-field characterization requires recovering the amplitude $A(t)$ and phase $\theta(t)$ simultaneously, and both may evolve rapidly in time $t$.

A Fourier transform of the temporal field $E(t) = A(t)e^{i\theta(t)}$ gives the spectral field $E(\omega) \equiv \mathscr{F}[E(t)] = A(\omega)e^{i\theta(\omega)}$. Simultaneous reconstruction of spectral amplitude $A(\omega)$ and phase $\theta(\omega)$ will recover $E(\omega)$ and $E(t)$. As shown in Sec. IV, the power spectrum $I(\omega) = |E(\omega)|^2 = [A(\omega)]^2$ can be reconstructed from a time-integrated intensity measurement of optical speckle pattern generated by a random scattering medium or a multimode fiber/waveguide. However, such speckle pattern does not contain any information of spectral phase, thus preventing complete pulse recovery.

Lately, two methods are developed for single-shot full-field measurement of optical pulses using (i) spatiotemporal speckles and (ii) nonlinear speckles. This subsection will introduce these methods. While method (i) employs a reference pulse, method (ii) is reference-free or self-referenced.

### 1. Parallel temporal ghost-imaging

Figure 20(a) illustrates the single-shot full-field measurement using spatiotemporal speckle pattern out of a multimode fiber (MMF).[256] A linearly polarized laser pulse with known field $f(t)$ is split into two arms of a Mach–Zehnder interferometer. In one arm, the pulse is launched into a multimode fiber (MMF) to create a
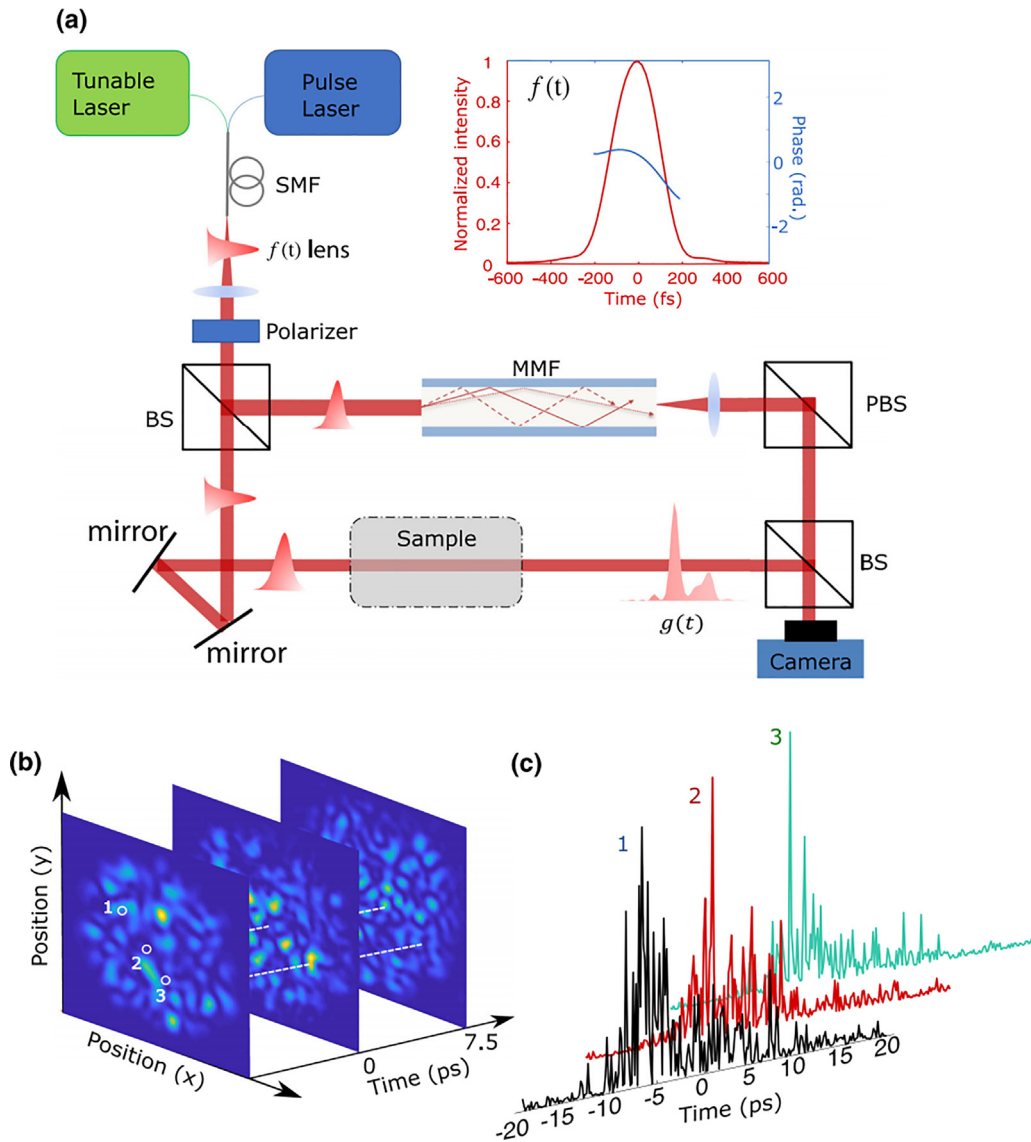
**FIG. 20.** Single-shot pulse characterization using spatiotemporal speckles. Reprinted with permission from Xiong *et al.*, Opt. Lett. **45**, 2462 (2020) Copyright 2020 The Optical Society. (a) Schematic of an interferometric setup for calibration of spatiotemporal speckle field generated by a reference pulse through a multimode fiber (MMF). Its interference with a signal (transmitted pulse of a sample) at a slow camera enables full field recovery of the signal. Inset: intensity (red solid line) and phase (blue solid line) of the reference pulse launched into the MMF. (b) Spatial field amplitude distribution of a reference pulse transmitted through the MMF evolves with time. (c) Transmitted field amplitudes at different spatial positions of the fiber output exhibit distinct temporal fluctuations.

spatiotemporal speckle field $E_s(\mathbf{r}, t)$ in transmission. In the other arm, the pulse interacts with a sample, and the transmitted/reflected field $g(t)$ interferes with $E_s(\mathbf{r}, t)$. The time-integrated intensity pattern $I_p(\mathbf{r}) = \int |E_s(\mathbf{r}, t) + g(t)|^2 dt$ is recorded by a slow camera. By applying a Hilbert filter in the Fourier domain of $I_p(\mathbf{r})$, the interference term $I_q(\mathbf{r}) = \int dt [E_s(\mathbf{r}, t) g^*(t) + E_s(\mathbf{r}, t)^* g(t)]$ is extracted.

In the frequency domain, $E_s(\mathbf{r}, \omega) = \mathscr{F}[E_s(\mathbf{r}, t)] = T(\mathbf{r}, \omega) F(\omega)$, where $T(\mathbf{r}, \omega)$ is the frequency-resolved field transmission matrix of the MMF, and $F(\omega) = \mathscr{F}[f(t)]$. The interference term can be expressed in the frequency domain as

$$I_q(\mathbf{r}) = \begin{bmatrix} T(\mathbf{r}, \omega) f(\omega) & T^*(\mathbf{r}, \omega) f^*(\omega) \end{bmatrix} \begin{bmatrix} g^*(\omega) \\ g(\omega) \end{bmatrix}, \quad (20)$$

where $G(\omega) = \mathscr{F}[g(t)]$. Once $T(\mathbf{r}, \omega)$ is calibrated and $F(\omega)$ is known, $G(\omega)$ can be retrieved from $I_q(\mathbf{r})$, and an inverse Fourier transform gives $g(t)$.

The temporal range $\Delta t$ of the single-shot measurement is set by the temporal length of $E_s(\mathbf{r}, t)$, which is inversely proportional to the spectral correlation width of the MMF. A fiber with longer length and/or stronger modal dispersion has a faster spectral decorrelation and

can cover a longer time window. The temporal resolution $\delta t$ is equal to the temporal speckle size, which is given by the inverse of the spectral bandwidth of the reference pulse. A reference pulse of broader bandwidth (not necessarily transform-limited in time) provides higher temporal resolution. Therefore, the temporal range and resolution can be tuned separately by varying the parameters of the fiber and the reference pulse. Experimentally, single-shot full-field measurement with a 1.8-m-long MMF (105 $\mu$m core diameter, 0.22 NA) provides 230 fs temporal resolution over 35 ps window, and the time-bandwidth product is 152.[256]

The time-bandwidth product reflects the number of independent temporal channels that are measured simultaneously. Its upper bound is given by the number of uncorrelated time traces generated by the MMF, which is equal to the number of guided modes in the fiber. The time-bandwidth product for a MMF with a large core and a high NA may well exceed 1000, and a further increase is possible with a bundle of MMFs.[215]

This single-shot measurement scheme is equivalent to parallel ghost imaging in time.[257] While the conventional ghost imaging relies on sequential generation of different temporal waveforms for sampling, the MMF simultaneously creates many distinct time traces in different spatial channels to sample the signal [Fig. 20(c)]. The complex yet deterministic spatiotemporal speckle field enables parallel sampling in a single shot for a full-field recovery, eliminating the requirement for repetitive signals.

The spatiotemporal coupling of broadband light in a MMF has also been employed for axial reflectivity profiling.[258] The closely spaced yet distinct propagation constants of various spatiotemporal modes in a MMF yield a set of spatially distributed encoding functions that can be used for depth referencing. A signal that is delayed by reflection at a specific sample depth only interferes with the path length-matched encoding function [Fig. 20(b)] and creates a distinct speckle pattern that is unique to this depth. An arbitrary sample reflectivity profile produces a linear superposition of the associated speckle patterns. By calibrating the random encoding functions, the 1D sample depth profile is reconstructed from a single recording of the interference pattern without the need for any mechanical or optical scanning. Such configuration can be considered as spatially multiplexed low-coherence interferometry and is a parallel implementation of ghost optical coherence tomography.[259] Experimentally, axial depth profiling is demonstrated with bandwidth-limited resolution of 13.4 $\mu$m over a range of 13.4 mm.[258] By varying the MMF length, the depth range is scaled from several millimeters to well beyond one centimeter, relaxing the challenging hardware requirements of achieving similar performance with conventional spectrometer-based coherence gating.

### 2. Nonlinear speckle and deep learning

The method described in Subsection VII B 1 relies on a known optical pulse that is mutually coherent with the unknown signal. In this subsection, a reference-free time-integrated measurement scheme will be introduced to enable stand-alone single-shot characterization of ultrafast pulses.

The key for full-field recovery is retrieving the spectral phase $\theta(\omega)$, as the spectral amplitude $A(\omega)$ is already reconstructed from the linear speckle pattern. Measuring the relative phase of different spectral components in a pulse requires these components to interfere,

but distinct frequencies do not interfere in a linear, time-integrated detection. To retrieve the spectral phase without any reference, a nonlinear material is placed behind a MMF to create a speckle pattern via two-photon absorption or sum-frequency generation.[260,261]

As illustrated in Fig. 21(a), the propagation of a signal pulse in the MMF remains linear, so that the transmitted light is related to an incident signal by the field transmission matrix: $E_t(\mathbf{r}, t) = \mathscr{F}^{-1}[T(\mathbf{r}, \omega) A(\omega)]$, where $\mathscr{F}^{-1}$ denotes the inverse Fourier transform. The time-integrated linear speckle pattern $I_{1p}(\mathbf{r}) = \int |E_t(\mathbf{r}, t)|^2 dt = \int |T(\mathbf{r}, \omega)|^2 |A(\omega)|^2 d\omega$ encodes only the spectral amplitude $A(\omega)$ of an input signal. The time-integrated nonlinear speckle pattern $I_{2p}(\mathbf{r}) = \int |E_t(\mathbf{r}, t)|^4 dt$ can be expressed as

$$\begin{aligned}
I_{2p}(\mathbf{r}) = \iiint & d\omega_1 \, d\omega_2 \, d\omega_3 \, |T(\mathbf{r}, \omega_1)| \, A(\omega_1) \, |T(\mathbf{r}, \omega_2)| \, A(\omega_2) \\
& \times |T(\mathbf{r}, \omega_3)| \, A(\omega_3) \, |T(\mathbf{r}, \omega_1 - \omega_2 + \omega_3)| \, A(\omega_1 - \omega_2 + \omega_3) \\
& \times e^{i[\theta(\omega_1) - \theta(\omega_2) + \theta(\omega_3) - \theta(\omega_1 - \omega_2 + \omega_3)]} \\
& \times e^{i[\theta_{TM}(\mathbf{r}, \omega_1) - \theta_{TM}(\mathbf{r}, \omega_2) + \theta_{TM}(\mathbf{r}, \omega_3) - \theta_{TM}(\mathbf{r}, \omega_1 - \omega_2 + \omega_3)]},
\end{aligned} \quad (21)$$

where $\theta_{TM}(\mathbf{r}, \omega)$ is the phase of $T(\mathbf{r}, \omega)$. $I_{2p}(\mathbf{r})$ encodes the spectral phase $\theta(\omega)$ of the signal, because different spectral components interfere in the nonlinear optical process. Moreover, the complex interference eliminates ambiguity in the sign of spectral phase, allowing the direction of time to be recovered [Figs. 21(b) and 21(c)]. This is advantageous over other self-referenced nonlinear techniques that cannot distinguish the direction of time.[262]

In practice, retrieving the input spectral phase $\theta(\omega)$ from the nonlinear speckle intensity $I_{2p}(\mathbf{r})$ is highly non-trivial, because the inverse mapping from $I_{2p}(\mathbf{r})$ to $\theta(\omega)$ is complicated. Conventional phase retrieval algorithms are sensitive to noise in the nonlinear snapshot measurement and thus cannot provide a reliable recovery. A deep neural network is employed to learn the nonlinear mapping from $I_{2p}(\mathbf{r})$ to $\theta(\omega)$.[260] Once the field transmission matrix $T(\mathbf{r}, \omega)$ of the fiber is calibrated, it is straightforward to calculate the nonlinear speckle pattern for any input pulses using Eq. (21). A large amount of data are numerically synthesized to train a convolutional neural network. Furthermore, deep learning is combined with compressive sensing by representing the spectral phase in a sparse basis to dramatically reduce the number of parameters that the neural network predicts. Measurement noise and fiber fluctuation are incorporated to the training data, so that the trained network is robust and outperforms classical algorithms.

Since the nonlinear speckle pattern encodes both amplitude and phase information, it may be used to recover $A(\omega)$ and $\theta(\omega)$ simultaneously, eliminating the linear speckle measurement. Numerically, a deep neural network is trained for pulse amplitude and phase recovery.[261] This technique is shown to be robust to noise and inaccuracy in system parameters, and capable of reconstructing ultrashort pulses at low SNR. It mitigates the need for iterative optimization, which is usually slow and hampered by the presence of noise. Therefore, the deep learning method is advantageous for real time probing of ultrafast processes under noisy conditions.

The speckle-based pulse characterization scheme can be tuned to measure optical pulses of varying length. The temporal range of measurement is determined by the spectral decorrelation of the MMF, and the temporal resolution depends on the spectral bandwidth over which the field transmission matrix is calibrated. Experimentally, a 1.3-m-
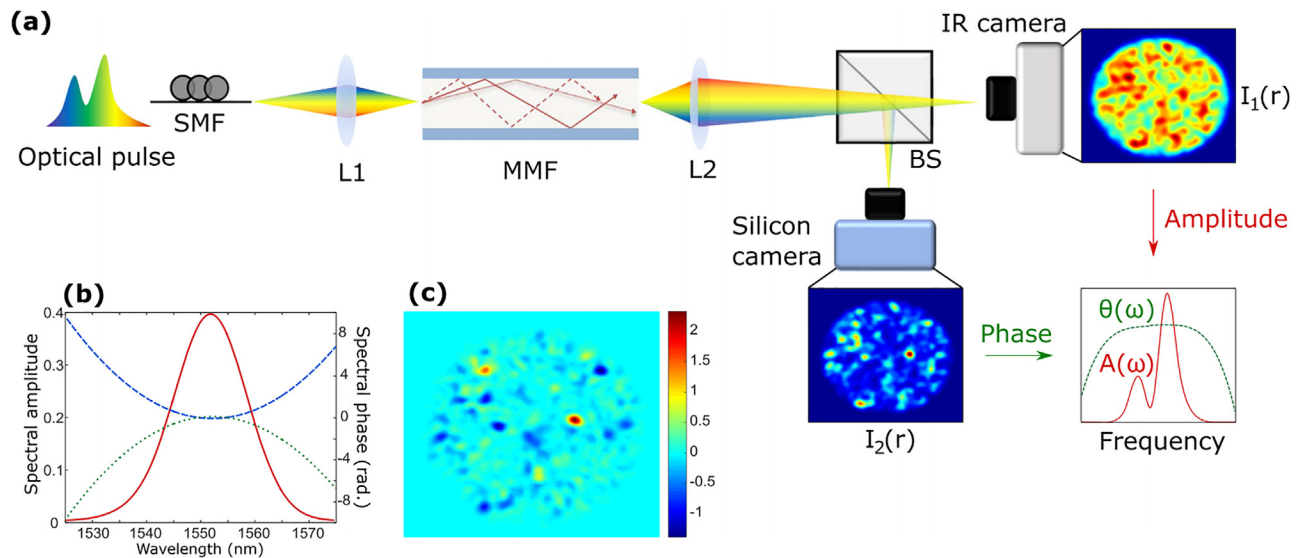
**FIG. 21.** Full-field recovery with linear and nonlinear speckles. Reproduced with permission from Xiong *et al.*, APL Photonics **5**, 9 (2020). Copyright 2020 AIP Publishing LLC. (a) Schematic of experimental realization. An optical pulse at $\lambda = 1550$ nm is delivered via a single-mode fiber (SMF) to a multimode fiber (MMF). At the MMF output, time-integrated linear speckle pattern $I_{1p}(\mathbf{r})$ is recorded by an IR camera via one-photon absorption, and nonlinear speckle pattern $I_{2p}(\mathbf{r})$ recorded by a silicon camera via two-photon absorption. The spectral amplitude $A(\omega)$ and phase $\theta(\omega)$ of the input pulse are recovered from $I_{1p}(\mathbf{r})$ and $I_{2p}(\mathbf{r})$, respectively. (b) An optical pulse has spectral amplitude $A(\omega)$ (red solid line) and phase $\theta(\omega)$ (blue dashed line). The sign of its phase flipped to $-\theta(\omega)$ (green dotted line), which corresponds to temporal inversion with phase conjugation. (c) Difference in $I_{2p}(\mathbf{r})$ between two pulses with opposite spectral phases in (b) indicates the sign of spectral phase can be recovered from the nonlinear speckle pattern.

long step-index fiber with 105 $\mu$m core and 0.22 NA is calibrated over a wavelength range of 1525–1575 nm, and provides a temporal resolution of 160 fs over a time window of 30 ps. The resolution can be further increased by calibrating the MMF over a larger bandwidth, and the temporal range can be extended by using a longer fiber with faster spectral decorrelation. Finally, the MMF may be replaced by a random scattering medium or an on-chip multimode waveguide.

## VIII. RANDOM LASERS

Next, we switch to disordered systems that possess optical gain and nonlinearity. In Sec. VIII A, we introduce random lasers and illustrate their distinction from conventional lasers. The applications of random lasers to spatial coherence engineering and speckle-free imaging are covered in Secs. VIII B and VIII C. In analog to super-resolution microscopy, super-resolution spectroscopy is achieved with a random laser in Sec. VIII. Section VIII E presents the random fiber lasers based on stimulated Raman scattering, which produce high-power with high efficiency and exhibit nearly octave wavelength tuning. Section VIII F shows that structural disorder can suppress temporal instability in a semiconductor laser.

### A. Introduction of random laser

The essential ingredients of a laser are a gain material that is optically or electrically pumped to amplify light through stimulated emission, and a cavity that increases the dwell time or path length of light in the gain medium to enhance amplification. Although most lasers produce emission with high spatial and temporal coherence, the first-order coherence is not exclusive to lasers.[263] What distinguishes a laser

from a thermal light source is the second-order coherence that results from gain saturation.

Unlike conventional lasers relying on mirrors or periodic structures to trap light, a random laser utilizes multiple scattering in a disordered gain medium for optical confinement and feedback.[264–266] It has been implemented in many material systems, including powders,[267] colloids,[268] biological tissues,[269] polycrystalline films,[270] polymers,[271] optical fibers,[272] and cold atomic vapors.[273] The lasing frequencies range from ultraviolet[274] and visible[275] to infrared[276] and Tera-Hertz.[277] This section will cover some applications of random lasers.

### B. Spatial coherence engineering

Despite high radiance, high efficiencies, and good spectral control, conventional lasers have not been widely used for illumination in full-field imaging and display applications because of coherent imaging artifacts. Such artifacts originate from the interference of scattered or diffracted waves during image formation, and the resulting intensity modulations appear as additional features that are not present in the object, thereby corrupting the image. The most common manifestation of coherent artifacts is speckle noise, which occurs when a rough object or scattering environment introduces random phase delays among mutually coherent photons that interfere at the detector. To avoid speckle, thermal light sources and light-emitting diodes (LEDs) are commonly used for illumination in most parallel imaging and projection applications, despite having lower power per mode, poorer collection efficiency, and less spectral control than lasers. The limitation of source brightness is particularly pronounced in applications requiring high-speed imaging or imaging with absorbing or scattering background.

For parallel imaging and projection applications, the ideal illumination source will combine the high brightness of a laser and the low spatial coherence of a lamp. The common approach to achieve this combination is reducing the effective spatial coherence of a traditional laser using a time-varying scattering system such as a moving diffuser[278] or a colloidal solution.[279] Many speckle patterns are generated sequentially and summed to reduce the intensity contrast $C_t$ to $1/\sqrt{N_r}$, where $N_r$ is the number of uncorrelated speckle patterns in the sum. To lower the speckle contrast below the level of human perception $C_t < 3\%$, about 1000 different speckle patterns are needed for averaging, and it takes time to create them in series, which mitigates the advantage of using bright sources like lasers for high-speed imaging applications. Instead of reducing the spatial coherence with moving scatterers outside the laser cavity, incorporation of (static) scatterers in a laser cavity will directly generate emission with low spatial coherence.

Once numerous scattering particles are added to a gain material, the spontaneously emitted photons will be scattered many times and undergo a "random walk."[280] Multiple scattering increases the path length of photons in the gain medium, enhancing the stimulated emission of photons.[281] Furthermore, the scattered photons may return to spatial positions they have visited before, providing feedback for lasing oscillation.[282] Most random lasers operate in the highly multimode regime. Individual lasing modes, formed by interference of scattered waves, have distinct frequencies and spatial structures.[283] If the frequency spacing between neighboring lasing modes $\delta\omega$ exceeds their linewidth, they become mutually incoherent on a timescale longer than $1/\delta\omega$.[284] The spectral repulsion of random lasing modes accelerate spatial decoherence. An incoherent sum of emission from many lasing modes, each producing a distinctly speckled wavefront, leads to low spatial coherence.[285–288] Since the number of random lasing modes and their spatial structures is dictated by the amount of scattering in the random medium as well as the dimension and shape of the excitation region, the spatial coherence of random lasers can be tuned by varying the density of scatterers or the pump beam profile.

## C. Speckle-free imaging

A random laser with low spatial coherence can suppress speckle noise and improve the image quality, especially when imaging in a scattering environment.[289–295] Figure 22 shows full-field imaging through a (static) scattering film of a US Air Force resolution test chart with two illumination sources. Under spatially coherent illumination with a He:Ne laser, interference among scattered photons creates strong speckle noise that corrupts the image beyond recognition. In contrast, when illuminating with a random laser of low spatial coherence, scattered photons do not interfere, instead producing a uniform background. Although the photons that are scattered and mismapped to what would otherwise be dark regions of an image raise the background level and lower the image contrast, the features of the object remain clearly visible.

The speckle noise depends not only on the coherence properties of the illumination source, but also on the imaging optics, including the ratio of the numerical aperture for observation to that for illumination.[289] Therefore, the degree of spatial incoherence in illumination that is needed to suppress speckle noise depends on the parameters of
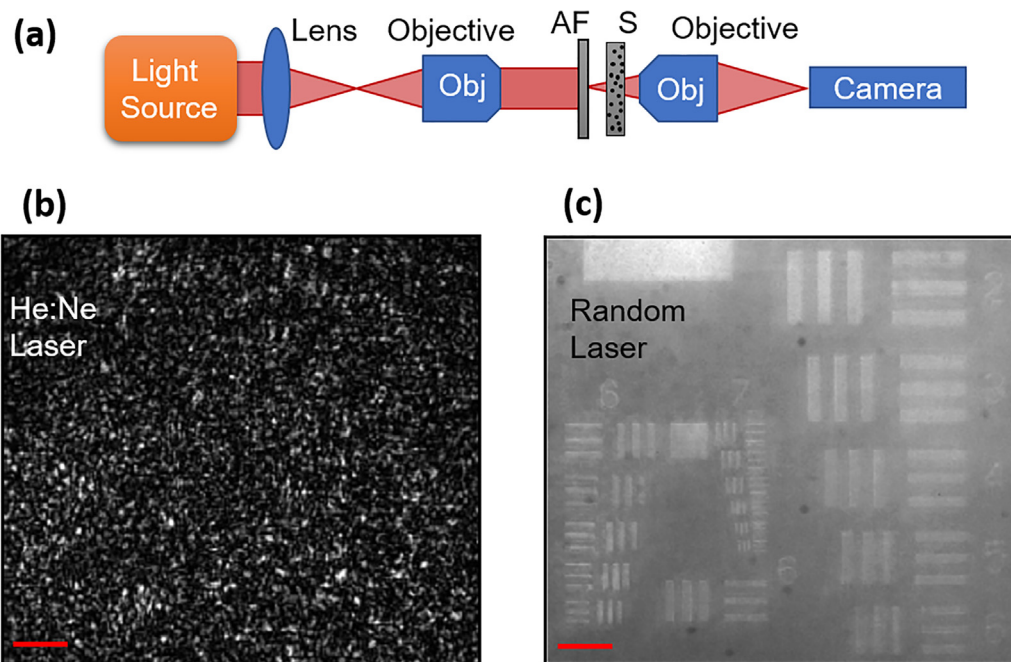


**FIG. 22.** Speckle-free imaging under random laser illumination. Reprinted with permission from Redding *et al.*, Nat. Photonics **6**, 355 (2012). Copyright 2012 Nature Publishing Group. (a) Schematic of full-field imaging of a US Air Force resolution test chart (AF) through a thin static scattering film (S). (b) Image is corrupted by speckle noise when the object is illuminated by a coherent He:Ne laser ($\lambda = 633$ nm). (c) Image is free of speckle noise when the illumination source is switched to a random laser with low spatial coherence.

a specific application, such as the amount of scattering or diffraction, the imaging resolution, etc. Correspondingly, a random laser can be tailored to provide sufficiently low spatial coherence for speckle suppression, while maintaining relatively high power per mode as compared to spatially incoherent sources such as lamps and LEDs. For example, to reduce the speckle contrast below the level observable by humans, it is sufficient to have 1000 spatial modes lase independently, which can be realized by engineering a random laser, but ordinary lamps and LEDs emit photons into far more modes, thus having lower power per mode.

A quantitative measure of the source brightness is the photon degeneracy parameter, which gives the number of photons per coherence volume.[263] It is proportional to the spectral radiance, a radiometric measure of the amount of radiation through a unit area and into a unit solid angle within a unit frequency bandwidth. The photon degeneracy parameters for random lasers are several orders of magnitude higher than those of lamps and LEDs.[289] The greatly improved brightness, together with short decoherence time, enables much higher speed for full-field imaging of transient physical processes. For example, a random laser is triggered to produce a short illumination flash at a well-defined time, providing uniform, speckle-free illumination for time-resolved microscopy.[296,297]

### D. Super-resolution spectroscopy

Super-resolution microscopy includes a set of imaging techniques that overcome the diffraction limit. One example is the single-molecule localization microscopy, which relies on spatially sparse activation of fluorescent molecules with a sample. Each molecule creates an isolated Gaussian-shaped disk in the image, and its center location can be fit with sub-pixel resolution. Although only a small number of molecules are recorded in one image, repetitive activation and recording under constant conditions allows full reconstruction of an object with a spatial resolution much finer than that of the imaging system.

The concept of super-resolution is extended to spectroscopy, using a random laser for sparse sampling in frequency.[298] A 3D disordered sample with large gain volume has a huge number of spatial modes that may lase. If light scattering is relatively weak, these modes are spatially extended and overlap with each other. Their competition for optical gain will lead to spectral repulsion of the lasing modes.[299] Since most of these modes have similar lasing thresholds, which ones will lase depends on initial seeding from spontaneous emission.[300] When pumped by a short pulse, the initial photons spontaneously emitted into a subset of spatial modes will trigger the stimulated emission process, leading to a rapid growth of the number of photons in these modes. Hence, these modes tend to lase first; and once they lase, they will prevent other modes from lasing by saturating optical gain. For each pump pulse, only a small number of spatial modes manage to lase, correspondingly the emission spectrum contains a few narrow peaks. Due to spectral repulsion of the lasing modes, the emission peaks are well separated in frequency.[301] As the spontaneous emission events are stochastic and will seed different modes for individual pump pulse, the lasing modes vary from pulse to pulse, producing a distinct set of peaks in the emission spectrum. Because the spectral density of modes is uniform in a random medium, the lasing peaks collected over a large ensemble of pump pulses will cover the entire gain spectrum.

The sparse random lasing peaks in individual emission spectra provide spectral super-resolution when probing the frequency response of a sample. By recording the peak amplitudes and frequencies in incident and transmitted spectra taken with a series of random laser pulses, the transmission function of a sample is reconstructed.[298] With only a few prominent peaks in each lasing spectrum, their center frequency is retrieved with high precision beyond the spectrometer resolution. Once a few thousands of lasing peaks are collected and analyzed, a plot of their amplitude change vs their center frequency gives the transmission function of the sample.

Figure 23 shows the transmission spectrum of a low-finesse Fabry–Pérot (FP) etalon, which is reconstructed with random lasing emission from a dye solution with ZnO nanoparticles.[298] The dye molecules are optically pumped with frequency-doubled Nd:YAG laser pulses. The pump power and excitation volume are adjusted to keep the number of random lasing peaks in each shot low enough, so that the peaks are well separated in frequency. A threefold increase in spectral resolution is obtained. The ultimate resolution limit is set by the linewidth of individual lasing modes.

We note that amplified spontaneous emission (ASE) also creates sharp spikes in the emission spectrum, which originate from the spontaneously emitted photons taking long propagation paths inside a random medium and pick up a large amplification. These spikes are intrinsically stochastic and vary from shot to shot. Since different ASE spikes originate from independent spontaneous emission events, their frequencies are uncorrelated, and the Poisson statistics of the frequency spacing of neighboring ASE spikes results in a high probability of spectral bunching of ASE spikes in a single shot.[302] Once the pumping level is above the random lasing threshold, the lasing peaks have much higher amplitudes than the ASE spikes, and the inherent spectral separation of random lasing modes greatly reduces the probability of having two almost-degenerate peaks in the same shot spectrum. This is the key to sparse sampling in frequency.

While it is experimentally demonstrated in the visible frequency, the spectral super-resolution can be obtained in different frequencies ranging from ultraviolet to terahertz, where random laser sources are already available. Furthermore, this technique is robust and does not require any stabilization of the source, which is necessary in other high-resolution spectroscopy techniques such as frequency comb spectroscopy.

### E. High power with high efficiency

There has been rapid progress in the development of random fiber lasers that generate high power with high efficiency and provide extremely broad wavelength tunability.[380] While the fiber waveguide geometry provides transverse confinement for light, in the longitudinal direction the naturally present refractive index irregularities causes Rayleigh scattering, which is weak but sufficient for random lasing in a long fiber.[272] Much stronger feedback is supplied by artificial structures such as fiber Bragg gratings (FBGs) with random phase and/or amplitude modulation[303] or an array of FBGs with randomly varying spacing,[304] to realize lasing in short fibers.

In addition to stimulated emission, optical gain can be provided by stimulated Raman scattering (SRS) or stimulated Brillouin scattering (SBS) in a fiber.[305] One unique property of SRS-based random distributed feedback fiber lasers is the ultra-wide wavelength tunability, as both stimulated Raman scattering gain and Rayleigh scattering
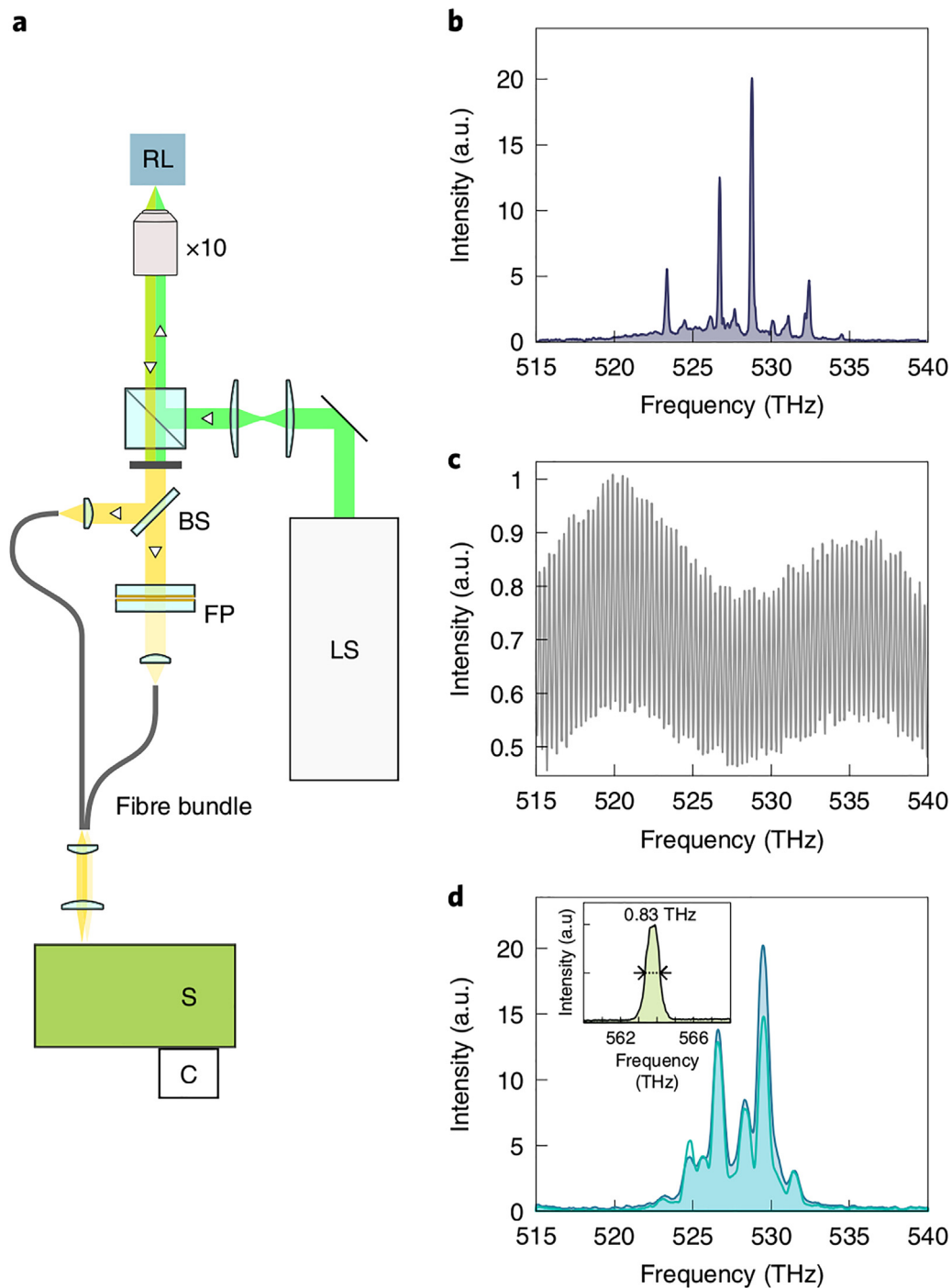
**FIG. 23.** Super-resolution spectroscopy using random laser emission. Reprinted with permission from Boschetti *et al.*, Nat. Photonics **14**, 177 (2020). Copyright 2020 Nature Publishing Group. (a) A random laser (RL) is optically pumped by a pulsed laser source (LS) with an objective lens (×10), and its emission in backward direction is collected by the same objective. A beam splitter (BS) sends a reference signal to a first multimode fiber, and the probe passes through an Fabry–Pérot (FP) etalon before being focused on a second fiber. The two fibers are bundled and simultaneously imaged onto the entrance slit of a spectrometer (S) so that they are spectrally dispersed and collected by a single camera (C) at the spectrometer output port. (b) A single-shot transmission spectrum of the FP etalon (cyan) is compared to its respective reference spectrum of random laser emission (light blue curve). Both are measured with a low-resolution spectrometer whose instrumental response is shown in the inset. (c) Transmission curve of the FP etalon, obtained by sparse sampling with a few thousands of random laser emission spectra, agrees to the one measured with a high-resolution spectrometer (not shown). (d) Transmission curve obtained with a broadband lamp illumination fails to capture the fine features in the transmission function of the FP etalon.

feedback are available at any wavelength.[306–311] When pumped by a Yb:doped fiber laser or a narrow-band ASE source, cascaded Raman lasing up to the 10th order is obtained with increasing pump power.[312–316] With wavelength tuning of the pump light, the Raman emission fills the spectral gaps between cascaded Stokes. As shown in Fig. 24, continuous wavelength tuning from 1 $\mu$m to 1.9 $\mu$m is demonstrated experimentally.[311]

Another striking feature of the SRS random fiber laser is high-efficiency high-power generation.[317] In order to concentrate all power in the first-order Raman Stokes, the fiber length is chosen to be relatively short to avoid power transfer to higher orders.[318–324] One end of the fiber is terminated by a highly reflective FBG to ensure the total power output from the other end. With a 90-meter-long large-mode-area fiber, an output power of 919 W is obtained at $\lambda = 1150$ nm.[324] The random distributed feedback from Rayleigh scattering leads to a specific power distribution along the fiber, making the generation efficiency superior to that of a conventional fiber laser with a Fabry–Pérot cavity.[315,325,326] The maximum optical conversion efficiency has reached 89%, as a result of highly efficient Raman gain and low quantum defect. Another advantage is the absence of photo-darkening effect that happens to high-power fiber lasers based on stimulated emission.

High spectral purity and clean output beam profile are obtained with random distributed feedback lasers. The temporal stable emission is used to seed a kilowatt fiber amplifier.[327] The absence of nonlinear

spectral broadening, which is common to traditional master-oscillator power-amplifiers, allows further power scaling and spectral beam combination for high-power narrow-linewidth applications. Thanks to its wavelength flexibility and low background noise, a random fiber laser is used to pump an optical parametric oscillator (OPO) to achieve tunable mid-infrared emission.[328] Visible light is generated via second harmonics of a linearly polarized near-infrared random fiber laser emission with high conversion efficiency.[329] Novel applications of random fiber lasers in telecommunication and remote sensing have been explored, see Refs. 330 and 331 and references therein.

## F. Suppression of lasing instability

Instabilities and chaotic dynamics in the form of irregular pulsations are common to high power multimode lasers, hindering their applications in material processing, large-scale displays, laser surgery, and pumping other lasers. The spatiotemporal instabilities are intrinsic and caused by nonlinear light–matter interactions. For example, in a broad-area edge-emitting semiconductor laser, spatial hole burning and lensing effects results in formation of filaments, which are prone to modulational instabilities.[332] An efficient way of suppressing lasing instabilities while maintaining multimode operation is using a wave-chaotic cavity.[333] In such a cavity, the interference of many propagating waves with random phases form speckles, which prevents self-focusing and filamentation, leading to stable lasing operation.
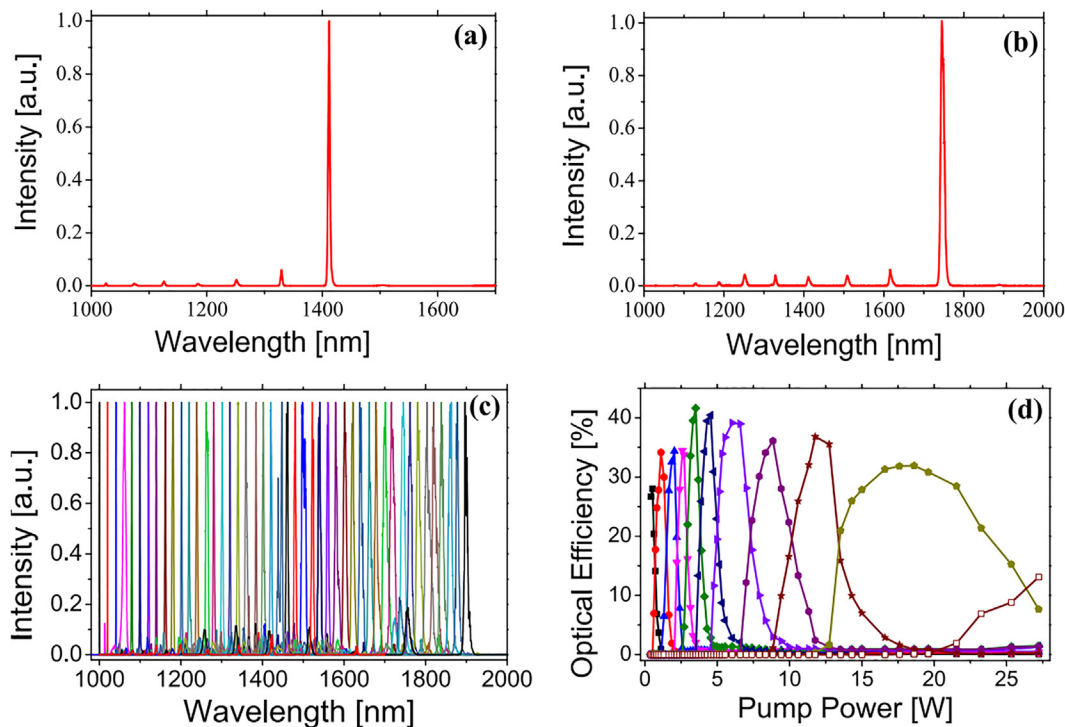


**FIG. 24.** Nearly octave wavelength tuning of a fiber random laser. Reproduced with permission from Zhang *et al.*, Sci. Rep. **7**, 42611 (2017). Copyright 2017 Author(s); licensed under a Creative Commons Attribution (CC BY) license. A random distributed feedback fiber laser generates cascaded Raman Stokes up to the 10th order with increasing pump power. (a) and (b) are the output spectra of the laser when optimized for the 6th and 9th order Raman Stokes by tuning the pump power. The pump wavelength is 1025 nm. (c) shows the random fiber laser emission spectra with continuous wavelength tuning from 1 to 1.9 $\mu$m. (d) shows the optical efficiencies for different order Raman Stokes light as a function of the pump power.

Even in a narrow-stripe cavity that supports only one transverse mode, lasing dynamics is not always stable. In a Fabry–Pérot cavity formed by reflection from two end facets, lasing occurs in many longitudinal modes with equal frequency spacing. Optical interference between two modes creates periodic intensity modulation, and a refractive index grating is formed via optical nonlinearity. A third mode then diffracts from this grating, resulting in energy transfer among the lasing modes. The mode hopping and switching become more frequent and irregular in time at high pump power.[334]

To suppress lasing instability, random variation of the refractive index is introduced to an 1D dielectric stripe, as shown in Fig. 25(a). Multiple reflected waves interfere to form lasing modes with irregular frequency spacing.[333] The mode structures also become irregular with varying spatial scales. Such irregularities disrupt coherent nonlinear interactions among the modes via multi-wave mixing, effectively blocking mode coupling and energy transfer. Numerical simulations reveal stable lasing dynamics over a wide range of pump power, in contrast to the cavity without refractive index fluctuation [Figs. 25(b) and 25(c)]. This simple approach is robust and generally applicable to other types of high-power lasers exhibiting instabilities.

## IX. SUMMARY AND PERSPECTIVES

There are many ways to harvest disorder for photonic device applications, and it is impossible to cover all of them in this review. For example, randomly textured surfaces in solar cells have enhanced the efficiency of trapping and absorption of broadband light over a
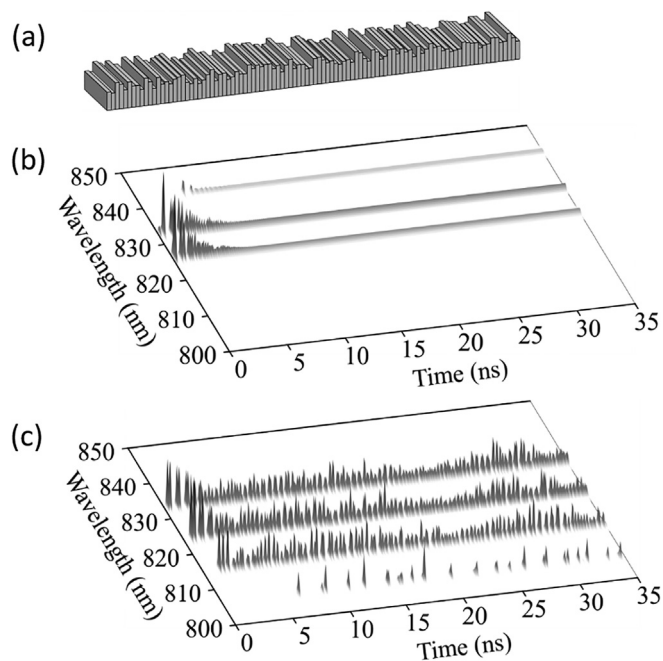


**FIG. 25.** Suppressing laser instability with structural disorder. (a) Schematic of introducing random variation of refractive index to an one-dimensional (1D) laser cavity. (b) Temporal evolutions of three longitudinal lasing modes reveal that they all reach a steady state after transient oscillations. (c) In a homogeneous cavity without refractive index fluctuation, all lasing modes pulsate irregularly and do not stabilize eventually.

wide angle of incidence.[335–337] In nature, structural disorder has been maximized in white beetles scales to acquire an exceptional white appearance.[35,338,339]

Various device applications rely on optical speckle patterns created by random scattering samples and multimode fibers/waveguides. A speckle pattern is sensitive not only to the incident wave but also to the internal structure of a sample and its environment. On one hand, if the sample and its environment remain constant, spatial, spectral, temporal, and polarization information of the illuminating light can be retrieved from the speckle pattern, as described in Secs. III–VII. On the other hand, by fixing the probe light and illumination condition, the speckle pattern may be used to sense the change of a sample or its surrounding. Section IX A will explain how disorder can enhance the sensitivity of optical sensors.

Looking ahead, there are a lot more opportunities to explore disorder for photonic device applications. When light propagates through a static disordered system, the information about incident light field is mixed but not lost. Such mixing of information can be used as a resource for computation, for example, high-dimensional matrix multiplication. In some sense, a strongly scattering medium is an optical realization of a neural network: the connection weights correspond to the coefficients of the field transmission matrix, and the nonlinearity comes from either nonlinear optical response of the material or simply the conversion of light field to intensity during detection by the camera. Section IX B will describe emerging applications of complex random systems for optical computing. Finally, we will briefly discuss the engineering of disorder for photonic device applications in Sec. IX C.

### A. Disorder-enhanced optical sensors

A ground glass optical diffuser has been used to sense the refractive index change of surrounding liquid.[340] When a laser beam of fixed wavelength passes through a solution and illuminates the diffuser, the speckle pattern it generates depends on the refractive index of the solution. A refractive index change as small as 0.00038 is detected with an average error less than 4.5%. Using more diffusers further enhances the sensitivity by multiple scattering of light.[62] With three diffusers immersed in a solution, the solution's refractive index change is detected at resolution of $3.87 \times 10^{-6}$ RIU, which is equivalent to the glucose concentration change of 12 ppm.

Another example is a pressure sensor. Remote sensing of pressure inside deformable microchannels has been realized with light scattering in a translucent Scotch tape.[341] As shown in Fig. 26, a change in the internal pressure of a deformable microchannel distorts the wavefront of a passing laser beam, which is subsequently incident on the Scotch tape and generates speckles in the far field. By detecting the change of speckle pattern, internal pressure can be remotely sensed with the resolution of 0.1 kPa within a pressure range of 0–3 kPa.

Optical speckles generated by multimode fibers have also been used for a variety of environmental sensing applications. In these applications, a laser beam with a constant wavelength is launched into a multimode fiber, and the transmitted/reflected speckles are monitored in time to track changes in the surrounding environment such as temperature,[342] pressure,[343] acoustic vibrations,[344] or properties of a liquid the fiber is immersed in.[345] The speckle patterns can also detect tiny displacements or vibrations of the fiber position.[346–348]

In addition to passive optical sensors, random lasers have been explored as active sensors with enhanced sensitivity.[349] Since random
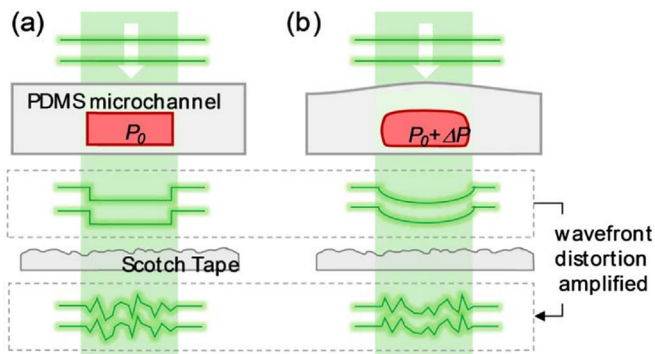
**FIG. 26.** Pressure sensing with laser speckle. Reprinted with permission from Kim *et al.*, Opt. Lett. **41**, 1837 (2016). Copyright 2016 The Optical Society. (a) Schematic diagram describing the change in wavefront of a laser beam, which passes through a transparent channel and a scattering layer (Scotch tape). (b) Deformation of wavefront caused by increase in internal pressure, and the scattering layer amplifies the wavefront change.

lasing action strongly depends on the amount of optical scattering, its emission is used to map cancerous tissue *ex vivo*.[350] A human tissue is infiltrated with a dye solution and optically pumped by a laser. As the strength of light scattering in malignant tissue differs from that of the healthy one, the random lasing emission spectrum is modified. To avoid injection of toxic substance to biological tissue, the laser dye solution is contained in a transparent cell and separated from the scattering tissue.[351] Such design facilitates the application of random laser sensors to *in-vivo* measurements. Alternatively, biocompatible random lasers are made entirely of doped silk, functional in aqueous media.[352] They are capable of probing small changes in a chemical environment due to their intrinsic nonlinear response and spectral purity.

## B. Disorder-assisted optical computing

This subsection will illustrate how disorder can assist optical computing with three examples.

### 1. Random projection

Random projections have been widely used in signal processing and machine learning applications. They require either to store a very large random matrix, or to use a different, structured matrix to reduce the computational and memory costs. This difficulty is recently overcome by using multiple scattering media to perform random projections without having to store any matrix in memory.[353] Experimentally, a monochromatic laser illuminates a digital micromirror device (DMD), which spatially encodes digital information on the light beam by amplitude modulation. The light beam carrying the signal transmits through a layer of titanium dioxide nanoparticles, and the far-field speckle pattern is recorded by a camera. For a stable medium, such as a paint layer on a glass slide, the transmission matrix that maps incident fields to transmitted fields is stable, and thus, the scattering medium can therefore provide a convenient platform for random projections, without the need to determine the field transmission matrix. The resulting random projection of digital data is used for classification, and its efficiency is comparable to that of synthetic random projection.[353] The large dimensional ($10^4$–$10^6$) random projections are obtained almost instantaneously with disordered samples, which can be used for machine learning applications such as kernel classification.

### 2. Reservoir computing

Reservoir computing is a recent computational paradigm based on recurrent neural network. It expands the dimensionality of a problem by mapping an input signal to a higher-dimensional reservoir space, in order to capture and predict complex, non-linear temporal dynamics. Large reservoirs are difficult to obtain in conventional computers, due to extraordinary computation complexity and memory usage. There have been much interest and development of optical reservoir computing.[354,355] One scheme utilizes multiple scattering of light in a disordered system.[356]

In reservoir computing, the most computationally demanding operation is the iterative computation of the reservoir state, which can be accelerated optically with a random scattering medium.[356] The strong optical scattering guarantees random coupling weights of a very large number of photonic nodes and their parallel processing. Even though other steps related to the final linear layer are still performed on a conventional computer, the optical reservoir computing strategy is shown to outperform electronic implementations by two orders of magnitude in speed, and scale to very large dimensions, which cannot be reached in electronics due to memory limitations (Fig. 27). The scalability is demonstrated by predicting multidimensional large chaotic systems using optical reservoirs with up to 50 000 optical nodes.[357]

Multimode fibers/waveguides are also exploited for speckle-based optical reservoir computing.[358] An electro-optical reservoir computer uses speckles generated by propagating a laser beam modulated with a SLM through a multimode waveguide to perform a multivariate audio classification task. Since the feedback and nonlinearity are provided by the SLM and a computer, one optical-to-electrical-to-optical conversion has to be done per pixel per time step. Moreover, such implementation requires as many SLM pixels as the number of neurons. In a latest proposal, the electrical feedback is replaced by optical feedback in a multimode waveguide ring resonator with a built-in nonlinear element.[359] Elimination of the analog-digital conversion and the SLM paves the way toward fast, efficient reservoir computers for optical signal processing.

Expanding from spatial domain, multidimensional speckle dynamics in multimode fibers has been utilized for information processing.[360] The input information is mapped into the space, frequency, and time domains by an optical phase modulation technique. The speckle-based mapping of input information is high dimensional and nonlinear, and thus, nonlinear time-dependent information processing can be achieved at fast rates. Using a reservoir computing approach, chaotic time-series prediction is realized at input rates of 12.5 Gigasamples per second. The passivity of multimode fibers allows multiple tasks to be simultaneously processed, which will further increase the processing speed.

### 3. Reconfigurable operations

Complex optical systems driven by wavefront shaping can perform various operations on classical and quantum light. They are programmable and reconfigurable, leading to promising applications for large-scale classical and quantum circuits.[361–364] From a large field transmission matrix of a complex system, small matrices for desired linear operations have been extracted by finding suitable input and
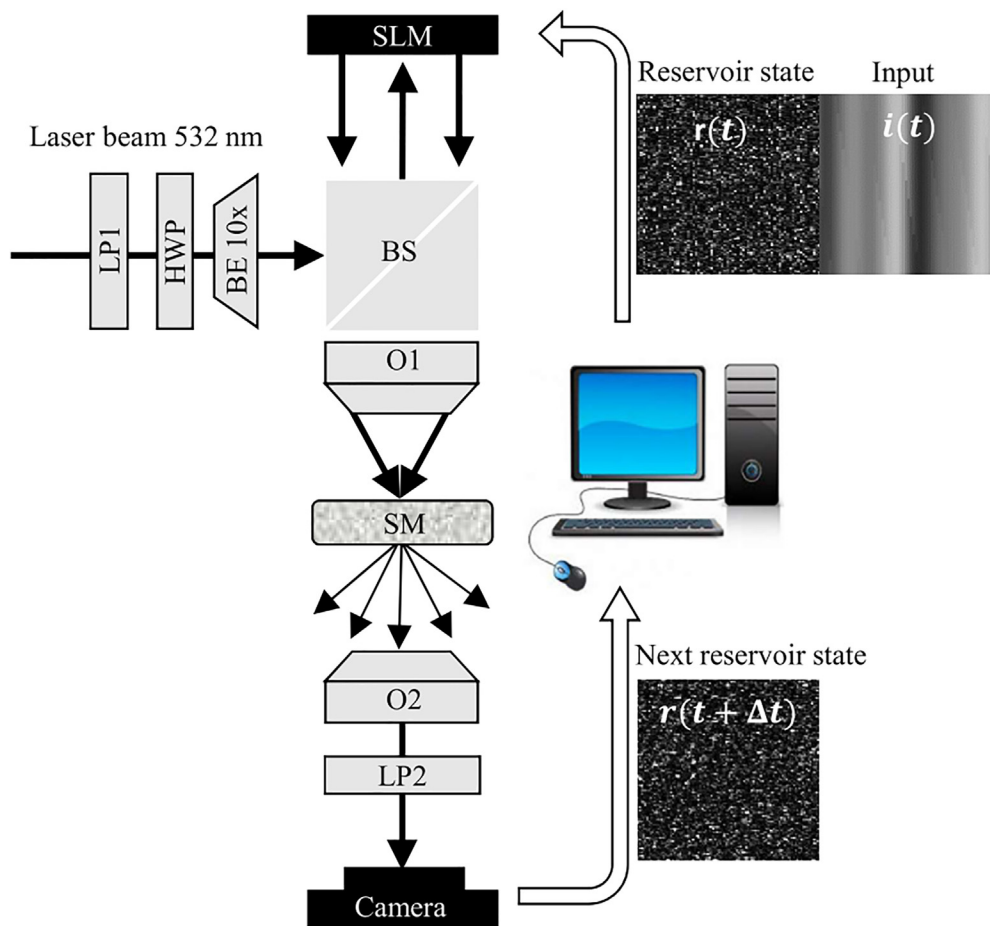
**FIG. 27.** Optical reservoir computing with random scattering medium. Rafayelyan *et al.* Phys. Rev. X **10**, 041037 (2020). Copyright 2020 Author(s); licensed under a Creative Commons Attribution (CC BY) license. The SLM receives from the computer the consequent input concatenated with the reservoir state and imprints it into the spatial phase profile of the reflected beam (upper inset). The scattering medium (SM) provides a complex linear mixing of the whole encoded information. Finally, the camera performs a non-linear readout for the next reservoir state (lower inset), which is sent by the computer back to the SLM to be displayed with new input, and the process repeats.

output projectors.[363] The input projection is carried out by a SLM, which is placed next to a multimode fiber. By displaying a specific pattern on the SLM, the fiber acts as a desired complex-valued linear operator on the optical field. Using different input projections by the SLM, multiple linear operators are constructed with the same fiber. This work offers the prospect of reconfigurable linear optical analog computation units. Extending from classical to quantum regime, the reliable reprogrammable linear transformations open the door to scalable, reconfigurable quantum circuits.[364]

Beyond the passive random systems, random lasers with extraordinary complexity and strong nonlinearity may be suitable for reservoir computing. The spatiotemporal interference of numerous lasing modes in disordered media can be a source of massive-parallel random number generation.[365]

### C. Engineering disorder

Moving beyond harvesting disorder is engineering disorder for photonic devices.[34,35] Instead of complete disorder, incorporating short-range or long-range order to nanostructures may further enhance device performance. It has been shown that introducing spatial correlations to disordered structures improves photon management and efficiency of thin-film solar cells.[366–369] Specially designed disordered structures[199,370] and metasurface diffusers[371] not only minimize energy loss and eliminate laborious calibration procedures, but also provide large noise tolerance, reliable reproducibility, and robustness against misalignment. In nature, amorphous photonic structures with short-range order[372] are widely adopted to produce angle-invariant color,[373,374] in contrast to iridescent color created by ordered structures. Bioinspired photonic structures with correlated disorder[36] or hyperuniformity[34] are fabricated and explored for various applications, for example, special coloration effects[35,375,376] and thin photovoltaic absorbers.[377] Compared to random lasers, employing deterministic aperiodic nanostructures[378] leads to control and reproducibility of lasing mode frequencies and spatial profiles.[379] In between order and disorder, there is a huge parameter space to explore for photonic device applications.

# NOMENCLATURE

## Symbol

| | |
|---|---|
| $a_m$ | Modal complex amplitude |
| $A(t)$ | Time resolved amplitude |
| $A(\omega)$ | Spectral amplitude |
| $C_E$ | Spectral field correlation function |
| $C_i$ | Cross-correlation coefficients of $R_s$ with $i = \{x, y, xy, +\}$ polarized references |
| $C_I$ | Spectral intensity correlation function |
| $C_S$ | Spectral correlation function |
| $C_t$ | Transmitted speckle intensity contrast |
| $C_t$ | Speckle contrast |
| $D_a$ | Input aperture diameter |
| $D_w$ | Fiber core diameter |
| DOF | Depth of field |
| $\mathbf{E}_{\text{in}}$ | Random lens input field |
| $\mathbf{E}_{\text{in}}^H$ | Horizontally polarized input field |
| $\mathbf{E}_{\text{in}}^V$ | Vertically polarized input field |
| $E_{\text{MMF}}$ | Multi-mode fiber output field |
| $\mathbf{E}_{\text{out}}$ | Random lens output field |
| $\mathbf{E}_{\text{out}}^H$ | Horizontally polarized output field |
| $\mathbf{E}_{\text{out}}^V$ | Vertically polarized output field |
| $E_p$ | Speckle field pattern |
| $E_s(\mathbf{r}, t)$ | Spatiotemporal speckle field |
| $E_t(\mathbf{r}, t)$ | Transmitted spatiotemporal electric field |
| $E(t)$ | Time resolved electric field |
| $E(\omega)$ | Spectral field |
| $\mathscr{F}$ | Fourier transform |
| $f$ | Lens focal point |
| FOV | Field of view |
| FSR | Free spectral range |
| $f(t)$ | Laser pulse field |
| $F(\omega)$ | Laser pulse field spectrum |
| $g(t)$ | Transmitted/reflected laser pulse |
| $G(\omega)$ | Transmitted/reflected pulse field spectrum |
| $I$ | Total intensity |
| $I_{\text{det}}$ | Detector measured intensity |
| $I_{\text{dif}}$ | Sensor array spectral intensity distribution |
| $\mathbf{I}_{\text{in}}$ | Input intensity |
| $I_{\text{MMF}}$ | Multi-mode fiber output intensity |
| $\mathbf{I}_{\text{out}}$ | Output intensity |
| $I_p$ | Integrated intensity of speckle and reflected/transmitted pulses interference |
| $I_q$ | Extracted intensity term of speckle and reflected/transmitted pulses interference |
| $I_{\text{sig}}$ | Input spectral signal |
| $\overline{I_s}$ | Average speckle intensity |
| $I_{\text{sig}}^{(H)}$ | Input spectra for TE polarization |
| $I_{\text{sig}}^{(V)}$ | Input spectra for TM polarization |
| $I_{1p}$ | One photon absorption time integrated intensity pattern |
| $I_{2p}$ | Two-photon absorption time integrated intensity pattern |
| $I_\lambda$ | Multi-spectral intensity |
| $I(\omega)$ | Power spectrum |
| $L$ | Linear dimension of a spectrometer system |
| $\mathscr{L}$ | Scattering path length distribution |
| $L_{\text{MMF}}$ | Multi-mode fiber length |
| $\langle\mathscr{L}\rangle$ | Average scattering path length |
| $l_t$ | Scattering mean free path |
| $l_s$ | Transport mean free path |
| $L_s$ | Scattering system thickness |
| $L_w$ | Fiber length |
| $\Delta\mathscr{L}$ | Scattering path length distribution width |
| $m$ | magnification ratio |
| $\mathbf{M}_{\text{F}}$ | Random lens field transmission matrix |
| $M_w$ | Number of guided modes |
| $\mathbf{M}_{HH}$ | Horizontal to Horizontal polarization scattering matrix |
| $\mathbf{M}_{HV}$ | Horizontal to Vertical polarization scattering matrix |
| $\mathbf{M}_{VH}$ | Vertical to Horizontal polarization scattering matrix |
| $\mathbf{M}_{VV}$ | Vertical to Vertical polarization scattering matrix |
| $N_\lambda$ | Number of distinct incoherent speckle patterns |
| NA | Numerical aperture |
| $N_i$ | Number of input channels |
| $N_{\text{in}}$ | Number of input polarization states |
| $N_o$ | Number of output channels |
| $N_{\text{out}}$ | Number of input polarization states |
| $N_r$ | Number of uncorrelated speckle patterns |
| $N_x, N_{x,y}$ | Number of spatial independent channels |
| $N_\lambda$ | Number of spectral channels |
| $O$ | Sum of point sources |
| $O_\lambda$ | Multi-spectral object |
| $P$ | Point spread function (PSF) |
| $P_H$ | TE polarization spectral PSF |
| $P_V$ | TM polarization spectral PSF |
| $P_\lambda$ | Multi-spectral point spread function |
| $r$ | Spatial radial coordinate |
| $R_s$ | Correlated speckle pattern |
| $R_x$ | Reference speckle pattern with x-axis linear polarization |
| $R_{xy}$ | Reference speckle pattern with 45° linear polarization |
| $R_y$ | Reference speckle pattern with y-axis linear polarization |
| $R_+$ | Reference speckle pattern with right-handed circular polarization |
| RES | Lateral resolution |
| $\mathbf{S}$ | Stokes vector |
| $\mathbf{S}_{\text{in}}$ | Input Stokes vector |
| $S_1, \ldots, S_4$ | Stokes parameters |
| SNR | Signal-to-noise ratio |
| $T(\mathbf{r}, \omega)$ | Frequency resolved field transmission matrix |
| $\Delta t$ | Temporal range |
| $\delta t$ | Temporal resolution |
| $\Theta(t)$ | Time resolved phase |
| $\theta_{TM}(\mathbf{r}, \omega)$ | Transmission matrix spectral phase |
| $x$ | Cartesian spatial coordinate x |
| $y$ | Cartesian spatial coordinate y |
| $z$ | Point source axial coordinate |
| $z'$ | Sensor axial coordinate |
| $z_{det}$ | Axial lens to detector distance |
| $z_{obj}$ | Axial object to lens distance |
| $z_{ref}$ | Axial reference source to lens distance |
| $\beta_m$ | Modal propagation constant |

| $\dot{\beta}_m$ | Time derivative of modal propagation constant |
|---|---|
| $\Delta\theta_m$ | Angular range of the memory effect |
| $\Delta\lambda$ | Wavelength spacing |
| $\delta$ | Dirac delta distribution |
| $\delta\lambda$ | Spectral resolution |
| $\delta\omega$ | lasing modes frequency spacing |
| $\Theta(t)$ | Time resolved phase |
| $\theta_{max}$ | Maximum angular range of light |
| $\theta_s$ | Scattering angle |
| $\theta_T$ | original input angle of light |
| $\theta(\omega)$ | Spectral phase |
| $\theta_{TM}(\mathbf{r}, \omega)$ | Transmission matrix spectral phase |
| $\lambda$ | Wavelength |
| $\rho$ | Point source radial coordinate |
| $\rho_0$ | Reference point source transverse coordinate |
| $\rho'$ | Sensor radial coordinate |
| $\sigma_I$ | Speckle intensity standard deviation |
| $\phi$ | Azimuthal coordinate |
| $\Psi$ | Mode spatial field profile |
| $\omega$ | Angular frequency |
| $*$ | Convolution operation |
| $\star$ | Correlation operation |
| $\circledast$ | Deconvolution operator |

## Unit Description

| as | attoseconds |
|---|---|
| cm | centimeters |
| dBm | decibel-milliwatts |
| fs | femtoseconds |
| GHz | Gigahertz |
| GSps | Giga samples per second |
| Hz | Hertz ($s^{-1}$) |
| kPa | Kilopascal |
| m | meters |
| MHz | Megahertz |
| mm | millimeters |
| MSps | Mega samples per second |
| nm | nanometers |
| ns | nanoseconds |
| pm | pedometers |
| ppm | Parts per million |
| ps | picoseconds |
| RIU | Refractive index unit |
| THz | Terahertz |
| $\circ$ | Angular degree |
| $\mu$m | micrometers |

## AUTHOR DECLARATIONS
### Conflict of Interest

The authors have no conflict of interest to declare.

### DATA AVAILABILITY

Data sharing is not applicable to this article as no new data were created or analyzed in this study.

## REFERENCES

[1] S. Molesky, Z. Lin, A. Y. Piggott, W. Jin, J. Vucković, and A. W. Rodriguez, "Inverse design in nanophotonics," Nat. Photonics **12**, 659–670 (2018).

[2] R. Pappu, B. Recht, J. Taylor, and N. Gershenfeld, "Physical one-way functions," Science **297**, 2026–2030 (2002).

[3] H. Cao, "Perspective on speckle spectrometers," J. Opt. **19**, 060402 (2017).

[4] E. Small, O. Katz, Y. Guan, and Y. Silberberg, "Spectral control of broadband light through random media by wavefront shaping," Opt. Lett. **37**, 3429–3431 (2012).

[5] L. Wan, X. Ji, R. K. Singh, Z. Chen, and J. Pu, "Use of scattering layer as a programmable spectrum filter," IEEE J. Quantum Electron. **55**, 1–6 (2019).

[6] J.-H. Park, C. Park, H. Yu, Y.-H. Cho, and Y. Park, "Dynamic active wave plate using random nanoparticles," Opt. Express **20**, 17010–17016 (2012).

[7] Y. Guan, O. Katz, E. Small, J. Zhou, and Y. Silberberg, "Polarization control of multiply scattered light through random media by wavefront shaping," Opt. Lett. **37**, 4663–4665 (2012).

[8] W. Xiong, C. W. Hsu, Y. Bromberg, J. E. Antonio-Lopez, R. A. Correa, and H. Cao, "Complete polarization control in multimode fibers with polarization and mode coupling," Light: Sci. Appl. **7**, 1–10 (2018).

[9] O. Katz, E. Small, Y. Bromberg, and Y. Silberberg, "Focusing and compression of ultrashort pulses through scattering media," Nat. Photonics **5**, 372–377 (2011).

[10] D. J. McCabe, A. Tajalli, D. R. Austin, P. Bondareff, I. A. Walmsley, S. Gigan, and B. Chatel, "Spatio-temporal focusing of an ultrafast pulse through a multiply scattering medium," Nat. Commun. **2**, 447 (2011).

[11] J. Aulbach, B. Gjonaj, P. M. Johnson, A. P. Mosk, and A. Lagendijk, "Control of light transmission through opaque scattering media in space and time," Phys. Rev. Lett. **106**, 103901 (2011).

[12] Z. Shi, M. Davy, J. Wang, and A. Z. Genack, "Focusing through random media in space and time: A transmission matrix approach," Opt. Lett. **38**, 2714–2716 (2013).

[13] E. E. Morales-Delgado, S. Farahi, I. N. Papadopoulos, D. Psaltis, and C. Moser, "Delivery of focused short pulses through a multimode fiber," Opt. Express **23**, 9109–9120 (2015).

[14] J. Carpenter, B. J. Eggleton, and J. Schröder, "Observation of Eisenbud–Wigner–Smith states as principal modes in multimode fibre," Nat. Photonics **9**, 751–757 (2015).

[15] W. Xiong, P. Ambichl, Y. Bromberg, B. Redding, S. Rotter, and H. Cao, "Spatiotemporal control of light transmission through a multimode fiber with strong mode coupling," Phys. Rev. Lett. **117**, 053901 (2016).

[16] M. Mounaix, D. Andreoli, H. Defienne, G. Volpe, O. Katz, S. Grésillon, and S. Gigan, "Spatiotemporal coherent control of light through a multiple scattering medium with the multispectral transmission matrix," Phys. Rev. Lett. **116**, 253901 (2016).

[17] A. P. Mosk, A. Lagendijk, G. Lerosey, and M. Fink, "Controlling waves in space and time for imaging and focusing in complex media," Nat. Photonics **6**, 283 (2012).

[18] S. R. Huisman, T. J. Huisman, S. A. Goorden, A. P. Mosk, and P. W. Pinkse, "Programming balanced optical beam splitters in white paint," Opt. Express **22**, 8320–8332 (2014).

[19] A. Lagendijk and B. A. Van Tiggelen, "Resonant multiple scattering of light," Phys. Rep. **270**, 143–215 (1996).

[20] C. W. Beenakker, "Random-matrix theory of quantum transport," Rev. Mod. Phys. **69**, 731 (1997).

[21] M. v van Rossum and T. M. Nieuwenhuizen, "Multiple scattering of classical waves: Microscopy, mesoscopy, and diffusion," Rev. Mod. Phys. **71**, 313 (1999).

[22]E. Akkermans and G. Montambaux, *Mesoscopic Physics of Electrons and Photons* (Cambridge University Press, 2007).

[23]Z. Shi, M. Davy, and A. Z. Genack, "Statistics and control of waves in disordered media," Opt. Express **23**, 12293–12320 (2015).

[24]A. Dogariu and R. Carminati, "Electromagnetic field correlations in three-dimensional speckles," Phys. Rep. **559**, 1–29 (2015).

[25]R. Carminati and J. C. Schotland, *Principles of Scattering and Transport of Light* (Cambridge University Press, 2021).

[26]I. M. Vellekoop, "Feedback-based wavefront shaping," Opt. Express **23**, 12189–12206 (2015).

[27]S. Rotter and S. Gigan, "Light fields in complex media: Mesoscopic scattering meets wave control," Rev. Mod. Phys. **89**, 015005 (2017).

[28]R. Horstmeyer, H. Ruan, and C. Yang, "Guidestar-assisted wavefront-shaping methods for focusing light into biological tissue," Nat. Photonics **9**, 563–571 (2015).

[29]M. Kim, W. Choi, Y. Choi, C. Yoon, and W. Choi, "Transmission matrix of a scattering medium and its applications in biophotonics," Opt. Express **23**, 12648–12668 (2015).

[30]H. Yu, J. Park, K. Lee, J. Yoon, K. Kim, S. Lee, and Y. Park, "Recent advances in wavefront shaping techniques for biomedical applications," Curr. Appl. Phys. **15**, 632–641 (2015).

[31]S. Yoon, M. Kim, M. Jang, Y. Choi, W. Choi, S. Kang, and W. Choi, "Deep optical imaging within complex scattering media," Nat. Rev. Phys. **2**, 141–158 (2020).

[32]D. S. Wiersma, "Disordered photonics," Nat. Photonics **7**, 188–196 (2013).

[33]J.-H. Park, J. Park, K. Lee, and Y. Park, "Disordered optics: Exploiting multiple light scattering and wavefront shaping for nonconventional optical elements," Adv. Mater. **32**, 1903457 (2020).

[34]S. Yu, C.-W. Qiu, Y. Chong, S. Torquato, and N. Park, "Engineered disorder in photonics," Nat. Rev. Mater. **6**, 226–243 (2021).

[35]M. Rothammer, C. Zollfrank, K. Busch, and G. von Freymann, "Tailored disorder in photonics: Learning from nature," Adv. Opt. Mater. **9**, 2100787 (2021).

[36]K. Vynck, R. Pierrat, R. Carminati, L. S. Froufe-Pérez, F. Scheffold, R. Sapienza, S. Vignolini, and J. J. Sáenz, "Light in correlated disordered media," arXiv:2106.13892 (2021).

[37]B. Javidi, A. Carnicer, M. Yamaguchi, T. Nomura, E. Pérez-Cabré, M. S. Millán, N. K. Nishchal, R. Torroba, J. F. Barrera, W. He *et al.*, "Roadmap on optical security," J. Opt. **18**, 083001 (2016).

[38]Y. Gao, S. F. Al-Sarawi, and D. Abbott, "Physical unclonable functions," Nat. Electron. **3**, 81–91 (2020).

[39]F. Pavanello, I. O'Connor, U. Rührmair, A. C. Foster, and D. Syvridis, "Recent advances in photonic physical unclonable functions," in *2021 IEEE European Test Symposium (ETS)* (IEEE, 2021), pp. 1–10.

[40]J. Goodman, *Speckle Phenomena in Optics: Theory and Applications* (Roberts & Company, 2007).

[41]U. Rührmair, C. Hilgers, S. Urban, A. Weiershäuser, E. Dinter, B. Forster, and C. Jirauschek, "Optical PUFS reloaded," Report No. 2013/215 (2013).

[42]B. R. Anderson, R. Gunawidjaja, and H. Eilers, "Initial tamper tests of novel tamper-indicating optical physical unclonable functions," Appl. Opt. **56**, 2863–2872 (2017).

[43]B. Skoric, G.-J. Schrijen, W. Ophey, R. Wolters, N. Verhaegh, and J. van Geloven, "Experimental hardware for coating PUFS and optical PUFS," in *Security with Noisy Data* (Springer, 2007), pp. 255–268.

[44]M. Vai, B. Nahill, J. Kramer, M. Geis, D. Utin, D. Whelihan, and R. Khazan, "Secure architecture for embedded systems," in *2015 IEEE High Performance Extreme Computing Conference (HPEC)* (IEEE, 2015), pp. 1–5.

[45]K. Kursawe, A.-R. Sadeghi, D. Schellekens, B. Skoric, and P. Tuyls, "Reconfigurable physical unclonable functions-enabling technology for tamper-resistant storage," in *2009 IEEE International Workshop on Hardware-Oriented Security and Trust* (IEEE, 2009), pp. 22–29.

[46]R. Horstmeyer, S. Assawaworrarit, U. Ruhrmair, and C. Yang, "Physically secure and fully reconfigurable data storage using optical scattering," in *2015 IEEE International Symposium on Hardware Oriented Security and Trust (HOST)* (IEEE, 2015), pp. 157–162.

[47]B. C. Grubel, B. T. Bosworth, M. R. Kossey, H. Sun, A. B. Cooper, M. A. Foster, and A. C. Foster, "Silicon photonic physical unclonable function," Opt. Express **25**, 12710–12721 (2017).

[48]B. T. Bosworth, I. A. Atakhodjaev, M. R. Kossey, B. C. Grubel, D. S. Vresilovic, J. R. Stroud, N. MacFarlane, J. Villalba, N. Dehak, A. B. Cooper *et al.*, "Unclonable photonic keys hardened against machine learning attacks," APL Photonics **5**, 010803 (2020).

[49]S. A. Goorden, M. Horstmann, A. P. Mosk, B. Škorić, and P. W. Pinkse, "Quantum-secure authentication of a physical unclonable key," Optica **1**, 421–424 (2014).

[50]B. Škorić, A. P. Mosk, and P. W. Pinkse, "Security of quantum-readout PUFS against quadrature-based challenge-estimation attacks," Int. J. Quantum Inf. **11**, 1350041 (2013).

[51]M. Geis, K. Gettings, and M. Vai, "Optical physical unclonable function," in *2017 IEEE 60th International Midwest Symposium on Circuits and Systems (MWSCAS)* (IEEE, 2017), pp. 1248–1251.

[52]C. Mesaritakis, M. Akriotou, A. Kapsalis, E. Grivas, C. Chaintoutis, T. Nikas, and D. Syvridis, "Physical unclonable function based on a multi-mode optical waveguide," Sci. Rep. **8**, 9653 (2018).

[53]Y. Bromberg, B. Redding, S. M. Popoff, N. Zhao, G. Li, and H. Cao, "Remote key establishment by random mode mixing in multimode fibers and optical reciprocity," Opt. Eng. **58**, 016105 (2019).

[54]L. V. Amitonova, T. B. Tentrup, I. M. Vellekoop, and P. W. Pinkse, "Quantum key establishment via a multimode fiber," Opt. Express **28**, 5965–5981 (2020).

[55]F. B. Tarik, A. Famili, Y. Lao, and J. D. Ryckman, "Robust optical physical unclonable function using disordered photonic integrated circuits," Nanophotonics **9**, 2817–2828 (2020).

[56]F. Chen, Q. Li, M. Li, F. Huang, H. Zhang, J. Kang, and P. Wang, "Unclonable fluorescence behaviors of perovskite quantum dots/chaotic metasurfaces hybrid nanostructures for versatile security primitive," Chem. Eng. J. **411**, 128350 (2021).

[57]A. Fratalocchi, A. Fleming, C. Conti, and A. D. Falco, "NIST-certified secure key generation via deep learning of physical unclonable functions in silica aerogels," Nanophotonics **10**, 457–464 (2021).

[58]B. Škorić, P. W. Pinkse, and A. P. Mosk, "Authenticated communication from quantum readout of PUFs," Quantum Inf. Process. **16**, 200 (2017).

[59]R. Horstmeyer, B. Judkewitz, I. M. Vellekoop, S. Assawaworrarit, and C. Yang, "Physical key-protected one-time pad," Sci. Rep. **3**, 3543 (2013).

[60]B. C. Grubel, B. T. Bosworth, M. R. Kossey, A. B. Cooper, M. A. Foster, and A. C. Foster, "Secure communications using nonlinear silicon photonic keys," Opt. Express **26**, 4710–4722 (2018).

[61]R. Uppu, T. A. Wolterink, S. A. Goorden, B. Chen, B. Škorić, A. P. Mosk, and P. W. Pinkse, "Asymmetric cryptography with physical unclonable keys," Quantum Sci. Technol. **4**, 045011 (2019).

[62]V. Tran, S. K. Sahoo, D. Wang, and C. Dang, "Utilizing multiple scattering effect for highly sensitive optical refractive index sensing," Sens. Actuators A **301**, 111776 (2020).

[63]U. Rührmair and D. E. Holcomb, "PUFS at a glance," in *2014 Design, Automation Test in Europe Conference Exhibition (DATE)* (IEEE, 2014), pp. 1–6.

[64]U. Rührmair, S. Devadas, and F. Koushanfar, "Security based on physical unclonability and disorder," in *Introduction to Hardware Security and Trust*, edited by M. Tehranipoor and C. Wang (Springer, New York, 2012), pp. 65–102.

[65]U. Rührmair, "Secret-free security: A survey and tutorial," J. Cryptographic Eng. (to be published) (2022).

[66]J. D. Buchanan, R. P. Cowburn, A.-V. Jausovec, D. Petit, P. Seem, G. Xiong, D. Atkinson, K. Fenton, D. A. Allwood, and M. T. Bryan, "'Fingerprinting' documents and packaging," Nature **436**, 475–475 (2005).

[67]Y. Blau, O. Bar-On, O. Kotlicki, Y. Hanein, A. Boag, and J. Scheuer, "Holographic anti-counterfeiting tags utilizing speckle pattern 'fingerprint,'" in *Novel Optical Materials and Applications* (Optical Society of America, 2018), pp. NoW1D-1.

[68]Y. Blau, O. Bar-On, Y. Hanein, A. Boag, and J. Scheuer, "Holographic speckle-based authentication paradigm," in *CLEO: Applications and Technology* (Optical Society of America, 2019), pp. AF3K–2.

[69]A. F. Smith, P. Patton, and S. E. Skrabalak, "Plasmonic nanoparticles as a physically unclonable function for responsive anti-counterfeit nanofingerprints," Adv. Funct. Mater. **26**, 1315–1321 (2016).

[70]H. Zhang and S. Tzortzakis, "Robust authentication through stochastic femto-second laser filament induced scattering surfaces," Appl. Phys. Lett. **108**, 211107 (2016).

[71]M. R. Carro-Temboury, R. Arppe, T. Vosch, and T. J. Sørensen, "An optical authentication system based on imaging of excitation-selected lanthanide luminescence," Sci. Adv. **4**, e1701384 (2018).

[72]J. Feng, W. Wen, X. Wei, X. Jiang, M. Cao, X. Wang, X. Zhang, L. Jiang, and Y. Wu, "Random organic nanolaser arrays for cryptographic primitives," Adv. Mater. **31**, 1807880 (2019).

[73]J. W. Leem, M. S. Kim, S. H. Choi, S.-R. Kim, S.-W. Kim, Y. M. Song, R. J. Young, and Y. L. Kim, "Edible unclonable functions," Nat. Commun. **11**, 328 (2020).

[74]R. Fergus, A. Torralba, and W. T. Freeman, "Random lens imaging," Technical Report MIT-CSAIL-TR-2006-058 (2006).

[75]I. M. Vellekoop, A. Lagendijk, and A. Mosk, "Exploiting disorder for perfect focusing," Nat. Photonics **4**, 320–322 (2010).

[76]Y. Choi, T. D. Yang, C. Fang-Yen, P. Kang, K. J. Lee, R. R. Dasari, M. S. Feld, and W. Choi, "Overcoming the diffraction limit using multiple light scattering in a highly disordered medium," Phys. Rev. Lett. **107**, 023902 (2011).

[77]Y. Choi, C. Yoon, M. Kim, W. Choi, and W. Choi, "Optical imaging with the use of a scattering lens," IEEE J. Sel. Top. Quantum Electron. **20**, 61–73 (2013).

[78]N. Antipa, G. Kuo, R. Heckel, B. Mildenhall, E. Bostan, R. Ng, and L. Waller, "Diffusercam: Lensless single-exposure 3D imaging," Optica **5**, 1–9 (2018).

[79]P. Potuluri, M. Xu, and D. J. Brady, "Imaging with random 3D reference structures," Opt. Express **11**, 2134–2141 (2003).

[80]S. Popoff, G. Lerosey, M. Fink, A. C. Boccara, and S. Gigan, "Image transmission through an opaque material," Nat. Commun. **1**, 81 (2010).

[81]A. Liutkus, D. Martina, S. Popoff, G. Chardon, O. Katz, G. Lerosey, S. Gigan, L. Daudet, and I. Carron, "Imaging with nature: Compressive imaging using a multiply scattering medium," Sci. Rep. **4**, 5552 (2014).

[82]C. Park, J.-H. Park, C. Rodriguez, H. Yu, M. Kim, K. Jin, S. Han, J. Shin, S. H. Ko, K. T. Nam *et al.*, "Full-field subwavelength imaging using a scattering superlens," Phys. Rev. Lett. **113**, 113901 (2014).

[83]Z. Zhang, P. Isola, and E. H. Adelson, "Sparklevision: Seeing the world through random specular microfacets," in *Proceedings of the IEEE Conference on Computer Vision and Pattern Recognition Workshops* (IEEE, 2015), pp. 1–9.

[84]A. Stylianou and R. Pless, "Sparklegeometry: Glitter imaging for 3d point tracking," in *Proceedings of the IEEE Conference on Computer Vision and Pattern Recognition Workshops* (IEEE, 2016), pp. 10–17.

[85]S. Feng, C. Kane, P. A. Lee, and A. D. Stone, "Correlations and fluctuations of coherent wave transmission through disordered media," Phys. Rev. Lett. **61**, 834 (1988).

[86]I. Freund, M. Rosenbluh, and S. Feng, "Memory effects in propagation of optical waves through disordered media," Phys. Rev. Lett. **61**, 2328 (1988).

[87]S. Li, M. Deng, J. Lee, A. Sinha, and G. Barbastathis, "Imaging through glass diffusers using densely connected convolutional networks," Optica **5**, 803–813 (2018).

[88]Y. Li, Y. Xue, and L. Tian, "Deep speckle correlation: A deep learning approach toward scalable imaging through scattering media," Optica **5**, 1181–1190 (2018).

[89]A. Turpin, I. Vishniakou, and J. d. Seelig, "Light scattering control in transmission and reflection with neural networks," Opt. Express **26**, 30911–30929 (2018).

[90]M. Lyu, H. Wang, G. Li, S. Zheng, and G. Situ, "Learning-based lensless imaging through optically thick scattering media," Adv. Photonics **1**, 036002 (2019).

[91]M. Yang, Z.-H. Liu, Z.-D. Cheng, J.-S. Xu, C.-F. Li, and G.-C. Guo, "Deep hybrid scattering image learning," J. Phys. D: Appl. Phys. **52**, 115105 (2019).

[92]S. Cheng, H. Li, Y. Luo, Y. Zheng, and P. Lai, "Artificial intelligence-assisted light control and computational imaging through scattering media," J. Innovative Opt. Health Sci. **12**, 1930006 (2019).

[93]W. Tang, J. Yang, W. Yi, Q. Nie, J. Zhu, M. Zhu, Y. Guo, M. Li, X. Li, and W. Wang, "Single-shot coherent power-spectrum imaging of objects hidden by opaque scattering media," Appl. Opt. **58**, 1033–1039 (2019).

[94]E. Guo, S. Zhu, Y. Sun, L. Bai, C. Zuo, and J. Han, "Learning-based method to reconstruct complex targets through scattering medium beyond the memory effect," Opt. Express **28**, 2433–2446 (2020).

[95]L. Sun, J. Shi, X. Wu, Y. Sun, and G. Zeng, "Photon-limited imaging through scattering medium based on deep learning," Opt. Express **27**, 33120–33134 (2019).

[96]Y. Li, S. Cheng, Y. Xue, and L. Tian, "Displacement-agnostic coherent imaging through scatter with an interpretable deep neural network," Opt. Express **29**, 2244–2257 (2021).

[97]I. Freund, "Correlation imaging through multiply scattering media," Phys. Lett. A **147**, 502–506 (1990).

[98]I. Freund, "Looking through walls and around corners," Physica A **168**, 49–65 (1990).

[99]A. K. Singh, G. Pedrini, M. Takeda, and W. Osten, "Scatter-plate microscope for lensless microscopy with diffraction limited resolution," Sci. Rep. **7**, 10687 (2017).

[100]J. Bertolotti, E. G. Van Putten, C. Blum, A. Lagendijk, W. L. Vos, and A. P. Mosk, "Non-invasive imaging through opaque scattering layers," Nature **491**, 232–234 (2012).

[101]O. Katz, P. Heidmann, M. Fink, and S. Gigan, "Non-invasive single-shot imaging through scattering layers and around corners via speckle correlations," Nat. Photonics **8**, 784–790 (2014).

[102]J. Bertolotti, E. Van Putten, C. Blum, A. Lagendijk, W. Vos, and A. Mosk, "Non-invasive imaging through opaque scattering layers," Proc. SPIE **9335**, 93350W (2015).

[103]A. K. Singh, D. N. Naik, G. Pedrini, M. Takeda, and W. Osten, "Exploiting scattering media for exploring 3D objects," Light: Sci. Appl. **6**, e16219 (2017).

[104]F. Zhang, G. Pedrini, and W. Osten, "Phase retrieval of arbitrary complex-valued fields through aperture-plane modulation," Phys. Rev. A **75**, 043805 (2007).

[105]A. Anand, G. Pedrini, W. Osten, and P. Almoro, "Wavefront sensing with random amplitude mask and phase retrieval," Opt. Lett. **32**, 1584–1586 (2007).

[106]P. F. Almoro and S. G. Hanson, "Random phase plate for wavefront sensing via phase retrieval and a volume speckle field," Appl. Opt. **47**, 2979–2987 (2008).

[107]S. Bernet, W. Harm, A. Jesacher, and M. Ritsch-Marte, "Lensless digital holography with diffuse illumination through a pseudo-random phase mask," Opt. Express **19**, 25113–25124 (2011).

[108]R. Horisaki, Y. Ogura, M. Aino, and J. Tanida, "Single-shot phase imaging with a coded aperture," Opt. Lett. **39**, 6466–6469 (2014).

[109]R. Horisaki, R. Egami, and J. Tanida, "Experimental demonstration of single-shot phase imaging with a coded aperture," Opt. Express **23**, 28691–28697 (2015).

[110]R. Horisaki and J. Tanida, "Multidimensional object acquisition by single-shot phase imaging with a coded aperture," Opt. Express **23**, 9696–9704 (2015).

[111]K. Lee and Y. Park, "Exploiting the speckle-correlation scattering matrix for a compact reference-free holographic image sensor," Nat. Commun. **7**, 13359 (2016).

[112]Y. Baek, K. Lee, J. Oh, and Y. Park, "Speckle-correlation scattering matrix approaches for imaging and sensing through turbidity," Sensors **20**, 3147 (2020).

[113]Y. Baek, K. Lee, and Y. Park, "High-resolution holographic microscopy exploiting speckle-correlation scattering matrix," Phys. Rev. Appl. **10**, 024053 (2018).

[114]P. Berto, H. Rigneault, and M. Guillon, "Wavefront sensing with a thin diffuser," Opt. Lett. **42**, 5117–5120 (2017).

[115]K. Kim, H. Yu, K. Lee, and Y. Park, "Universal sensitivity of speckle intensity correlations to wavefront change in light diffusers," Sci. Rep. **7**, 44435 (2017).

[116]I. M. Vellekoop and A. Mosk, "Focusing coherent light through opaque strongly scattering media," Opt. Lett. **32**, 2309–2311 (2007).

[117]Z. Yaqoob, D. Psaltis, M. S. Feld, and C. Yang, "Optical phase conjugation for turbidity suppression in biological samples," Nat. Photonics **2**, 110–115 (2008).

[118]D. D. Battista, G. Zacharakis, and M. Leonetti, "Enhanced adaptive focusing through semi-transparent media," Sci. Rep. **5**, 17406 (2015).

[119] E. G. van Putten, D. Akbulut, J. Bertolotti, W. L. Vos, A. Lagendijk, and A. Mosk, "Scattering lens resolves sub-100 nm structures with visible light," Phys. Rev. Lett. **106**, 193905 (2011).

[120] J.-H. Park, C. Park, H. Yu, J. Park, S. Han, J. Shin, S. H. Ko, K. T. Nam, Y.-H. Cho, and Y. Park, "Subwavelength light focusing using random nanoparticles," Nat. Photonics **7**, 454–458 (2013).

[121] S. Popoff, G. Lerosey, R. Carminati, M. Fink, A. Boccara, and S. Gigan, "Measuring the transmission matrix in optics: An approach to the study and control of light propagation in disordered media," Phys. Rev. Lett. **104**, 100601 (2010).

[122] B. Mastiani, T.-L. Ohn, and I. M. Vellekoop, "Scanning a focus through scattering media without using the optical memory effect," Opt. Lett. **44**, 5226–5229 (2019).

[123] D. D. Battista, D. Ancora, H. Zhang, K. Lemonaki, E. Marakis, E. Liapis, S. Tzortzakis, and G. Zacharakis, "Tailored light sheets through opaque cylindrical lenses," Optica **3**, 1237–1240 (2016).

[124] M. Jang, Y. Horie, A. Shibukawa, J. Brake, Y. Liu, S. M. Kamali, A. Arbabi, H. Ruan, A. Faraon, and C. Yang, "Wavefront shaping with disorder-engineered metasurfaces," Nat. Photonics **12**, 84–90 (2018).

[125] A. Boniface, M. Mounaix, B. Blochet, R. Piestun, and S. Gigan, "Transmission-matrix-based point-spread-function engineering through a complex medium," Optica **4**, 54–59 (2017).

[126] E. Seo, J. Ahn, W. Choi, H. Lee, Y. M. Jhon, S. Lee, and W. Choi, "Far-field control of focusing plasmonic waves through disordered nanoholes," Opt. Lett. **39**, 5838–5841 (2014).

[127] B. Gjonaj, J. Aulbach, P. Johnson, A. Mosk, L. Kuipers, and A. Lagendijk, "Focusing and scanning microscopy with propagating surface plasmons," Phys. Rev. Lett. **110**, 266804 (2013).

[128] H. Yilmaz, E. G. van Putten, J. Bertolotti, A. Lagendijk, W. L. Vos, and A. P. Mosk, "Speckle correlation resolution enhancement of wide-field fluorescence imaging," Optica **2**, 424–429 (2015).

[129] A. Yariv, "On transmission and recovery of three-dimensional image information in optical waveguides," J. Opt. Soc. Am. **66**, 301–306 (1976).

[130] A. Gover, C. Lee, and A. Yariv, "Direct transmission of pictorial information in multimode optical fibers," J. Opt. Soc. Am. **66**, 306–311 (1976).

[131] G. J. Dunning and R. Lind, "Demonstration of image transmission through fibers by optical phase conjugation," Opt. Lett. **7**, 558–560 (1982).

[132] A. Friesem, U. Levy, and Y. Silberberg, "Parallel transmission of images through single optical fibers," Proc. IEEE **71**, 208–221 (1983).

[133] T. Čižmár and K. Dholakia, "Shaping the light transmission through a multimode optical fibre: Complex transformation analysis and applications in biophotonics," Opt. Express **19**, 18871–18884 (2011).

[134] M. Plöschner, T. Tyc, and T. Čižmár, "Seeing through chaos in multimode fibres," Nat. Photonics **9**, 529–535 (2015).

[135] D. E. B. Flaes, J. Stopka, S. Turtaev, J. F. De Boer, T. Tyc, and T. Čižmár, "Robustness of light-transport processes to bending deformations in graded-index multimode waveguides," Phys. Rev. Lett. **120**, 233901 (2018).

[136] T. Čižmár and K. Dholakia, "Exploiting multimode waveguides for pure fibre-based imaging," Nat. Commun. **3**, 2024 (2012).

[137] Y. Choi, C. Yoon, M. Kim, T. D. Yang, C. Fang-Yen, R. R. Dasari, K. J. Lee, and W. Choi, "Scanner-free and wide-field endoscopic imaging by using a single multimode optical fiber," Phys. Rev. Lett. **109**, 203901 (2012).

[138] A. M. Caravaca-Aguirre and R. Piestun, "Single multimode fiber endoscope," Opt. Express **25**, 1656–1665 (2017).

[139] M. N'Gom, T. B. Norris, E. Michielssen, and R. R. Nadakuditi, "Mode control in a multimode fiber through acquiring its transmission matrix from a reference-less optical system," Opt. Lett. **43**, 419–422 (2018).

[140] S. Aisawa, K. Noguchi, and T. Matsumoto, "Remote image classification through multimode optical fiber using a neural network," Opt. Lett. **16**, 645–647 (1991).

[141] R. K. Marusarz and M. R. Sayeh, "Neural network-based multimode fiber-optic information transmission," Appl. Opt. **40**, 219–227 (2001).

[142] R. Takagi, R. Horisaki, and J. Tanida, "Object recognition through a multimode fiber," Opt. Rev. **24**, 117–120 (2017).

[143] B. Rahmani, D. Loterie, G. Konstantinou, D. Psaltis, and C. Moser, "Multimode optical fiber transmission with a deep learning network," Light: Sci. Appl. **7**, 1–11 (2018).

[144] N. Borhani, E. Kakkava, C. Moser, and D. Psaltis, "Learning to see through multimode fibers," Optica **5**, 960–966 (2018).

[145] P. Wang and J. Di, "Deep learning-based object classification through multimode fiber via a CNN-architecture specklenet," Appl. Opt. **57**, 8258–8263 (2018).

[146] N. Shabairou, E. Cohen, O. Wagner, D. Malka, and Z. Zalevsky, "Color image identification and reconstruction using artificial neural networks on multimode fiber images: Towards an all-optical design," Opt. Lett. **43**, 5603–5606 (2018).

[147] O. Moran, P. Caramazza, D. Faccio, and R. Murray-Smith, "Deep, complex, invertible networks for inversion of transmission effects in multimode optical fibres," in 32nd Conference on Neural Information Processing Systems (NeurIPS 2018), Montréal, Canada (2018).

[148] L. V. Amitonova and J. F. De Boer, "Compressive imaging through a multimode fiber," Opt. Lett. **43**, 5427–5430 (2018).

[149] M. Lan, D. Guan, L. Gao, J. Li, S. Yu, and G. Wu, "Robust compressive multimode fiber imaging against bending with enhanced depth of field," Opt. Express **27**, 12957–12962 (2019).

[150] P. Fan, T. Zhao, and L. Su, "Deep learning the high variability and randomness inside multimode fibers," Opt. Express **27**, 20241–20258 (2019).

[151] P. Caramazza, O. Moran, R. Murray-Smith, and D. Faccio, "Transmission of natural scene images through a multimode fibre," Nat. Commun. **10**, 2029 (2019).

[152] E. Kakkava, N. Borhani, B. Rahmani, U. Teğin, C. Moser, and D. Psaltis, "Deep learning-based image classification through a multimode fiber in the presence of wavelength drift," Appl. Sci. **10**, 3816 (2020).

[153] T. Zhao, S. Ourselin, T. Vercauteren, and W. Xia, "Seeing through multimode fibers with real-valued intensity transmission matrices," Opt. Express **28**, 20978–20991 (2020).

[154] H. Chen, Z. He, Z. Zhang, Y. Geng, and W. Yu, "Binary amplitude-only image reconstruction through a MMF based on an AE-SNN combined deep learning model," Opt. Express **28**, 30048–30062 (2020).

[155] S. Li, C. Saunders, D. J. Lum, J. Murray-Bruce, V. K. Goyal, T. Čižmár, and D. B. Phillips, "Compressively sampling the optical transmission matrix of a multimode fibre," Light: Sci. Appl. **10**, 1–15 (2021).

[156] S. Resisi, S. M. Popoff, and Y. Bromberg, "Image transmission through a flexible multimode fiber by deep learning," arXiv:2011.05144 (2020).

[157] C. Zhu, E. A. Chan, Y. Wang, W. Peng, R. Guo, B. Zhang, C. Soci, and Y. Chong, "Image reconstruction through a multimode fiber with a simple neural network architecture," Sci. Rep. **11**, 896 (2021).

[158] R. D. Leonardo and S. Bianchi, "Hologram transmission through multi-mode optical fibers," Opt. Express **19**, 247–254 (2011).

[159] S. Bianchi and R. D. Leonardo, "A multi-mode fiber probe for holographic micromanipulation and microscopy," Lab Chip **12**, 635–639 (2012).

[160] I. N. Papadopoulos, S. Farahi, C. Moser, and D. Psaltis, "Focusing and scanning light through a multimode optical fiber using digital phase conjugation," Opt. Express **20**, 10583–10590 (2012).

[161] R. N. Mahalati, D. Askarov, J. P. Wilde, and J. M. Kahn, "Adaptive control of input field to achieve desired output intensity profile in multimode fiber with random mode coupling," Opt. Express **20**, 14321–14337 (2012).

[162] I. N. Papadopoulos, S. Farahi, C. Moser, and D. Psaltis, "High-resolution, lensless endoscope based on digital scanning through a multimode optical fiber," Biomed. Opt. Express **4**, 260–270 (2013).

[163] S. Farahi, D. Ziegler, I. N. Papadopoulos, D. Psaltis, and C. Moser, "Dynamic bending compensation while focusing through a multimode fiber," Opt. Express **21**, 22504–22514 (2013).

[164] A. M. Caravaca-Aguirre, E. Niv, D. B. Conkey, and R. Piestun, "Real-time resilient focusing through a bending multimode fiber," Opt. Express **21**, 12881–12887 (2013).

[165] M. Plöschner, V. Kollárová, Z. Dostál, J. Nylk, T. Barton-Owen, D. E. Ferrier, R. Chmelík, K. Dholakia, and T. Čižmár, "Multimode fibre: Light-sheet microscopy at the tip of a needle," Sci. Rep. **5**, 18050 (2015).

[166] D. Loterie, D. Psaltis, and C. Moser, "Bend translation in multimode fiber imaging," Opt. Express **25**, 6263–6273 (2017).

[167] L. V. Amitonova, A. P. Mosk, and P. W. Pinkse, "Rotational memory effect of a multimode fiber," Opt. Express **23**, 20569–20575 (2015).

168 S. Rosen, D. Gilboa, O. Katz, and Y. Silberberg, "Focusing and scanning through flexible multimode fibers without access to the distal end," arXiv:1506.08586 (2015).

169 S. Li, S. A. Horsley, T. Tyc, T. Čižmár, and D. B. Phillips, "Memory effect assisted imaging through multimode optical fibres," Nat. Commun. **12**, 3751 (2021).

170 A. M. Caravaca-Aguirre, A. Carron, S. Mezil, I. Wang, and E. Bossy, "Optical memory effect in square multimode fibers," Opt. Lett. **46**, 4924–4927 (2021).

171 L. V. Amitonova, A. Descloux, J. Petschulat, M. H. Frosz, G. Ahmed, F. Babic, X. Jiang, A. P. Mosk, P. S. J. Russell, and P. W. Pinkse, "High-resolution wavefront shaping with a photonic crystal fiber for multimode fiber imaging," Opt. Lett. **41**, 497–500 (2016).

172 I. T. Leite, S. Turtaev, X. Jiang, M. Šiler, A. Cuschieri, P. S. J. Russell, and T. Čižmár, "Three-dimensional holographic optical manipulation through a high-numerical-aperture soft-glass multimode fibre," Nat. Photonics **12**, 33–39 (2018).

173 I. N. Papadopoulos, S. Farahi, C. Moser, and D. Psaltis, "Increasing the imaging capabilities of multimode fibers by exploiting the properties of highly scattering media," Opt. Lett. **38**, 2776–2778 (2013).

174 S. Resisi, Y. Viernik, S. M. Popoff, and Y. Bromberg, "Wavefront shaping in multimode fibers by transmission matrix engineering," APL Photonics **5**, 036103 (2020).

175 S. A. Vasquez-Lopez, R. Turcotte, V. Koren, M. Plöschner, Z. Padamsey, M. J. Booth, T. Čižmár, and N. J. Emptage, "Subcellular spatial resolution achieved for deep-brain imaging in vivo using a minimally invasive multimode fiber," Light: Sci. Appl. **7**, 110 (2018).

176 S. Turtaev, I. T. Leite, T. Altwegg-Boussac, J. M. Pakan, N. L. Rochefort, and T. Čižmár, "High-fidelity multimode fibre-based endoscopy for deep brain in vivo imaging," Light: Sci. Appl. **7**, 92 (2018).

177 G. P. Laporte, N. Stasio, C. Moser, and D. Psaltis, "Enhanced resolution in a multimode fiber imaging system," Opt. Express **23**, 27484–27493 (2015).

178 E. E. Morales-Delgado, D. Psaltis, and C. Moser, "Two-photon imaging through a multimode fiber," Opt. Express **23**, 32158–32170 (2015).

179 D. Loterie, S. Farahi, I. Papadopoulos, A. Goy, D. Psaltis, and C. Moser, "Digital confocal microscopy through a multimode fiber," Opt. Express **23**, 23845–23858 (2015).

180 J. Trägårdh, T. Pikálek, M. Šerý, T. Meyer, J. Popp, and T. Čižmár, "Label-free cars microscopy through a multimode fiber endoscope," Opt. Express **27**, 30055–30066 (2019).

181 A. M. Caravaca-Aguirre, S. Singh, S. Labouesse, M. V. Baratta, R. Piestun, and E. Bossy, "Hybrid photoacoustic-fluorescence microendoscopy through a multimode fiber using speckle illumination," APL Photonics **4**, 096103 (2019).

182 E. E. Morales-Delgado, L. Urio, D. B. Conkey, N. Stasio, D. Psaltis, and C. Moser, "Three-dimensional microfabrication through a multimode optical fiber," Opt. Express **25**, 7031–7045 (2017).

183 S. Karbasi, K. W. Koch, and A. Mafi, "Image transport quality can be improved in disordered waveguides," Opt. Commun. **311**, 72–76 (2013).

184 S. Karbasi, R. J. Frazier, K. W. Koch, T. Hawkins, J. Ballato, and A. Mafi, "Image transport through a disordered optical fibre mediated by transverse Anderson localization," Nat. Commun. **5**, 3362 (2014).

185 J. Zhao, J. E. A. Lopez, Z. Zhu, D. Zheng, S. Pang, R. A. Correa, and A. Schulzgen, "Image transport through meter-long randomly disordered silica-air optical fiber," Sci. Rep. **8**, 3065 (2018).

186 J. Zhao, Y. Sun, Z. Zhu, J. E. Antonio-Lopez, R. A. Correa, S. Pang, and A. Schulzgen, "Deep learning imaging through fully-flexible glass-air disordered fiber," ACS Photonics **5**, 3930–3935 (2018).

187 T. H. Tuan, S. Kuroyanagi, K. Nagasaka, T. Suzuki, and Y. Ohishi, "Characterization of an all-solid disordered tellurite glass optical fiber and its NIR optical image transport," Jpn. J. Appl. Phys., Part 1 **58**, 032005 (2019).

188 M. Leonetti, S. Karbasi, A. Mafi, E. DelRe, and C. Conti, "Secure information transport by transverse localization of light," Sci. Rep. **6**, 29918 (2016).

189 A. Mafi, J. Ballato, K. W. Koch, and A. Schulzgen, "Disordered Anderson localization optical fibers for image transport—A review," J. Lightwave Technol. **37**, 5652–5659 (2019).

190 S. Karbasi, K. W. Koch, and A. Mafi, "Multiple-beam propagation in an Anderson localized optical fiber," Opt. Express **21**, 305–313 (2013).

191 P. Wang and R. Menon, "Computational spectrometer based on a broadband diffractive optic," Opt. Express **22**, 14575–14587 (2014).

192 P. Wang and R. Menon, "Computational spectroscopy via singular-value decomposition and regularization," Opt. Express **22**, 21541–21550 (2014).

193 T. Yang, C. Xu, H.-p. Ho, Y.-y. Zhu, X.-h. Hong, Q.-j. Wang, Y.-c. Chen, X.-a. Li, X.-h. Zhou, M.-d. Yi et al., "Miniature spectrometer based on diffraction in a dispersive hole array," Opt. Lett. **40**, 3217–3220 (2015).

194 T. Yang, J.-x. Peng, X.-a. Li, X. Shen, X.-h. Zhou, X.-l. Huang, W. Huang, and H.-p. Ho, "Compact broadband spectrometer based on upconversion and downconversion luminescence," Opt. Lett. **42**, 4375–4378 (2017).

195 T. Yang, X. Huang, H. Ho, C. Xu, Y. Zhu, M. Yi, X. Zhou, X. Li, and W. Huang, "Compact spectrometer based on a frosted glass," IEEE Photonics Technol. Lett. **29**, 217–220 (2016).

196 M. Chakrabarti, M. L. Jakobsen, and S. G. Hanson, "Speckle-based spectrometer," Opt. Lett. **40**, 3264–3267 (2015).

197 B. Redding, S. M. Popoff, Y. Bromberg, M. A. Choma, and H. Cao, "Noise analysis of spectrometers based on speckle pattern reconstruction," Appl. Opt. **53**, 410–417 (2014).

198 U. Kürüm, P. R. Wiecha, R. French, and O. L. Muskens, "Deep learning enabled real time speckle recognition and hyperspectral imaging using a multimode fiber array," Opt. Express **27**, 20965–20979 (2019).

199 B. Redding, S. F. Liew, R. Sarma, and H. Cao, "Compact spectrometer based on a disordered photonic chip," Nat. Photonics **7**, 746–751 (2013).

200 P. Varytis, D.-N. Huynh, W. Hartmann, W. Pernice, and K. Busch, "Design study of random spectrometers for applications at optical frequencies," Opt. Lett. **43**, 3180–3183 (2018).

201 W. Hartmann, P. Varytis, H. Gehring, N. Walter, F. Beutel, K. Busch, and W. Pernice, "Waveguide-integrated broadband spectrometer based on tailored disorder," Adv. Opt. Mater. **8**, 1901602 (2020).

202 W. Hartmann, P. Varytis, H. Gehring, N. Walter, F. Beutel, K. Busch, and W. Pernice, "Broadband spectrometer with single-photon sensitivity exploiting tailored disorder," Nano Lett. **20**, 2625–2631 (2020).

203 T. Liu and A. Fiore, "Designing open channels in random scattering media for on-chip spectrometers," Optica **7**, 934–939 (2020).

204 M. Mazilu, T. Vettenburg, A. D. Falco, and K. Dholakia, "Random super-prism wavelength meter," Opt. Lett. **39**, 96–99 (2014).

205 N. K. Metzger, R. Spesyvtsev, G. D. Bruce, B. Miller, G. T. Maker, G. Malcolm, M. Mazilu, and K. Dholakia, "Harnessing speckle for a sub-femtometre resolved broadband wavemeter and laser stabilization," Nat. Commun. **8**, 15610 (2017).

206 L. O'Donnell, K. Dholakia, and G. D. Bruce, "High speed determination of laser wavelength using Poincaré descriptors of speckle," Opt. Commun. **459**, 124906 (2020).

207 R. K. Gupta, G. D. Bruce, S. J. Powis, and K. Dholakia, "Deep learning enabled laser speckle wavemeter with a high dynamic range," Laser Photonics Rev. **14**, 2000120 (2020).

208 A. Dávila and J. Rayas, "Single-shot phase detection in a speckle wavemeter for the measurement of femtometric wavelength change," Opt. Lasers Eng. **125**, 105856 (2020).

209 W. Freude, C. Fritzsche, G. Grau, and L. Shan-da, "Speckle interferometry for spectral analysis of laser sources and multimode optical waveguides," J. Lightwave Technology **4**, 64–72 (1986).

210 B. Redding and H. Cao, "Using a multimode fiber as a high-resolution, low-loss spectrometer," Opt. Lett. **37**, 3384–3386 (2012).

211 B. Redding, S. M. Popoff, and H. Cao, "All-fiber spectrometer based on speckle pattern reconstruction," Opt. Express **21**, 6584–6600 (2013).

212 B. Redding, M. Alam, M. Seifert, and H. Cao, "High-resolution and broadband all-fiber spectrometers," Optica **1**, 175–180 (2014).

213 G. D. Bruce, L. O'Donnell, M. Chen, and K. Dholakia, "Overcoming the speckle correlation limit to achieve a fiber wavemeter with attometer resolution," Opt. Lett. **44**, 1367–1370 (2019).

214 G. D. Bruce, L. O'Donnell, M. Chen, M. Facchin, and K. Dholakia, "Femtometer-resolved simultaneous measurement of multiple laser wavelengths in a speckle wavemeter," Opt. Lett. **45**, 1926–1929 (2020).

215 S. F. Liew, B. Redding, M. A. Choma, H. D. Tagare, and H. Cao, "Broadband multimode fiber spectrometer," Opt. Lett. **41**, 2029–2032 (2016).

[216]N. Coluccelli, M. Cassinerio, B. Redding, H. Cao, P. Laporta, and G. Galzerano, "The optical frequency comb fibre spectrometer," Nat. Commun. **7**, 12995 (2016).

[217]B. Redding, S. F. Liew, Y. Bromberg, R. Sarma, and H. Cao, "Evanescently coupled multimode spiral spectrometer," Optica **3**, 956–962 (2016).

[218]G. C. Valley, G. A. Sefler, and T. J. Shaw, "Multimode waveguide speckle patterns for compressive sensing," Opt. Lett. **41**, 2529–2532 (2016).

[219]T. Wang, Y. Li, Y. Meng, Y. Qiu, and B. Mao, "Study of a fiber spectrometer based off offset fusion," Appl. Opt. **59**, 4697–4702 (2020).

[220]M. Piels and D. Zibar, "Compact silicon multimode waveguide spectrometer with enhanced bandwidth," Sci. Rep. **7**, 43454 (2017).

[221]Z. Meng, J. Li, C. Yin, T. Zhang, Z. Yu, M. Tang, W. Tong, and K. Xu, "Multimode fiber spectrometer with scalable bandwidth using space-division multiplexing," AIP Adv. **9**, 015004 (2019).

[222]D. Yi, Y. Zhang, X. Wu, and H. K. Tsang, "Integrated multimode waveguide with photonic lantern for speckle spectroscopy," IEEE J. Quantum Electron. **57**, 1–8 (2020).

[223]Y. Wan, X. Fan, S. Wang, Z. Zhang, S. Zhao, and Z. He, "Wavemeter capable of simultaneously achieving ultra-high resolution and broad bandwidth by using Rayleigh speckle from single mode fiber," J. Lightwave Technol. **39**, 2223–2229 (2021).

[224]W. Yangyang, F. Xinyu, and H. Zuyuan, "Review on speckle-based spectrum analyzer," Photonic Sens. **11**, 187–202 (2021).

[225]ŞK. Çetindağ, M. F. Toy, O. Ferhanoğlu, and F. Çivitci, "A speckle-enhanced prism spectrometer with high dynamic range," IEEE Photonics Technol. Lett. **30**, 2139–2142 (2018).

[226]S. K. Çetindağ, M. F. Toy, O. Ferhanoğlu, and F. Civitci, "Scattering metal waveguide based speckle-enhanced prism spectrometry," J. Lightwave Technol. **38**, 2022–2027 (2020).

[227]N. H. Wan, F. Meng, T. Schröder, R.-J. Shiue, E. H. Chen, and D. Englund, "High-resolution optical spectroscopy using multimode interference in a compact tapered fibre," Nat. Commun. **6**, 8762 (2015).

[228]G. Hornig, T. Harrison, L. Bu, S. Azmayesh-Fard, and R. DeCorby, "Wavemeter based on dispersion and speckle in a tapered hollow waveguide," OSA Continuum **2**, 495–506 (2019).

[229]F. Meng, Y. Zhao, H. Wang, and Y. Zhang, "High-performance compact spectrometer based on multimode interference in a tapered spiral-shaped waveguide," Opt. Express **27**, 38349–38358 (2019).

[230]U. Paudel and T. Rose, "Ultra-high resolution and broadband chip-scale speckle enhanced Fourier-transform spectrometer," Opt. Express **28**, 16469–16485 (2020).

[231]Z. Xu, Z. Wang, M. E. Sullivan, D. J. Brady, S. H. Foulger, and A. Adibi, "Multimodal multiplex spectroscopy using photonic crystals," Opt. Express **11**, 2126–2133 (2003).

[232]J. Oliver, W.-B. Lee, and H.-N. Lee, "Filters with random transmittance for improving resolution in filter-array-based spectrometers," Opt. Express **21**, 3969–3989 (2013).

[233]Z. Wang and Z. Yu, "Spectral analysis based on compressive sensing in nanophotonic structures," Opt. Express **22**, 25608–25614 (2014).

[234]C. Kim, W.-B. Lee, S. K. Lee, Y. T. Lee, and H.-N. Lee, "Fabrication of 2D thin-film filter-array for compressive sensing spectroscopy," Opt. Lasers Eng. **115**, 53–58 (2019).

[235]Y. Kwak, S. M. Park, Z. Ku, A. Urbas, and Y. L. Kim, "A pearl spectrometer," Nano Lett. **21**, 921 (2020).

[236]Z. Wang, S. Yi, A. Chen, M. Zhou, T. S. Luk, A. James, J. Nogan, W. Ross, G. Joe, A. Shahsafi et al., "Single-shot on-chip spectral sensors based on photonic crystal slabs," Nat. Commun. **10**, 1020 (2019).

[237]J. Bao and M. G. Bawendi, "A colloidal quantum dot spectrometer," Nature **523**, 67–70 (2015).

[238]P. Wang and R. Menon, "Ultra-high-sensitivity color imaging via a transparent diffractive-filter array and computational optics," Optica **2**, 933–939 (2015).

[239]P. Wang and R. Menon, "Computational multispectral video imaging," J. Opt. Soc. Am. A **35**, 189–199 (2018).

[240]R. French, S. Gigan, and O. L. Muskens, "Speckle-based hyperspectral imaging combining multiple scattering and compressive sensing in nanowire mats," Opt. Lett. **42**, 1820–1823 (2017).

[241]S. K. Sahoo, D. Tang, and C. Dang, "Single-shot multispectral imaging with a monochromatic camera," Optica **4**, 1209–1213 (2017).

[242]M. A. Golub, A. Averbuch, M. Nathan, V. A. Zheludev, J. Hauser, S. Gurevitch, R. Malinsky, and A. Kagan, "Compressed sensing snapshot spectral imaging by a regular digital camera with an added optical diffuser," Appl. Opt. **55**, 432–443 (2016).

[243]L. Zhu, J. Liu, L. Feng, C. Guo, T. Wu, and X. Shao, "Recovering the spectral and spatial information of an object behind a scattering media," OSA Continuum **1**, 553–563 (2018).

[244]J. Hauser, M. A. Golub, A. Averbuch, M. Nathan, V. A. Zheludev, and M. Kagan, "Dual-camera snapshot spectral imaging with a pupil-domain optical diffuser and compressed sensing algorithms," Appl. Opt. **59**, 1058–1070 (2020).

[245]K. Monakhova, K. Yanny, N. Aggarwal, and L. Waller, "Spectral diffusercam: Lensless snapshot hyperspectral imaging with a spectral filter array," Optica **7**, 1298–1307 (2020).

[246]R. French, S. Gigan et al., "Snapshot fiber spectral imaging using speckle correlations and compressive sensing," Opt. Express **26**, 32302–32316 (2018).

[247]T. Kohlgraf-Owens and A. Dogariu, "Finding the field transfer matrix of scattering media," Opt. Express **16**, 13225–13232 (2008).

[248]T. Kohlgraf-Owens and A. Dogariu, "Spatially resolved scattering polarimeter," Opt. Lett. **34**, 1321–1323 (2009).

[249]I. Freund, "Stokes-vector reconstruction," Opt. Lett. **15**, 1425–1427 (1990).

[250]D. Singh, Z. Chen, J. Pu, and R. K. Singh, "Recovery of polarimetric parameters from non-imaged laser-speckle," J. Opt. **20**, 085605 (2018).

[251]M. Facchin, G. D. Bruce, and K. Dholakia, "Speckle-based determination of the polarisation state of single and multiple laser beams," OSA Continuum **3**, 1302–1313 (2020).

[252]A. Roy, R. K. Singh, and M. M. Brundavanam, "Non-invasive tracking of polarization rotation from speckle contrast using uncorrelated speckle patterns," J. Opt. **22**, 125603 (2020).

[253]T. W. Kohlgraf-Owens and A. Dogariu, "Transmission matrices of random media: Means for spectral polarimetric measurements," Opt. Lett. **35**, 2236–2238 (2010).

[254]G. A. Sefler, T. J. Shaw, and G. C. Valley, "Demonstration of speckle-based compressive sensing system for recovering RF signals," Opt. Express **26**, 21390–21402 (2018).

[255]D. B. Borlaug, S. Estrella, C. T. Boone, G. A. Sefler, T. J. Shaw, A. Roy, L. Johansson, and G. C. Valley, "Photonic integrated circuit based compressive sensing radio frequency receiver using waveguide speckle," Opt. Express **29**, 19222–19239 (2021).

[256]W. Xiong, S. Gertler, H. Yilmaz, and H. Cao, "Multimode-fiber-based single-shot full-field measurement of optical pulses," Opt. Lett. **45**, 2462–2465 (2020).

[257]P. Ryczkowski, M. Barbier, A. T. Friberg, J. M. Dudley, and G. Genty, "Ghost imaging in the time domain," Nat. Photonics **10**, 167–170 (2016).

[258]S.-Y. Lee, P.-C. Hui, B. Bouma, and M. Villiger, "Single-shot depth profiling by spatio-temporal encoding with a multimode fiber," Opt. Express **28**, 1124–1138 (2020).

[259]C. G. Amiot, P. Ryczkowski, A. T. Friberg, J. M. Dudley, and G. Genty, "Ghost optical coherence tomography," Opt. Express **27**, 24114–24122 (2019).

[260]W. Xiong, B. Redding, S. Gertler, Y. Bromberg, H. D. Tagare, and H. Cao, "Deep learning of ultrafast pulses with a multimode fiber," APL Photonics **5**, 096106 (2020).

[261]R. Ziv, A. Dikopoltsev, T. Zahavy, I. Rubinstein, P. Sidorenko, O. Cohen, and M. Segev, "Deep learning reconstruction of ultrashort pulses from 2D spatial intensity patterns recorded by an all-in-line system in a single-shot," Opt. Express **28**, 7528–7538 (2020).

[262]T. Zahavy, A. Dikopoltsev, D. Moss, G. I. Haham, O. Cohen, S. Mannor, and M. Segev, "Deep learning reconstruction of ultrashort pulses," Optica **5**, 666–673 (2018).

[263]L. Mandel and E. Wolf, *Optical Coherence and Quantum Optics* (Cambridge University Press, 1995).

[264]H. Cao, "Lasing in random media," Waves Random Media **13**, R1 (2003).

[265]M. Noginov, *Solid-State Random Lasers* (Springer, 2006), Vol. 105.

[266] D. S. Wiersma, "The physics and applications of random lasers," Nat. Phys. **4**, 359–367 (2008).

[267] V. M. Markushev, V. Zolin, and C. M. Briskina, "Luminescence and stimulated emission of neodymium in sodium lanthanum molybdate powders," Sov. J. Quantum Electron. **16**, 281 (1986).

[268] N. M. Lawandy, R. Balachandran, A. Gomes, and E. Sauvain, "Laser action in strongly scattering media," Nature **368**, 436–438 (1994).

[269] M. Siddique, L. Yang, Q. Wang, and R. Alfano, "Mirrorless laser action from optically pumped dye-treated animal tissues," Opt. Commun. **117**, 475–479 (1995).

[270] H. Cao, Y. Zhao, H. Ong, S. Ho, J. Y. Dai, J. Y. Wu, and R. Chang, "Ultraviolet lasing in resonators formed by scattering in semiconductor polycrystalline films," Appl. Phys. Lett. **73**, 3656–3658 (1998).

[271] S. Frolov, Z. Vardeny, K. Yoshino, A. Zakhidov, and R. Baughman, "Stimulated emission in high-gain organic media," Phys. Rev. B **59**, R5284 (1999).

[272] S. K. Turitsyn, S. A. Babin, A. E. El-Taher, P. Harper, D. V. Churkin, S. I. Kablukov, J. D. Ania-Castañón, V. Karalekas, and E. V. Podivilov, "Random distributed feedback fibre laser," Nat. Photonics **4**, 231–235 (2010).

[273] Q. Baudouin, N. Mercadier, V. Guarrera, W. Guerin, and R. Kaiser, "A cold-atom random laser," Nat. Phys. **9**, 357–360 (2013).

[274] E. S. Leong and S. F. Yu, "UV random lasing action in p-SiC (4h)/i-ZnO–SiO$_2$ nanocomposite/n-ZnO:Al heterojunction diodes," Adv. Mater. **18**, 1685–1688 (2006).

[275] M. Leonetti, C. Conti, and C. Lopez, "The mode-locking transition of random lasers," Nat. Photonics **5**, 615–617 (2011).

[276] H. K. Liang, B. Meng, G. Liang, J. Tao, Y. Chong, Q. J. Wang, and Y. Zhang, "Electrically pumped mid-infrared random lasers," Adv. Mater. **25**, 6859–6863 (2013).

[277] S. Schönhuber, M. Brandstetter, T. Hisch, C. Deutsch, M. Krall, H. Detz, A. M. Andrews, G. Strasser, S. Rotter, and K. Unterrainer, "Random lasers for broadband directional emission," Optica **3**, 1035–1038 (2016).

[278] S. Lowenthal and D. Joyeux, "Speckle removal by a slowly moving diffuser associated with a motionless diffuser," J. Opt. Soc. Am. **61**, 847–851 (1971).

[279] B. Redding, G. Allen, E. R. Dufresne, and H. Cao, "Low-loss high-speed speckle reduction using a colloidal dispersion," Appl. Opt. **52**, 1168–1172 (2013).

[280] V. Letokhov, "Generation of light by a scattering medium with negative resonance absorption," Sov. Phys. JETP **26**, 835–840 (1968).

[281] D. S. Wiersma and A. Lagendijk, "Light diffusion with gain and random lasers," Phys. Rev. E **54**, 4256 (1996).

[282] H. Cao, Y. Zhao, S. Ho, E. Seelig, Q. Wang, and R. Chang, "Random laser action in semiconductor powder," Phys. Rev. Lett. **82**, 2278 (1999).

[283] H. Cao, "Review on latest developments in random lasers with coherent feedback," J. Phys. A **38**, 10497 (2005).

[284] H. Cao, R. Chriki, S. Bittner, A. A. Friesem, and N. Davidson, "Complex lasers with controllable coherence," Nat. Rev. Phys. **1**, 156–168 (2019).

[285] M. Noginov, S. Egarievwe, N. Noginova, H. Caulfield, and J. Wang, "Interferometric studies of coherence in a powder laser," Opt. Mater. **12**, 127–134 (1999).

[286] B. Redding, M. A. Choma, and H. Cao, "Spatial coherence of random laser emission," Opt. Lett. **36**, 3404–3406 (2011).

[287] M. Koivurova, E. Vasileva, Y. Li, L. Berglund, and S. Popov, "Complete spatial coherence characterization of quasi-random laser emission from dye doped transparent wood," Opt. Express **26**, 13474–13482 (2018).

[288] R. Ma, J. Q. Li, J. Y. Guo, H. Wu, H. H. Zhang, B. Hu, Y. J. Rao, and W. L. Zhang, "High-power low spatial coherence random fiber laser," Opt. Express **27**, 8738–8744 (2019).

[289] B. Redding, M. A. Choma, and H. Cao, "Speckle-free laser imaging using random laser illumination," Nat. Photonics **6**, 355–359 (2012).

[290] B. H. Hokr, M. S. Schmidt, J. N. Bixler, P. N. Dyer, G. D. Noojin, B. Redding, R. J. Thomas, B. A. Rockwell, H. Cao, V. V. Yakovlev *et al.*, "A narrow-band speckle-free light source via random Raman lasing," J. Mod. Opt. **63**, 46–49 (2016).

[291] M. Barredo-Zuriarrain, I. Iparraguirre, J. Fernández, J. Azkargorta, and R. Balda, "Speckle-free near-infrared imaging using a Nd$^{3+}$ random laser," Laser Phys. Lett. **14**, 106201 (2017).

[292] R. Ma, Y. J. Rao, W. L. Zhang, and B. Hu, "Multimode random fiber laser for speckle-free imaging," IEEE J. Sel. Top. Quantum Electron. **25**, 1–6 (2018).

[293] J. He, W.-K. Chan, X. Cheng, M.-L. Tse, C. Lu, P.-K. Wai, S. Savovic, and H.-Y. Tam, "Experimental and theoretical investigation of the polymer optical fiber random laser with resonant feedback," Adv. Opt. Mater. **6**, 1701187 (2018).

[294] Y.-J. Lee, T.-W. Yeh, Z.-P. Yang, Y.-C. Yao, C.-Y. Chang, M.-T. Tsai, and J.-K. Sheu, "A curvature-tunable random laser," Nanoscale **11**, 3534–3545 (2019).

[295] J. Y. Guo, W. L. Zhang, Y. J. Rao, H. H. Zhang, R. Ma, D. S. Lopes, I. C. Lins, and A. S. Gomes, "High contrast dental imaging using a random fiber laser in backscattering configuration," OSA Continuum **3**, 759–766 (2020).

[296] A. Mermillod-Blondin, H. Mentzel, and A. Rosenfeld, "Time-resolved microscopy with random lasers," Opt. Lett. **38**, 4112–4115 (2013).

[297] B. H. Hokr, J. V. Thompson, J. N. Bixler, D. T. Nodurft, G. D. Noojin, B. Redding, R. J. Thomas, H. Cao, B. A. Rockwell, M. O. Scully *et al.*, "Enabling time resolved microscopy with random Raman lasing," Sci. Rep. **7**, 44572 (2017).

[298] A. Boschetti, A. Taschin, P. Bartolini, A. K. Tiwari, L. Pattelli, R. Torre, and D. S. Wiersma, "Spectral super-resolution spectroscopy using a random laser," Nat. Photonics **14**, 177–182 (2020).

[299] H. Cao, X. Jiang, Y. Ling, J. Xu, and C. Soukoulis, "Mode repulsion and mode coupling in random lasers," Phys. Rev. B **67**, 161101 (2003).

[300] S. Mujumdar, M. Ricci, R. Torre, and D. S. Wiersma, "Amplified extended modes in random lasers," Phys. Rev. Lett. **93**, 053903 (2004).

[301] X. Wu and H. Cao, "Statistics of random lasing modes in weakly scattering systems," Opt. Lett. **32**, 3089–3091 (2007).

[302] X. Wu and H. Cao, "Statistical studies of random-lasing modes and amplified spontaneous-emission spikes in weakly scattering systems," Phys. Rev. A **77**, 013832 (2008).

[303] M. Gagné and R. Kashyap, "Demonstration of a 3 mW threshold Er-doped random fiber laser based on a unique fiber Bragg grating," Opt. Express **17**, 19067–19074 (2009).

[304] N. Lizárraga, N. Puente, E. Chaikina, T. Leskova, and E. Méndez, "Single-mode Er-doped fiber random laser with distributed Bragg grating feedback," Opt. Express **17**, 395–404 (2009).

[305] S. K. Turitsyn, S. A. Babin, D. V. Churkin, I. D. Vatnik, M. Nikulin, and E. V. Podivilov, "Random distributed feedback fibre lasers," Phys. Rep. **542**, 133–193 (2014).

[306] S. Babin, A. El-Taher, P. Harper, E. Podivilov, and S. Turitsyn, "Tunable random fiber laser," Phys. Rev. A **84**, 021805 (2011).

[307] A. Sarmani, R. Zamiri, M. A. Bakar, B. Azmi, A. Zaidan, and M. Mahdi, "Tunable Raman fiber laser induced by Rayleigh backscattering in an ultra-long cavity," J. Eur. Opt. Soc. **6**, 11043 (2011).

[308] Y. Y. Zhu, W. L. Zhang, and Y. Jiang, "Tunable multi-wavelength fiber laser based on random Rayleigh back-scattering," IEEE Photonics Technol. Lett. **25**, 1559–1561 (2013).

[309] X. Du, H. Zhang, X. Wang, and P. Zhou, "Tunable random distributed feedback fiber laser operating at 1 $\mu$m," Appl. Opt. **54**, 908–911 (2015).

[310] L. Zhang, H. Jiang, X. Yang, W. Pan, and Y. Feng, "Ultra-wide wavelength tuning of a cascaded Raman random fiber laser," Opt. Lett. **41**, 215–218 (2016).

[311] L. Zhang, H. Jiang, X. Yang, W. Pan, S. Cui, and Y. Feng, "Nearly-octave wavelength tuning of a continuous wave fiber laser," Sci. Rep. **7**, 42611 (2017).

[312] I. D. Vatnik, D. V. Churkin, S. A. Babin, and S. K. Turitsyn, "Cascaded random distributed feedback Raman fiber laser operating at 1.2 $\mu$m," Opt. Express **19**, 18486–18494 (2011).

[313] W. L. Zhang, Y. J. Rao, J. M. Zhu, Z. X. Y. Z. N. Wang, and X. H. Jia, "Low threshold 2nd-order random lasing of a fiber laser with a half-opened cavity," Opt. Express **20**, 14400–14405 (2012).

[314] Z. Wang, H. Wu, M. Fan, Y. Rao, X. Jia, and W. Zhang, "Third-order random lasing via Raman gain and Rayleigh feedback within a half-open cavity," Opt. Express **21**, 20090–20095 (2013).

[315] S. A. Babin, E. A. Zlobina, S. I. Kablukov, and E. V. Podivilov, "High-order random Raman lasing in a pm fiber with ultimate efficiency and narrow bandwidth," Sci. Rep. **6**, 22625 (2016).

[316] J. Dong, L. Zhang, H. Jiang, X. Yang, W. Pan, S. Cui, X. Gu, and Y. Feng, "High order cascaded Raman random fiber laser with high spectral purity," Opt. Express **26**, 5275–5280 (2018).

[317] X. Du, H. Zhang, H. Xiao, P. Ma, X. Wang, P. Zhou, and Z. Liu, "High-power random distributed feedback fiber laser: From science to application," Ann. Phys. **528**, 649–662 (2016).

[318] H. Zhang, P. Zhou, H. Xiao, and X. Xu, "Efficient Raman fiber laser based on random Rayleigh distributed feedback with record high power," Laser Phys. Lett. **11**, 075104 (2014).

[319] H. Zhang, P. Zhou, X. Wang, X. Du, H. Xiao, and X. Xu, "Hundred-watt-level high power random distributed feedback raman fiber laser at 1150 nm and its application in mid-infrared laser generation," Opt. Express **23**, 17138–17144 (2015).

[320] X. Du, H. Zhang, X. Wang, P. Zhou, and Z. Liu, "Short cavity-length random fiber laser with record power and ultrahigh efficiency," Opt. Lett. **41**, 571–574 (2016).

[321] H. Zhang, X. Du, P. Zhou, X. Wang, and X. Xu, "Tapered fiber based high power random laser," Opt. Express **24**, 9112–9118 (2016).

[322] H. Zhang, L. Huang, P. Zhou, X. Wang, J. Xu, and X. Xu, "More than 400 W random fiber laser with excellent beam quality," Opt. Lett. **42**, 3347–3350 (2017).

[323] H. Zhang, J. Ye, P. Zhou, X. Wang, J. Leng, J. Xu, J. Wu, and X. Xu, "Tapered-fiber-enabled high-power, high-spectral-purity random fiber lasing," Opt. Lett. **43**, 4152–4155 (2018).

[324] H. Zhang, L. Huang, J. Song, H. Wu, P. Zhou, X. Wang, J. Wu, J. Xu, Z. Wang, X. Xu *et al.*, "Quasi-kilowatt random fiber laser," Opt. Lett. **44**, 2613–2616 (2019).

[325] I. D. Vatnik, D. V. Churkin, and S. A. Babin, "Power optimization of random distributed feedback fiber lasers," Opt. Express **20**, 28033–28038 (2012).

[326] E. Zlobina, S. Kablukov, and S. Babin, "Linearly polarized random fiber laser with ultimate efficiency," Opt. Lett. **40**, 4074–4077 (2015).

[327] X. Du, H. Zhang, P. Ma, H. Xiao, X. Wang, P. Zhou, and Z. Liu, "Kilowatt-level fiber amplifier with spectral-broadening-free property seeded by a random fiber laser," Opt. Lett. **40**, 5311–5314 (2015).

[328] H. Wu, P. Wang, J. Song, J. Ye, J. Xu, X. Li, and P. Zhou, "High power tunable mid-infrared optical parametric oscillator enabled by random fiber laser," Opt. Express **26**, 6446–6455 (2018).

[329] E. Dontsova, S. Kablukov, I. Vatnik, and S. Babin, "Frequency doubling of Raman fiber lasers with random distributed feedback," Opt. Lett. **41**, 1439–1442 (2016).

[330] D. V. Churkin, S. Sugavanam, I. D. Vatnik, Z. Wang, E. V. Podivilov, S. A. Babin, Y. Rao, and S. K. Turitsyn, "Recent advances in fundamentals and applications of random fiber lasers," Adv. Opt. Photonics **7**, 516–569 (2015).

[331] H. Chen, S. Gao, M. Zhang, J. Zhang, L. Qiao, T. Wang, F. Gao, X. Hu, S. Li, and Y. Zhu, "Advances in random fiber lasers and their sensing application," Sensor **20**, 6122 (2020).

[332] J. Ohtsubo, *Semiconductor Lasers: Stability, Instability and Chaos* (Springer, 2012), Vol. 111.

[333] S. Bittner, S. Guazzotti, Y. Zeng, X. Hu, H. Y. ilmaz, K. Kim, S. S. Oh, Q. J. Wang, O. Hess, and H. Cao, "Suppressing spatiotemporal lasing instabilities with wave-chaotic microcavities," Science **361**, 1225–1231 (2018).

[334] L. Furfaro, F. Pedaci, M. Giudici, X. Hachair, J. Tredicce, and S. Balle, "Mode-switching in semiconductor lasers," IEEE J. Quantum Electron. **40**, 1365–1376 (2004).

[335] E. Yablonovitch and G. D. Cody, "Intensity enhancement in textured optical sheets for solar cells," IEEE Trans. Electron Devices **29**, 300–305 (1982).

[336] C. Rockstuhl, F. Lederer, K. Bittkau, and R. Carius, "Light localization at randomly textured surfaces for solar-cell applications," Appl. Phys. Lett. **91**, 171104 (2007).

[337] F. Pratesi, M. Burresi, F. Riboli, K. Vynck, and D. S. Wiersma, "Disordered photonic structures for light harvesting in solar cells," Opt. Express **21**, A460–A468 (2013).

[338] P. Vukusic, B. Hallam, and J. Noyes, "Brilliant whiteness in ultrathin beetle scales," Science **315**, 348–348 (2007).

[339] L. Cortese, L. Pattelli, F. Utel, S. Vignolini, M. Burresi, and D. S. Wiersma, "Anisotropic light transport in white beetle scales," Adv. Opt. Mater. **3**, 1337–1341 (2015).

[340] V. Trivedi, S. Mahajan, M. Joglekar, V. Chhaniwal, Z. Zalevsky, B. Javidi, and A. Anand, "3D printed hand-held refractometer based on laser speckle correlation," Opt. Lasers Eng. **118**, 7–13 (2019).

[341] K. Kim, H. Yu, J. Koh, J. H. Shin, W. Lee, and Y. Park, "Remote sensing of pressure inside deformable microchannels using light scattering in scotch tape," Opt. Lett. **41**, 1837–1840 (2016).

[342] T. Okamoto and I. Yamaguchi, "Multimode fiber-optic mach-zehnder interferometer and its use in temperature measurement," Appl. Opt. **27**, 3085–3087 (1988).

[343] K. Pan, C.-M. Uang, F. Cheng, and T. Francis, "Multimode fiber sensing by using mean-absolute speckle-intensity variation," Appl. Opt. **33**, 2095–2098 (1994).

[344] O. Oraby, J. Spencer, and G. Jones, "Monitoring changes in the speckle field from an optical fibre exposed to low frequency acoustical vibrations," J. Mod. Opt. **56**, 55–66 (2009).

[345] E. Fujiwara, Y. T. Wu, and C. K. Suzuki, "Vibration-based specklegram fiber sensor for measurement of properties of liquids," Opt. Lasers Eng. **50**, 1726–1730 (2012).

[346] T. Francis, J. Zhang, K. Pan, D. Zhao, and P. B. Ruffin, "Fiber vibration sensor that uses the speckle contrast ratio," Opt. Eng. **34**, 236–239 (1995).

[347] W. Ha, S. Lee, Y. Jung, J. K. Kim, and K. Oh, "Acousto-optic control of speckle contrast in multimode fibers with a cylindrical piezoelectric transducer oscillating in the radial direction," Opt. Express **17**, 17536–17546 (2009).

[348] S. Wu, S. Yin, and T. Francis, "Sensing with fiber specklegrams," Appl. Opt. **30**, 4468–4470 (1991).

[349] H. Cao, "Random lasers: Development, features and applications," Opt. Photonics News **16**, 24–29 (2005).

[350] R. Polson and Z. Vardeny, "Cancerous tissue mapping from random lasing emission spectra," J. Opt. **12**, 024010 (2010).

[351] E. Ignesti, F. Tommasi, L. Fini, F. Martelli, N. Azzali, and S. Cavalieri, "A new class of optical sensors: A random laser based device," Sci. Rep. **6**, 35225 (2016).

[352] S. Caixeiro, M. Gaio, B. Marelli, F. G. Omenetto, and R. Sapienza, "Silk-based biocompatible random lasing," Adv. Opt. Mater. **4**, 998–1003 (2016).

[353] A. Saade, F. Caltagirone, I. Carron, L. Daudet, A. Drémeau, S. Gigan, and F. Krzakala, "Random projections through multiple optical scattering: Approximating kernels at the speed of light," in *2016 IEEE International Conference on Acoustics, Speech and Signal Processing (ICASSP)* (IEEE, 2016), pp. 6215–6219.

[354] G. Van der Sande, D. Brunner, and M. C. Soriano, "Advances in photonic reservoir computing," Nanophotonics **6**, 561–576 (2017).

[355] K-i Kitayama, M. Notomi, M. Naruse, K. Inoue, S. Kawakami, and A. Uchida, "Novel frontier of photonics for data processing–photonic accelerator," APL Photonics **4**, 090901 (2019).

[356] J. Dong, M. Rafayelyan, F. Krzakala, and S. Gigan, "Optical reservoir computing using multiple light scattering for chaotic systems prediction," IEEE J. Sel. Top. Quantum Electron. **26**, 1–12 (2019).

[357] M. Rafayelyan, J. Dong, Y. Tan, F. Krzakala, and S. Gigan, "Large-scale optical reservoir computing for spatiotemporal chaotic systems prediction," Phys. Rev. X **10**, 041037 (2020).

[358] U. Paudel, M. Luengo-Kovac, J. Pilawa, T. J. Shaw, and G. C. Valley, "Classification of time-domain waveforms using a speckle-based optical reservoir computer," Opt. Express **28**, 1225–1237 (2020).

[359] M. N. Ashner, U. Paudel, M. Luengo-Kovac, J. Pilawa, and G. C. Valley, "Photonic reservoir computer using speckle in multimode waveguide ring resonators," Opt. Express **29**, 19262–19277 (2021).

[360] S. Sunada, K. Kanno, and A. Uchida, "Using multidimensional speckle dynamics for high-speed, large-scale, parallel photonic computing," Opt. Express **28**, 30349–30361 (2020).

[361] S. R. Huisman, T. J. Huisman, T. A. Wolterink, A. P. Mosk, and P. W. Pinkse, "Programmable multiport optical circuits in opaque scattering materials," Opt. Express **23**, 3102–3116 (2015).

[362] T. A. Wolterink, R. Uppu, G. Ctistis, W. L. Vos, K.-J. Boller, and P. W. Pinkse, "Programmable two-photon quantum interference in $10^3$ channels in opaque scattering media," Phys. Rev. A **93**, 053817 (2016).

[363]M. W. Matthès, P. del Hougne, J. de Rosny, G. Lerosey, and S. M. Popoff, "Optical complex media as universal reconfigurable linear operators," Optica **6**, 465–472 (2019).

[364]S. Leedumrongwatthanakun, L. Innocenti, H. Defienne, T. Juffmann, A. Ferraro, M. Paternostro, and S. Gigan, "Programmable linear quantum networks with a multimode fibre," Nat. Photonics **14**, 139–142 (2020).

[365]K. Kim, S. Bittner, Y. Zeng, S. Guazzotti, O. Hess, Q. J. Wang, and H. Cao, "Massively parallel ultrafast random bit generation with a chip-scale laser," Science **371**, 948–952 (2021).

[366]C. Rockstuhl, S. Fahr, K. Bittkau, T. Beckers, R. Carius, F.-J. Haug, T. Söderström, C. Ballif, and F. Lederer, "Comparison and optimization of randomly textured surfaces in thin-film solar cells," Opt. Express **18**, A335–A342 (2010).

[367]V. E. Ferry, M. A. Verschuuren, M. C. van Lare, R. E. Schropp, H. A. Atwater, and A. Polman, "Optimized spatial correlations for broadband light trapping nanopatterns in high efficiency ultrathin film a-Si:H solar cells," Nano Lett. **11**, 4239–4245 (2011).

[368]X. Sheng, S. G. Johnson, J. Michel, and L. C. Kimerling, "Optimization-based design of surface textures for thin-film Si solar cells," Opt. Express **19**, A841–A850 (2011).

[369]K. Vynck, M. Burresi, F. Riboli, and D. S. Wiersma, "Photon management in two-dimensional disordered media," Nat. Mater. **11**, 1017–1022 (2012).

[370]T. Nakamura, R. Horisaki, and J. Tanida, "Compact wide-field-of-view imager with a designed disordered medium," Opt. Rev. **22**, 19–24 (2015).

[371]H. Kwon, E. Arbabi, S. M. Kamali, M. Faraji-Dana, and A. Faraon, "Computational complex optical field imaging using a designed metasurface diffuser," Optica **5**, 924–931 (2018).

[372]C. Rockstuhl and T. Scharf, *Amorphous Nanophotonics* (Springer Science & Business Media, 2013).

[373]R. O. Prum, R. H. Torres, S. Williamson, and J. Dyck, "Coherent light scattering by blue feather barbs," Nature **396**, 28–29 (1998).

[374]H. Noh, S. F. Liew, V. Saranathan, S. G. Mochrie, R. O. Prum, E. R. Dufresne, and H. Cao, "How noniridescent colors are generated by quasi-ordered structures of bird feathers," Adv. Mater. **22**, 2871–2880 (2010).

[375]J. D. Forster, H. Noh, S. F. Liew, V. Saranathan, C. F. Schreck, L. Yang, J.-G. Park, R. O. Prum, S. G. Mochrie, C. S. O'Hern *et al.*, "Biomimetic isotropic nanostructures for structural coloration," Adv. Mater. **22**, 2939–2944 (2010).

[376]J.-G. Park, S.-H. Kim, S. Magkiriadou, T. M. Choi, Y.-S. Kim, and V. N. Manoharan, "Full-spectrum photonic pigments with non-iridescent structural colors through colloidal assembly," Angew. Chem. Int. Ed. **53**, 2899–2903 (2014).

[377]R. H. Siddique, Y. J. Donie, G. Gomard, S. Yalamanchili, T. Merdzhanova, U. Lemmer, and H. Hölscher, "Bioinspired phase-separated disordered nanostructures for thin photovoltaic absorbers," Sci. Adv. **3**, e1700232 (2017).

[378]L. Dal Negro, *Optics of Aperiodic Structures: Fundamentals and Device Applications* (CRC Press, 2013).

[379]J.-K. Yang, S. V. Boriskina, H. Noh, M. J. Rooks, G. S. Solomon, L. Dal Negro, and H. Cao, "Demonstration of laser action in a pseudorandom medium," Appl. Phys. Lett. **97**, 223101 (2010).

[380]L. Zhang, J. Dong, and Y. Feng, "High-power and high-order random Raman fiber lasers," IEEE J. Sel. Top. Quantum Electron. **24**, 1–6 (2017).